

UNCLASSIFIED

AD NUMBER

AD825459

LIMITATION CHANGES

TO:

Approved for public release; distribution is unlimited.

FROM:

Distribution authorized to U.S. Gov't. agencies and their contractors;  
Administrative/Operational Use; OCT 1967. Other requests shall be referred to Space and Missile Systems Organization, Norton AFB, CA.

AUTHORITY

SAMSO ltr 19 Jan 1972

THIS PAGE IS UNCLASSIFIED

AD825459

# PENETRATION SYSTEMS STUDIES REENTRY PHYSICS PROJECT

## FINAL REPORT CDRL ITEM 3

Advanced Research Projects Agency

ARPA Order No. 888

October 1967



Prepared for Headquarters  
SPACE AND MISSILE SYSTEMS ORGANIZATION  
AIR FORCE SYSTEMS COMMAND  
Norton Air Force Base, California 92409

This document is subject to special export controls and each transmittal to foreign governments or foreign nationals may be made only with prior approval of Space and Missile Systems Organization (SMSO), Los Angeles AFS, Los Angeles, Calif.

7854-6099-R000

This research was supported by the Advanced Research Projects Agency of the Department of Defense, and was monitored by SAMSO/SMYSE under Contract No. AF 04(694)992.

**TRW**  
SYSTEMS GROUP

SAMSO-TR-67-133

# PENETRATION SYSTEMS STUDIES REENTRY PHYSICS PROJECT

## FINAL REPORT CDRL ITEM 3

Advanced Research Projects Agency  
ARPA Order No. 888

October 1967

Prepared for Headquarters  
**SPACE AND MISSILE SYSTEMS ORGANIZATION**  
**AIR FORCE SYSTEMS COMMAND**  
Norton Air Force Base, California 92409

This document is subject to special export controls and each transmittal to foreign governments or foreign nationals may be made only with prior approval of Space and Missile Systems Organization (SMSO), Los Angeles AFS, Los Angeles, Calif. 7854-6099-R000

This research was supported by the Advanced Research Projects Agency of the Department of Defense, and was monitored by SAMSO/SMYSE under Contract No. AF 04(694)992.

**TRW**  
SYSTEMS GROUP

## FOREWORD

This research was supported by the Advanced Research Projects Agency of the Department of Defense and was monitored by the Space and Missile Systems Organization of the Air Force Systems Command, Norton Air Force Base, San Bernardino, California. The work reported here is submitted as the final report on Reentry Physics, Penetration Systems Studies, Contract AF 04(694)-992.

This document is subject to special export controls and each transmittal to foreign governments or foreign nationals may be made only with prior approval of Space and Missile Systems Organization (SMSD), Los Angeles AFS, Los Angeles, California.

The above statement is made for the following reason: Information in this report is embargoed under the Department of State International Traffic in Arms Regulations. This report may be released to foreign governments by departments or agencies of the U. S. government subject to approval of Space and Missile Systems Organization (SMSD), Los Angeles AFS, Los Angeles, California, or higher authority within the Department of the Air Force. Private individuals or firms require a Department of State export license.

Publication of this report does not constitute Air Force approval of the report's findings or conclusions. It is published only for the exchange and stimulation of ideas.

Captain William Mercer/SMYSE



## ABSTRACT

The present report describes the results obtained under the Reentry Physics portion of the Penetration Systems Studies contract. The purpose of the contract is to carry out analyses and experiments of hypersonic flow in support of missile detection and discrimination technology. The work comprises the following five tasks: (a) high altitude drag investigation, (b) nonequilibrium turbulent boundary layer, (c) wake turbulence measurements, (d) improved laminar wake, and (e) near wake analysis. The last four tasks fall under the general heading of hypersonic wake and boundary layer technology. The objective and approach for each task is presented together with a summary of the results obtained to date.

## SYMBOLS FOR SECTION II

$\lambda$	Mean free path
$D$	Characteristic body dimension
$u$	x molecular thermal velocity = $U - \bar{U}$
$v$	y molecular thermal velocity
$w$	z molecular thermal velocity
$U$	x molecular velocity with respect to body
$\bar{U}$	x fluid mechanical velocity
$\bar{V}$	y fluid mechanical velocity
$v_m$	most probable molecular speed = $\sqrt{2 \frac{k}{m} T}$
$K_n$	Knudsen number = $\lambda / D$
$S$	speed ratio = $\bar{U} / v_{m_\infty} = \sqrt{\frac{\gamma}{2}} M$
$T_b$	body temperature
$T_t$	total temperature of fluid
$T$	static temperature of fluid
$f(u) = \int_{-\infty}^{\infty} \int_{-\infty}^{\infty} f(u, v, w) dv dw$	distribution function for x molecular thermal velocity
$\rho$	mass density
$H$	total enthalpy
$C_D$	drag coefficient
$R_e$	Reynolds number = $\frac{\rho \bar{U}_\infty D}{\mu_\infty} = 1.77 \frac{S}{K_n} = 1.62 \frac{M}{K_n}$
$T_w$	Free molecule equilibrium temperature
$SS$	Sample size
$\Delta t_m$	Movement time

$M_c$	Number of molecules per cell at Time = 0
$\bar{t}$	Mean collision time per molecule
$A$	Molecular collision cross section
$v_r$	Relative velocity between two molecules
$\bar{c}$	Mean molecular thermal speed
$N$	Number density of molecules
$N_c$	Number of molecules in a cell
$T_{st}$	Time to reach approximate steady state
$M$	Mach number
$R_n$	nose radius
$R_d$	base radius
$Re_{we}$	$\frac{V_\infty \rho_\infty l}{\mu_w}$
$l$	cone wetted length
$\mu_w$	viscosity evaluated at wall temperature

## CONTENTS

	Page
I. INTRODUCTION	1
II. HIGH ALTITUDE DRAG INVESTIGATION	
2.1 Introduction and Background	3
2.2 Description of the Monte Carlo Method	4
2.3 Monte Carlo Calculations	6
2.4 Low Density Wind Tunnel Experiments	24
2.5 Comparisons of Monte Carlo Theory with Experiment	34
2.6 Conclusions	39
2.7 Recommendations for Future Work	40
III. WAKE TURBULENCE MEASUREMENTS	
3.1 Introduction and Background	41
3.2 Space Correlation Length Measurements	41
3.3 Extended X/D Data	42
3.4 Off-Axis Data	45
3.5 Two-Data Space Correlation Length Scale	46
3.6 Mean Velocity Temperature and Density	47
3.7 Fluctuation Measurements of Velocity Temperature and Density	48
3.8 Sphere Wake Measurements	51
3.9 Cone Wake Measurements	52
3.10 Conclusions	52
3.11 Recommendations	52
IV. TURBULENT CHEMICALLY REACTING BOUNDARY LAYER	
4.1 Introduction and Background	54
4.2 Low Speed Turbulent Boundary Layer	54
4.3 Compressibility Transformation	63
4.4 Chemical Kinetics	64
4.5 Conclusions	70
4.6 Recommendations	70
V. IMPROVED LAMINAR WAKE	
5.1 Introduction and Background	71
5.2 Technical Approach	72
5.3 Results	74
5.4 Conclusions	74
VI. NEAR WAKE	
6.1 Introduction and Background	77
6.2 Corner Flow	79
6.3 Downstream Effects of Upstream Influence	82
6.4 Inviscid Flow Assumption	86
6.5 Wake Neck	91
6.6 Recirculation Region	98
6.7 Conclusions and Recommendations	103

REFERENCES	Page
	104
APPENDICES	
I CONTRACTUAL REPORTS	109
II MONTE CARLO COMPUTER SIMULATION OF TWO-DIMENSIONAL AND AXI-SYMMETRIC SUPERSONIC STEADY FLOWS	111
III PARAMETERS OF THE MONTE CARLO CALCULATION	116
IV DESCRIPTION OF LOW DENSITY WIND TUNNEL EXPERIMENTAL SET-UP	124

## ILLUSTRATIONS

	Page
1. Distribution Function in Plane Shock Wave Krook Model Numerical Solution (Ref. 11)	9
2. Monte Carlo Calculation of the Distribution Function on Stagnation Line of a Sphere	10
3. Comparison of Calculated Equilibrium Distribution Function with a Maxwellian	11
4. Cylinder Drag Coefficient vs Sample Size	12
5. 22.5° Sharp Cone Drag Coefficient vs Sample Size	13
6. Cylinder Drag Coefficient vs Sample Size	14
7. Cylinder Drag Coefficient vs Sample Size, Case 17 Continued	15
8. Cell Arrangement	16
9. Density Contours in Flow Field of a Cylinder	17
10. Temperature Contours in the Flow Field of a Cylinder	17
11. Density Contours in Flow Field of a Sphere	18
12. Density Contours in the Flow Field of a 20° Sharp W Wedge	19
13. Density Contours in the Flow Field of a 22.5° Sharp Cone	19
14. Cylinder Stagnation Line Profiles	20
15. Sphere Stagnation Line Profiles	21
16. Cell Arrangement	22
17. Cylinder Stagnation Line Profiles	23
18. Cylinder Stagnation Line Profiles	23
19. Drag Coefficients of Cones in Transition Flow	24
20. Variation of Free Molecule Equilibrium Temperature with Mach Number in a Uniform Flow (from Sherman, Ref. 13)	25

# ILLUSTRATIONS (Continued)

	Page
21. Lines of Constant Wire Temperature in the Stagnation Region of an Adiabatic Cylinder at $M_{\infty} = 5.4$ and $K_{n\infty} = 0.70$ , in Argon	26
22. Lines of Constant Wire Temperature in the Stagnation Region of an Adiabatic Cylinder at $M_{\infty} = 5.4$ and $K_{n\infty} = 0.106$ , in Argon	26
23. Lines of Constant Wire Temperature in the Stagnation Region of a Cylinder at $M = 6.3$ and $K_{n\infty} = 0.098$ , in Nitrogen	27
24. Lines of Constant Wire Temperature in the Stagnation Region of a Cylinder at $M = 6.3$ and $K_n = 0.012$ , in Nitrogen	27
25. Stagnation Line Profiles on Cylinders at $M_{\infty} = 5.4$ in Argon	29
26. Stagnation Line Profiles on a 0.0153 in. Diameter Cylinder in Nitrogen and Argon	30
27. Stagnation Line Profiles on Cylinders at $M_{\infty} = 6.3$ in Nitrogen	30
28. Lines of Constant Wire Temperature in the Stagnation Region of a Sharp $20^{\circ}$ Wedge at $M_{\infty} = 6.7$ in Nitrogen	31
29. Stagnation Line Profiles on a Sharp $20^{\circ}$ Wedge at $M_{\infty} \sim 6.5$ in Nitrogen	32
30. Lines of Constant Wire Temperature in the Stagnation Region of a Blunt $18^{\circ}$ Wedge at $M_{\infty} = 6.7$ in Nitrogen	32
31. Lines of Constant Wire Temperature in the Stagnation Region of a Cold, Blunt $18^{\circ}$ Wedge at $M_{\infty} = 6.7$ in Nitrogen	33
32. Stagnation Line Profiles on a Warm and Cold $18^{\circ}$ Blunt Wedge at $M_{\infty} \sim 6.5$ in Nitrogen	

# ILLUSTRATIONS (Continued)

	Page
33. Comparison of Measured and Calculated Free Molecule Equilibrium Temperature Along Stagnation Line of a Cylinder	36
34. Comparison of Measured and Calculated Density Along Stagnation Line of a Sphere	36
35. Comparison of Measured and Computed Cylinder Drag	38
36. Comparison of Measured and Computed Sphere Drag	38
37. Typical Autocorrelation and Cross Correlation for Small and Large $X/D$	43
38. Typical Power Spectral Densities for Small and Large $X/D$	43
39. Time Correlation Scale for Extended $X/D$	44
40. Radial Probe Locations Compared with Wake Width	44
41. Space Correlation Length	46
42. Mean Wake Velocity	49
43. Mean Wake Temperature	49
44. Convection Velocity Compared with Mean Wake Velocity	50
45. High Reynolds Number Turbulent Boundary Layer	56
46. Solution for Matching Point, $\eta_0$ vs. $(C_f R_s)^{1/2}$	60
47. Boundary Layer Thickness, $\frac{\delta}{\delta_0}$ vs. $\frac{x}{\delta_0}$	61
48. Skin Friction vs. $\frac{x}{\delta_0}$	62
49. Flow Field Sketch	73
50. Radial Enthalpy Variation	75



## ILLUSTRATIONS (Continued)

		Page
51.	Turbulent Wake Growth	76
52.	Slender Body Near Wake	78
53.	Comparison with Experiment of the Computed Pressure Distribution on a Rounded Backward Facing Step	79
54.	Detailed Flow Properties for a Boundary Layer Separating from a Rounded Backward Facing Step	81
55.	Computed Streamlines and Separation Shock Superimposed on Shadowgraph Corresponding to the Same Conditions	83
56.	Wall Pressure Near a Sharp Corner-Comparison of Theory with Experiment	85
57.	Experimentally Determined Flow Field in the Near Wake of a 20-degree Wedge; $M_\infty = 6$ , $Re_\infty H = 5.5 \times 10^4$ (Reference 5)	87
58.	Example of a Calculation of the Expansion of the Boundary Layer into the Near Wake by Rotational Characteristics	88
59.	Pressure Field in the Near Wake of a 20-degree Wedge at $M_\infty = 6$ by Rotational Characteristics	90
60.	Wake Neck Interaction Analysis	94
61.	Interacting Wake Neck Calculations Showing a Source Type Solution ( $Re_\infty H = 50,000$ )	95
62.	Interacting Wake Neck Calculation Showing a Sink Type Solution ( $Re_\infty H = 55,000$ )	96
63.	Results of Wake Neck Interaction and Comparison with Experiment	97
64.	Sensitivity of Wake Neck Solution to the Flow Above the Wake Shock	99

## SECTION I

### INTRODUCTION

The Reentry Physics portion of the Penetration Systems Studies contract has been a continuing analysis effort in the area of hypersonic flow phenomena with the goal of supporting missile detection and discrimination technology. The present contract has five tasks outlined below.

One task has centered around the development of the Bird Monte Carlo technique to describe the free molecule/continuum transitional flow field around hypersonic bodies and carry out associated wind tunnel measurements to compare the theory and experimental results. The purpose of the task is to be able to obtain accurate drag predictions, as well as estimates of the high altitude plasma sheath properties around a reentering body.

The remaining four tasks fall under the general heading of hypersonic wake and boundary layer technology. The second task has been the use of a ballistic range to make detailed hot wire measurements of turbulent correlation length and spectra in the wake of hypersonic pellets. In this task, various shaped pellets are fired past stationary single and double hot wire probes to obtain the above pertinent statistical as well as mean properties back along the length of the wake.

The third task is to examine the nonequilibrium turbulent boundary layer from the viewpoint of formulating a new low speed theoretical description, developing the appropriate low/high speed transformations and, finally, examining the effect of turbulence on chemical reactions. The fourth task has been the prediction of a particular downstream laminar wake case in order to study the "breakthrough" phenomena noted by L. N. Wilson, General Motors,<sup>(58)</sup> in a ballistic range.

Finally, an analysis of the near wake is being developed based on the Crocco-Lees critical point concept. This analysis considers the upstream body boundary layer effect as well as the pertinent base region

details. The near wake work is an outgrowth of the far wake turbulence analysis carried out during the previous contract periods. An analysis of the kind being developed is a crucial link in the prediction of the total flow field, including downstream wake, around a hypersonic vehicle.

The format followed in the report is to present brief summaries of the work where detailed reports have already been issued during the contract period. Where reports have not yet been issued, or are in preparation, as in the case of the High Altitude Drag Investigation, considerably more detail is presented here. A list of the previous reports issued under the present contract is given in Appendix I.

## SECTION II

### HIGH ALTITUDE DRAG INVESTIGATION

#### 2.1 INTRODUCTION AND BACKGROUND

Since radars now under development are predicted to have very accurate measurement capabilities, the drag and flow fields of reentry bodies at high altitude will become important considerations in the design of future penetration aid systems. For example, the drag and the nature of the drag change with altitude provide information about the vehicle. In addition, the electrons produced in the stagnation region persist at high altitude throughout the boundary layer on the body. This ionized layer shields the aft corner thereby affecting the radar return markedly and hence, plays an important part in the discrimination process. Thus, it is important to develop analytical methods for treating this transition regime and to obtain additional experimental information about it.

The transitional regime between continuum and free molecule flow has been and continues to be one that is difficult to treat either experimentally or theoretically. It is not surprising, then, that there are so few flow situations for which a comparison between theory and experiment has been possible. Most analyses have been confined to flows with simple boundary conditions, for instance Couette and Rayleigh flow, while the few experiments deal with quite different situations such as flows about bodies and free jet flow. The plane shock wave is, of course, a notable exception to this situation.

However, external supersonic flows about bodies are of greatest practical interest. The objective of the research reported here was the development of a new theoretical method of treating such flows, the direct Monte Carlo simulation technique (References 1, 2, 3), and a comparison of theoretical flow fields about several simple shapes with those obtained in a low density wind tunnel.

In addition, a comparison of the Monte Carlo drag calculations on cylinders and spheres with measured drag has been made.

## 2.2 DESCRIPTION OF THE MONTE CARLO METHOD

Low density supersonic flow about cylinders, spheres, sharp wedges, and sharp cones has been studied in the free stream Knudsen number,  $K_n = \frac{\lambda}{D}$ , range from 0.025 to 100 and at Mach numbers from 3.8 to 11 using a Monte Carlo direct simulation technique. This method was originated by Prof. G. A. Bird of the University of Sydney. (References 1, 2, 3) Prof. Bird was consultant to this project during the past year.

In the direct simulation technique a small number of molecules is set in uniform motion in Maxwellian equilibrium. A body is instantaneously inserted in the stream and the motion of the molecules is computed in a region surrounding the body. The molecular paths between collisions are computed exactly but the collisions are treated statistically. The calculation procedure consists of holding all molecules motionless for a time interval,  $\Delta t_m$ , small compared to a molecular mean collision time,  $\bar{t}$ , while collisions are computed everywhere in the field. Molecules are then allowed to move with their new velocities for the time interval  $\Delta t_m$ , and are then held motionless in their new positions while another collision cycle takes place. Collisions are computed by statistical sampling as follows:

- a) An estimate of the local mean collision time  $\bar{t}$  is obtained from the local density and a characteristic molecular velocity;
- b) By comparing  $\Delta t_m$  and  $\bar{t}$ , the appropriate number of collisions to occur during  $\Delta t_m$  is known;
- c) Pairs of molecules are selected at random from a small spatial region of extent  $\sim \lambda$  (called a cell) and are allowed to collide with probability proportional to their relative velocity. This sampling scheme produces an average distance between collisions equal to the local mean free path;
- d) For pairs of molecules which have been accepted for collision, a line of impact and azimuth in the center of mass frame of reference are selected at random and the conservation laws are applied.

The initial flow field evolves to an approximate steady state in this manner. Accurate steady state values of flow field properties and body

forces are determined by continuing this collision process through a large number of cycles, computing a cumulative average of the instantaneous values. In this way, a small number of molecules can be used to represent a large number with accuracy dependent only upon the capacity of available computing machinery and the accuracy of the molecular collision model and surface reflection model.

In addition to the net force on the body, this method provides a considerably detailed description of the flow, for example:

- a) flow field properties: density, temperature, velocity, etc., everywhere in the region surrounding the body;
- b) variation of properties on the body surface; e. g., pressure, skin friction, number flux, etc.;
- c) heat transfer to the body;
- d) the distribution function of the gas.

A more detailed description of the method is given in Appendix II. In essence, the method consists of constraining a system of a small number of molecules to behave, in the mean, as they would if all the other molecules present in an actual gas were present. The Boltzmann equation is thus solved, in some mean sense, for a rigid elastic sphere gas. Effects of fluctuations are removed by continuing the calculation until a large sample of values for any particular flow field property has been gathered. The mean of this sample is then an estimate of the flow field property, to which some uncertainty, or variance, must be attached. A more detailed examination of the statistical aspects of the calculation is given in Appendix III.

In the present work, an extensive development of this method has been carried out. The theoretical basis has been further clarified, and the computational techniques have been greatly improved, reducing computational time by an order of magnitude. Some innovations to the technique have been developed; for example:

- 1) The cell size, i. e., the size of the small spatial regions in which sampling is done, may now be varied over the field, to allow finer definition of regions of high gradients, such as the stagnation region.

- 2) For axisymmetric calculations, where the population density for molecules in our two-dimensional computational field must increase as the distance from the axis in order to simulate axisymmetric space, a system has been devised of weighting molecules proportional to their distance from the axis, thus markedly reducing the required computer storage.
- 3) For two-dimensional flows, the free molecule equilibrium temperature can be computed at arbitrary points in the flow. Record is kept of the energy flux and number flux to a small circle in the flow, from which the free molecule recovery temperature can be computed, for an assumed type of reflection process. Since molecules pass through the circle and do not collide with it, there is no disturbance to the flow.

## 2.3 MONTE CARLO CALCULATIONS

### 2.3.1 Tabulation of Results

Digital computer programs have been written to compute the flow about five simple shapes:

- flat plate
- cylinder
- sphere
- sharp wedge of arbitrary apex angle
- sharp cone of arbitrary apex angle

A list of the computer results obtained to date is shown in Table I. (No results are presented for the flat plate.) All of these results are quantitatively accurate to a certain degree. However, the degree varies somewhat and for that reason some are considered preliminary, meaning that either the sample size is smaller than desirable or the effect of some parameter such as field size or the number of molecules in each cell should be investigated further. Most of the results marked preliminary were executed by Professor Bird on the IBM 7040 computer in Sydney. The computer used for most of the other results was the CDC 6600. Two of these results, the cylinder calculation at  $K_n = 1.0$  and  $0.3$ , were investigated extensively to determine the magnitude of statistical scatter and the effect of the previously mentioned parameters such as field size and movement time on the results. This matter is discussed in greater detail in Appendix III; however, it can be said in general that within the

Table I. Computer Results

	Knudsen Number	Speed Ratio	Body Temp.	
Cylinder	100	5	$T_{t\infty}$	
	1.0	5	$T_{t\infty}$	
	0.3	5	$T_{t\infty}$	
	0.2	5	$T_{t\infty}$	Preliminary
	0.1	10	.25 $T_{t\infty}$	Preliminary
	0.025	5	$T_{t\infty}$	Preliminary
	0.025	10	.49 $T_{t\infty}$	Preliminary
Sphere	100	5	$T_{t\infty}$	
	0.26	5	$T_{t\infty}$	
	0.03	3.5	$T_{t\infty}$	Preliminary
20° Sharp Wedge	0.3	5	.09 $T_{t\infty}$	
22.5° Sharp Cone	0.1	5	$T_{t\infty}$	

range investigated the results are not very sensitive to changes in field size, movement time and number of molecules per cell. The statistical scatter decreases with the square root of the sample size; e. g. ,

$$\sigma_{C_D} \sim \frac{1}{\sqrt{SS}} \cdot C_D$$

where  $\sigma_{C_D}$  is the standard deviation. A list of the sample size and standard deviation of the drag coefficient for the cases in Table I is given in Table II. The largest value of  $\sigma_{C_D}/C_D$  there is 2.6%. In general, for a given amount of computation time, drag coefficient is the most accurately determined property of the flow field, since it is a gross feature of the flow. Details of the flow such as the distribution function at a point may still show appreciable scatter when the drag is quite well converged.

In the following sections some of the results in Table II will be examined in detail.

### 2.3.2 Distribution Function Calculations

Liepmann (Reference 11) in a recent study of the Bhatnager-Gross-Krook model applied to a plane shock wave concluded that "the distribution function within the layer is bi-modal, exhibits the gradual change



Table II. Sample Size Standard Deviation of Drag Coefficient

	$K_n$	S	$T_b$	Sample Size	$C_D$	$\frac{\sigma_{C_D}}{C_D} (\%)$	Remarks
Cylinder	100.0	5	$T_{t_\infty}$	2,193	2.99	2.1	1 run
	1.0	5	$T_{t_\infty}$	4,960	2.44	1.4	3 runs
	0.3	5	$T_{t_\infty}$	31,381	1.85	0.5	4 runs
	0.2	5	$T_{t_\infty}$	2,275	1.78	2.1	2 runs
	0.1	10	$.25 T_{t_\infty}$	3,090	1.64	1.8	1 run
	0.025	5	$T_{t_\infty}$	1,878	1.57	2.3	1 run
	0.025	10	$.49 T_{t_\infty}$	2,595	1.57	2.0	1 run
Sphere	100.0	5	$T_{t_\infty}$	1,602	2.82	2.5	1 run
	0.26	5	$T_{t_\infty}$	1,965	1.88	2.3	1 run
	0.03	3.5	$T_{t_\infty}$	4,769	1.41	1.5	3 runs
20° Sharp Wedge	0.3	5	$.09 T_{t_\infty}$	5,669	1.67	1.3	1 run
22.5° Sharp Cone	0.1	5	$T_{t_\infty}$	1,473	1.29	2.6	1 run

from the molecular beamlike behavior ahead to a Maxwellian distribution behind the shock. The effect of the fast molecules is noticeable even many free paths behind the shock." Liepmann's results are shown in Figure 1, where the distribution function  $f(u, \sqrt{v^2 + w^2})$  is plotted versus thermal velocity  $u/v_{m_\infty}$  for several locations in the shock wave. As we proceed into the shock wave,  $f(u)$  departs from Maxwellian shape, the peak shifting to the right to lie near an absolute velocity equal to the free stream velocity; e. g., the peak at  $x = +2$  lies at  $u/v_{m_\infty} = 6.3$ , adding  $\bar{U}/v_{m_\infty} = 3.0$  yields an absolute velocity  $\bar{U}/v_{m_\infty} = 9.3$  which is nearly the free stream Mach number. The sharp peak at positive thermal velocity thus represents a cluster of molecules which haven't suffered enough collisions to lose their memory of the free stream. Deep in the shock layer the bi-modal shape appears. The same qualitative behavior of the distribution function is evident in the Monte Carlo calculations of the shock layer in front of a body. In Figure 2 is shown the distribution function  $f(u)$  at several locations along the stagnation line in front of a sphere at  $K_n = 0.26$ ,  $S = 5$ . In the free stream  $f(u)$  is very close to Maxwellian; and as we proceed toward the body, the bi-modal shape appears.

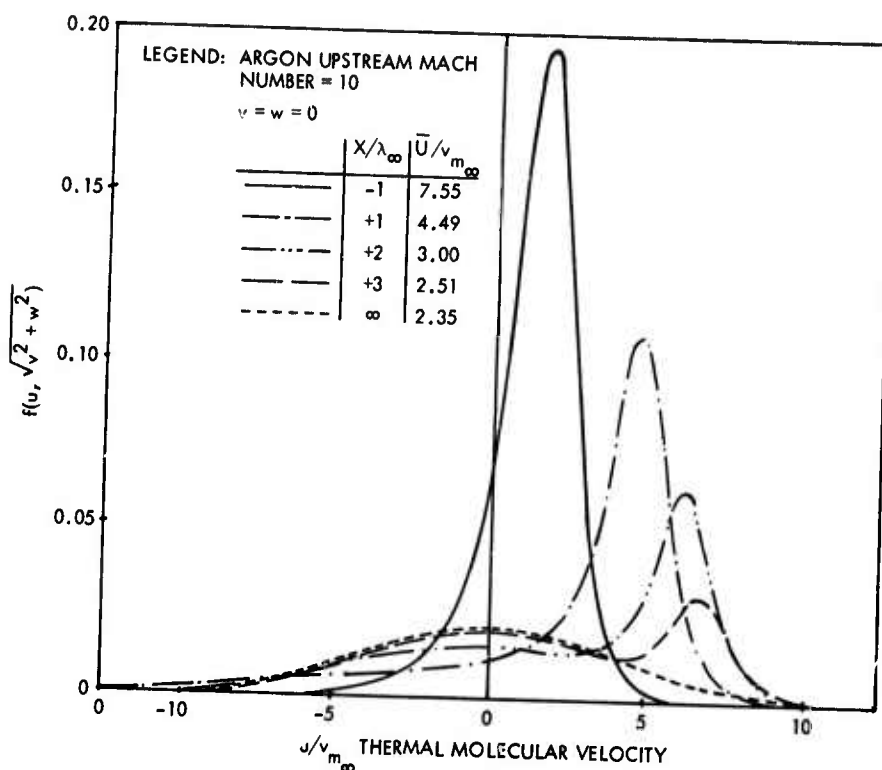


Figure 1. Distribution Function in Plane Shock Wave Krook Model Numerical Solution (Ref. 11)

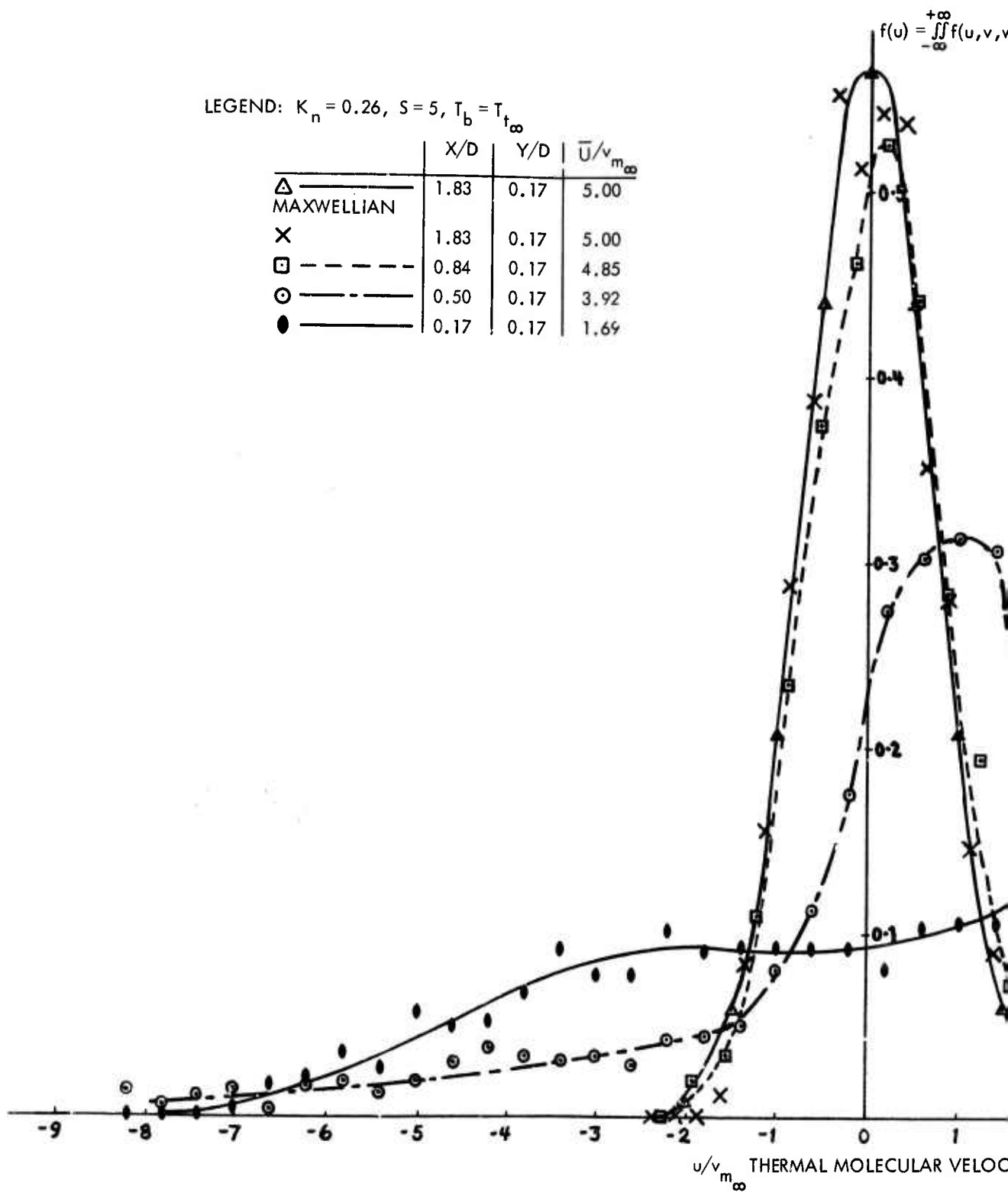
In Figure 3 comparison is made between the calculated distribution function in the uniform stream and a Maxwellian at the free stream temperature, again with very close agreement. The Monte Carlo collision calculation does produce a Maxwellian distribution when the flow is in equilibrium, as it should.

### 2.3.3 Drag Convergence with Sample Size

Some examples showing the way in which the drag coefficient converges are shown in Figures 4 and 5 for a cylinder and sharp cone. The sample size required for convergence to a given level of accuracy will vary with Knudsen number and body shape. Bluff shapes and low Knudsen numbers require a larger sample than slender shapes and high Knudsen numbers, because bluff bodies and low  $K_n$  cause higher gradients in the flow, hence more dispersion from the molecular distribution in the free stream. In Figure 4 the results of several calculations with different values of field size and initial number of molecules per cell are shown.

LEGEND:  $K_n = 0.26$ ,  $S = 5$ ,  $T_b = T_{t\infty}$

	X/D	Y/D	$\bar{U}/v_{m\infty}$
$\Delta$ ———	1.83	0.17	5.00
MAXWELLIAN			
X	1.83	0.17	5.00
$\square$ - - - -	0.84	0.17	4.85
$\circ$ - - - -	0.50	0.17	3.92
$\bullet$ ———	0.17	0.17	1.69



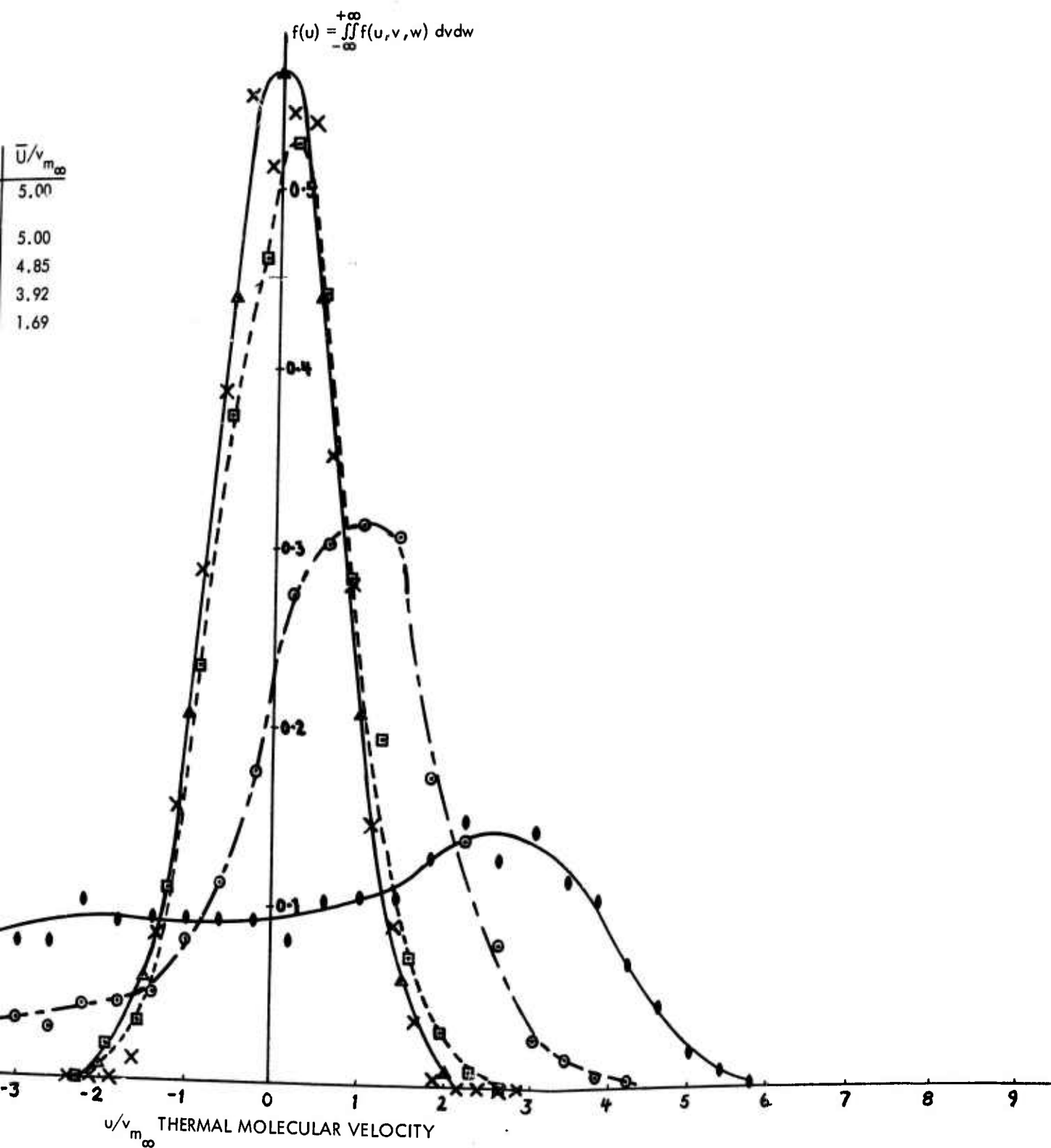


Figure 2. Monte Carlo Calculation of the Distribution Function on Stagnation Line of a Sphere

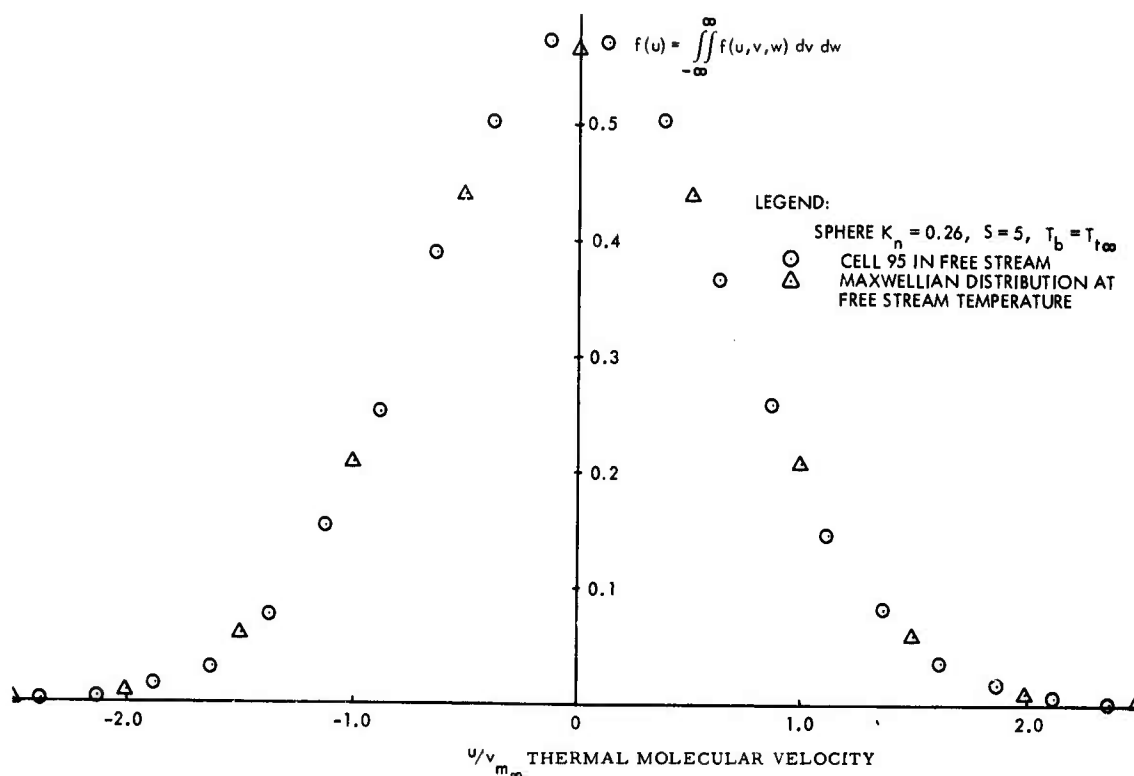
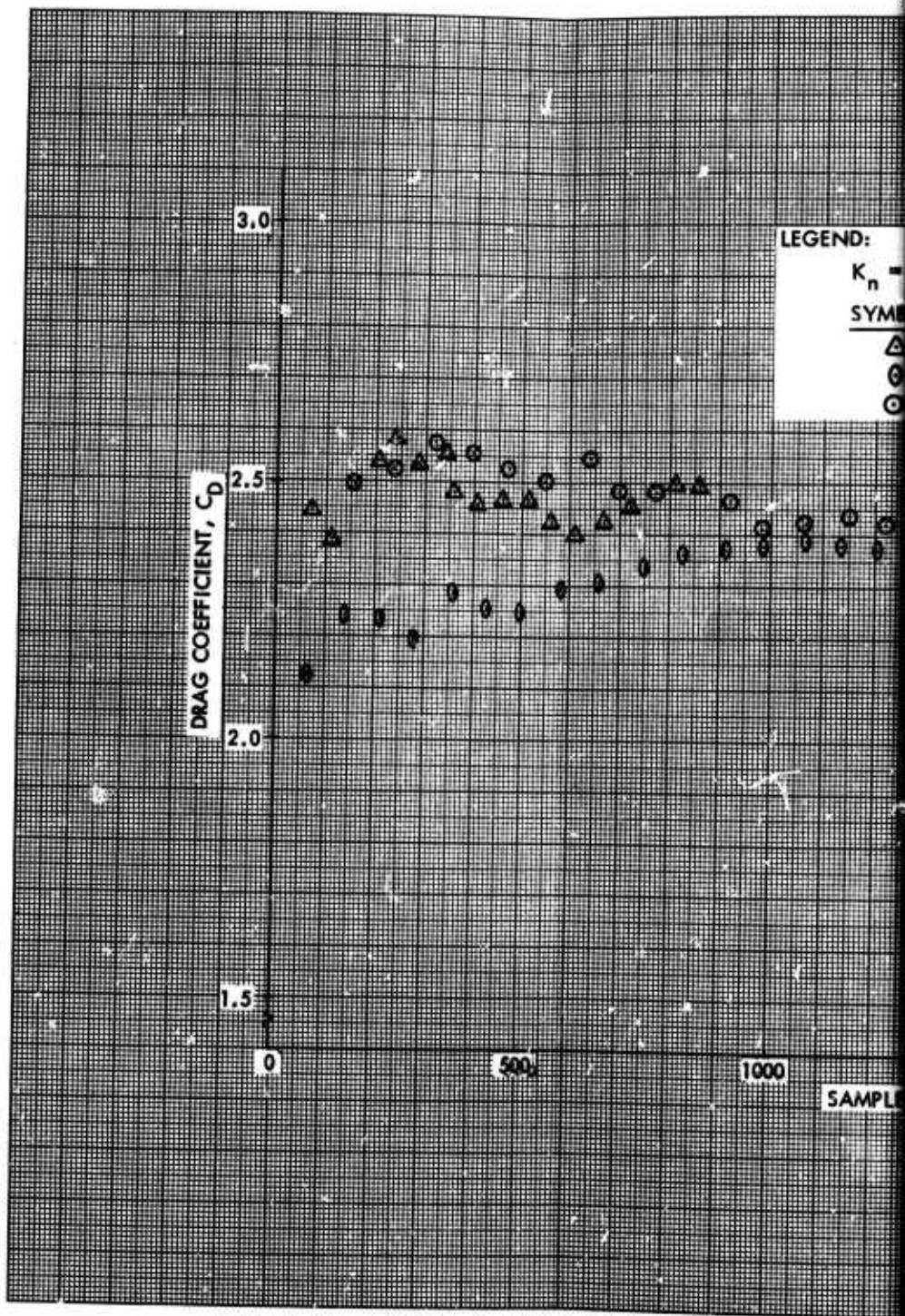


Figure 3. Comparison of Calculated Equilibrium Distribution Function with a Maxwellian

A similar but more extensive investigation for a cylinder at  $K_n = 0.3$  is shown in Figure 6 and in Figure 7 where one of the cases of Figure 6 is continued out to an extremely large sample size. At the end of the computer run in Figure 7 a total of 600,000 molecular collisions in the field had been computed. The variation of the parameters in these comparisons is not completely systematic and it is impossible to completely isolate the effect of any one parameter. However, it seems quite clear that within the range of variation we have investigated their effect is not large and further that after something like 2000 to 4000 molecules have struck the body the drag estimate has converged enough for practical purposes.





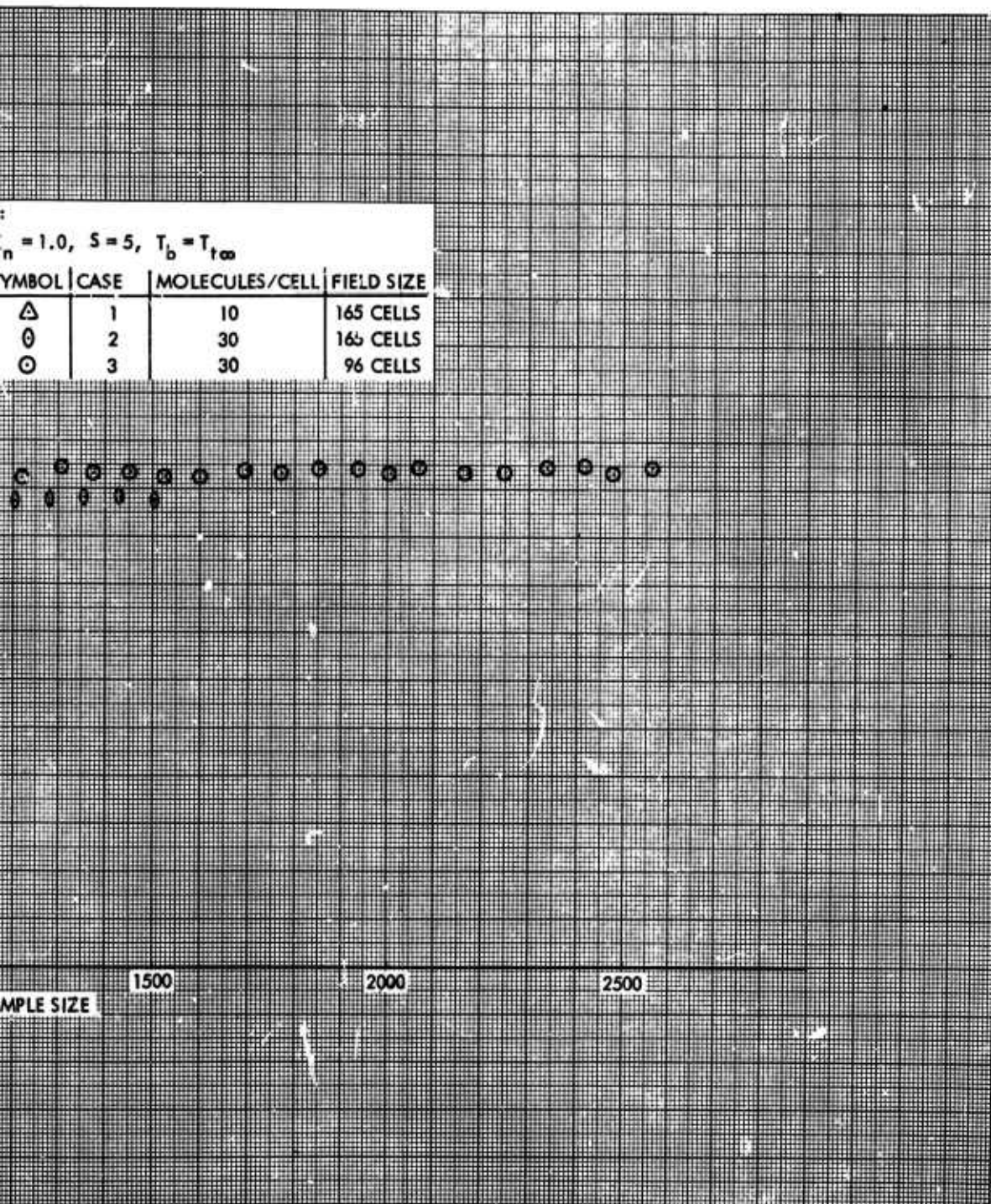


Figure 4. Cylinder Drag Coefficient vs Sample Size

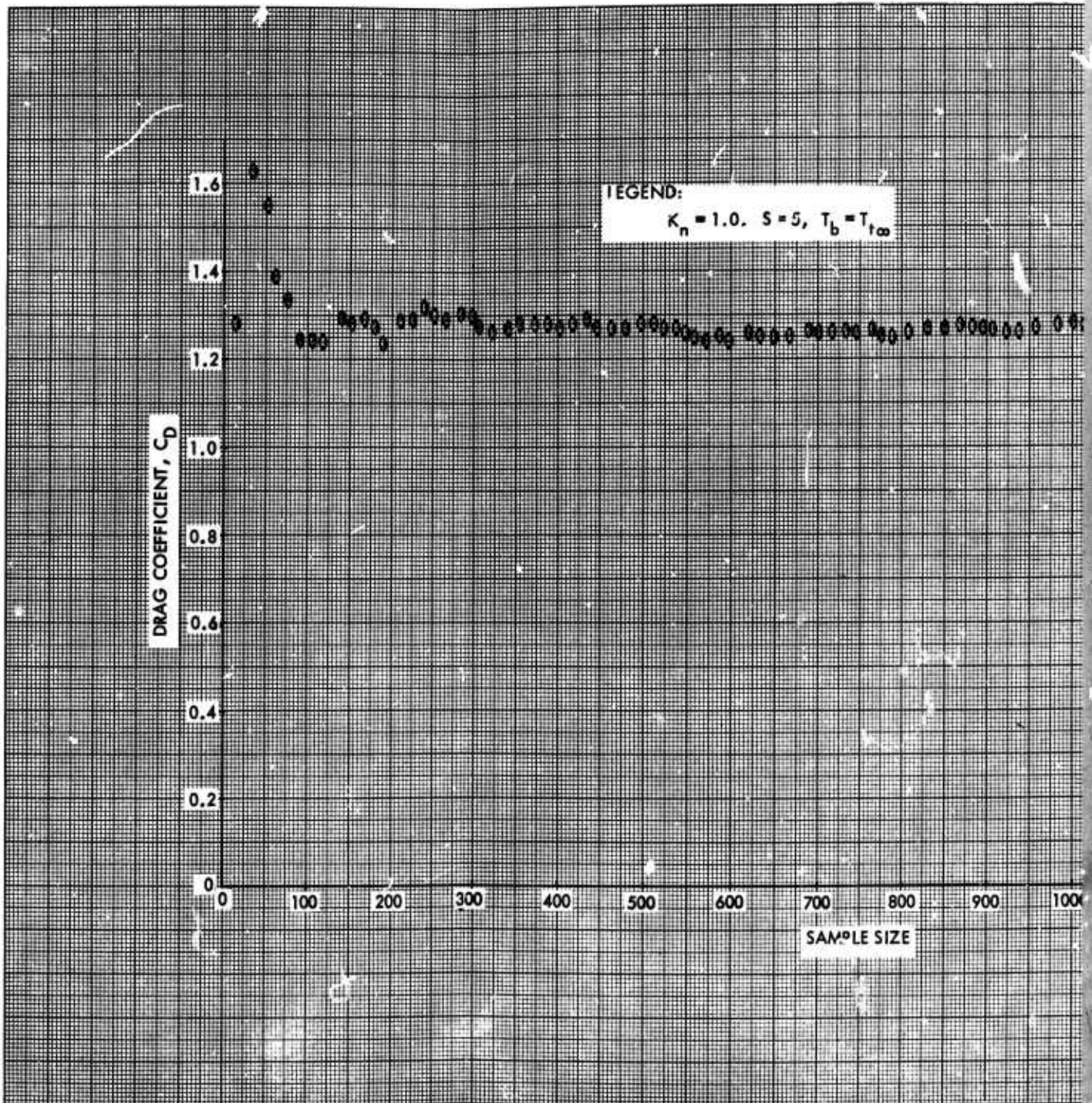


Figure 5. 22.5'



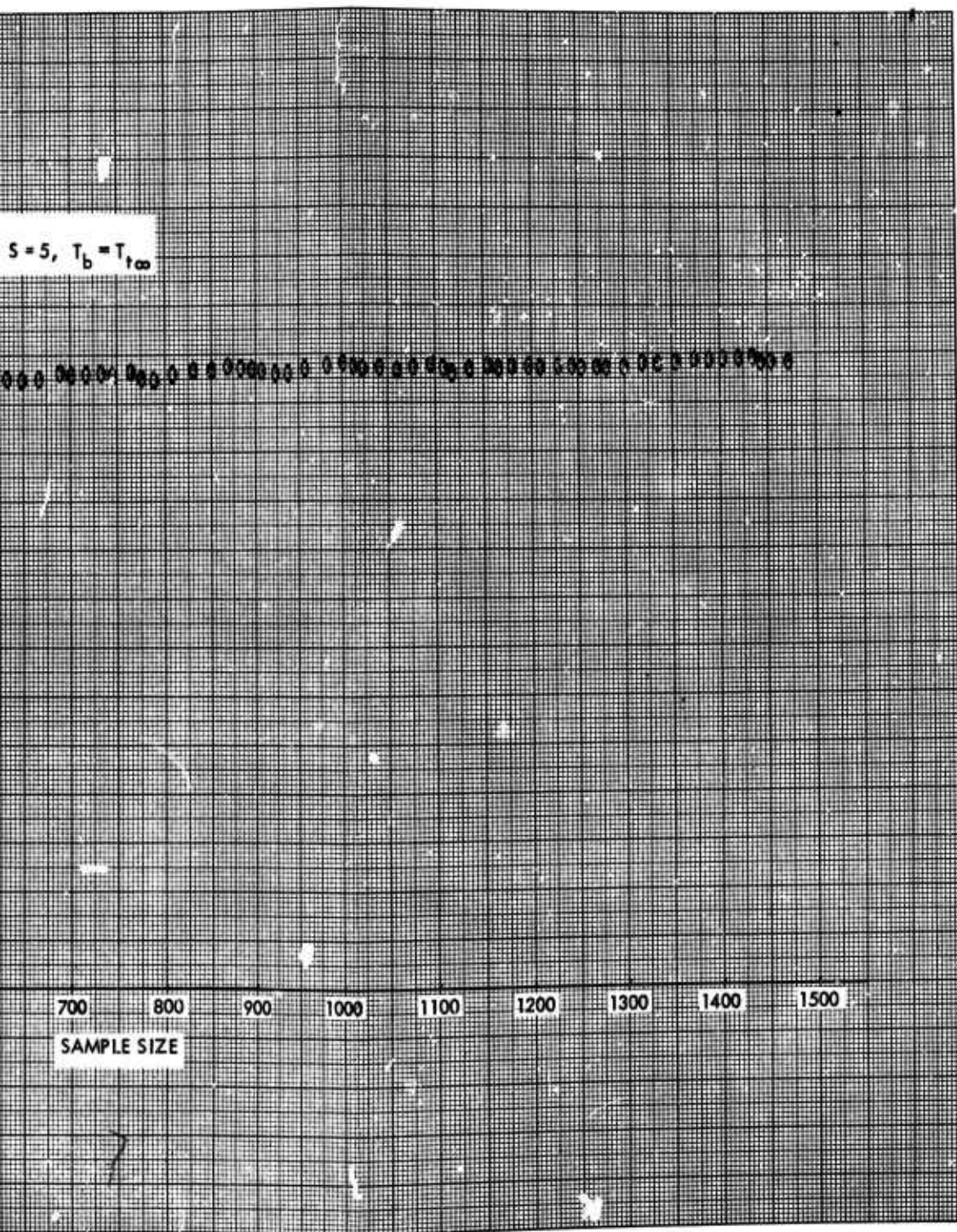
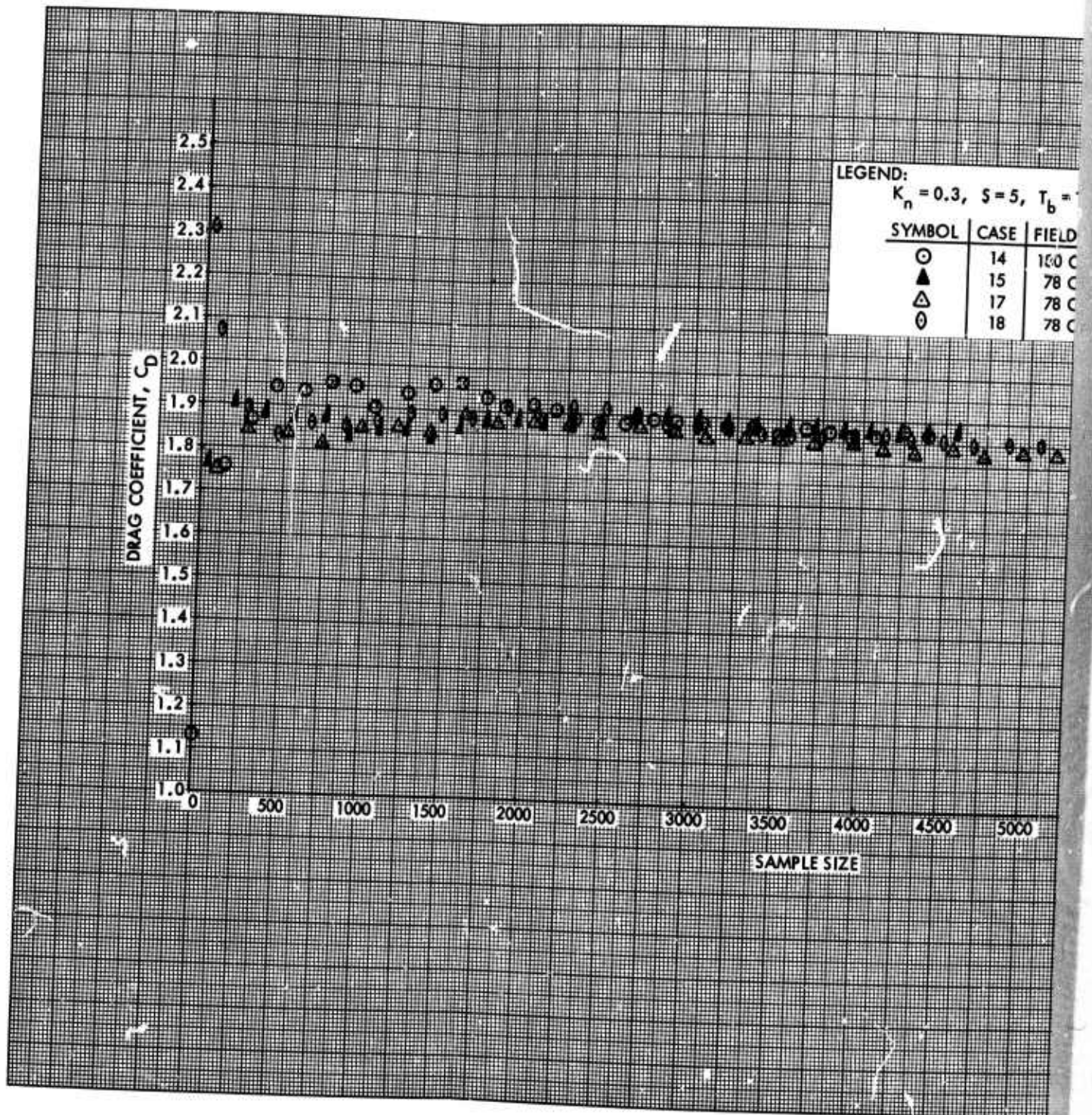


Figure 5.  $22.5^\circ$  Sharp Cone Drag Coefficient vs Sample Size



Figure



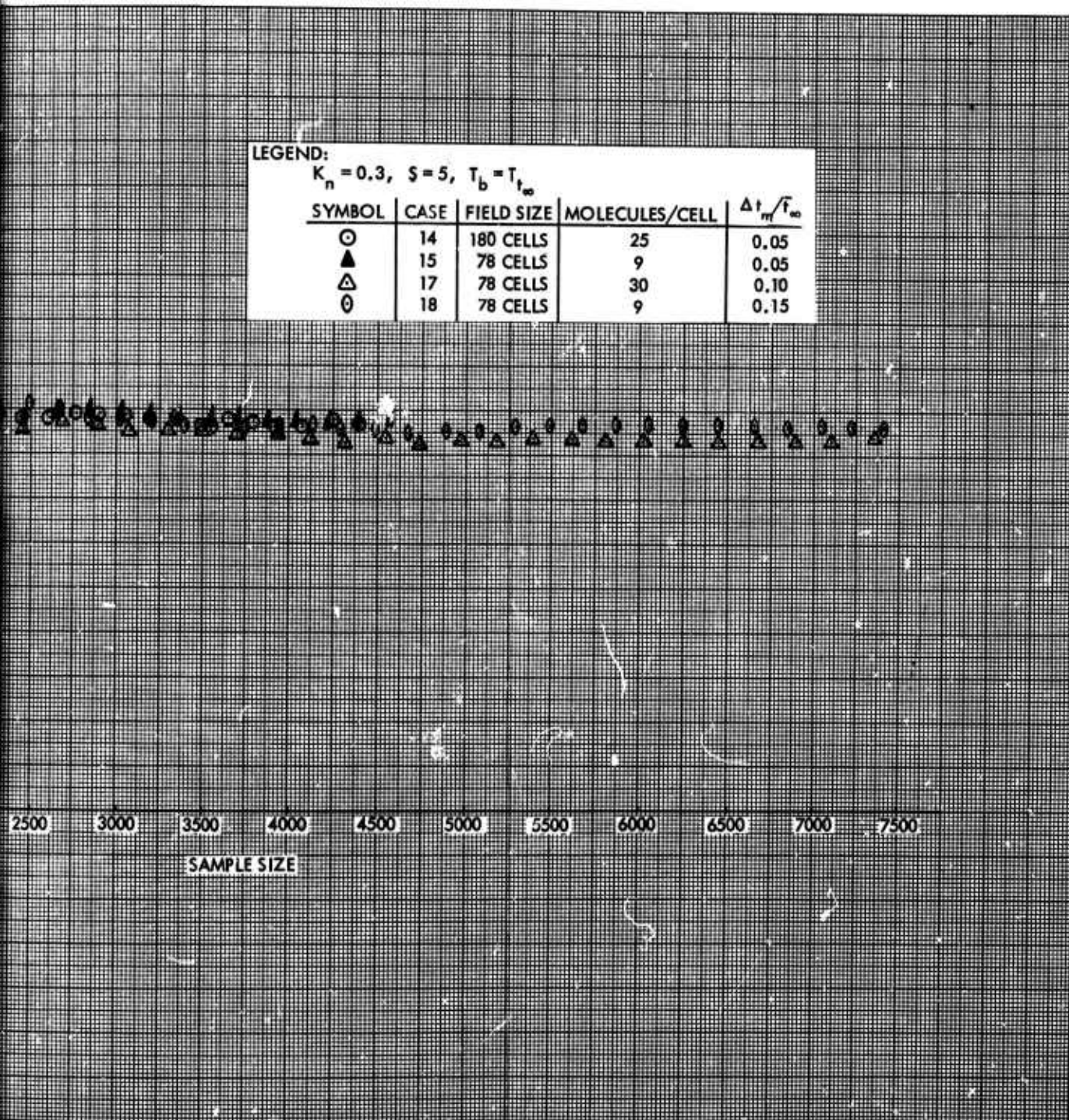


Figure 6. Cylinder Drag Coefficient vs Sample Size

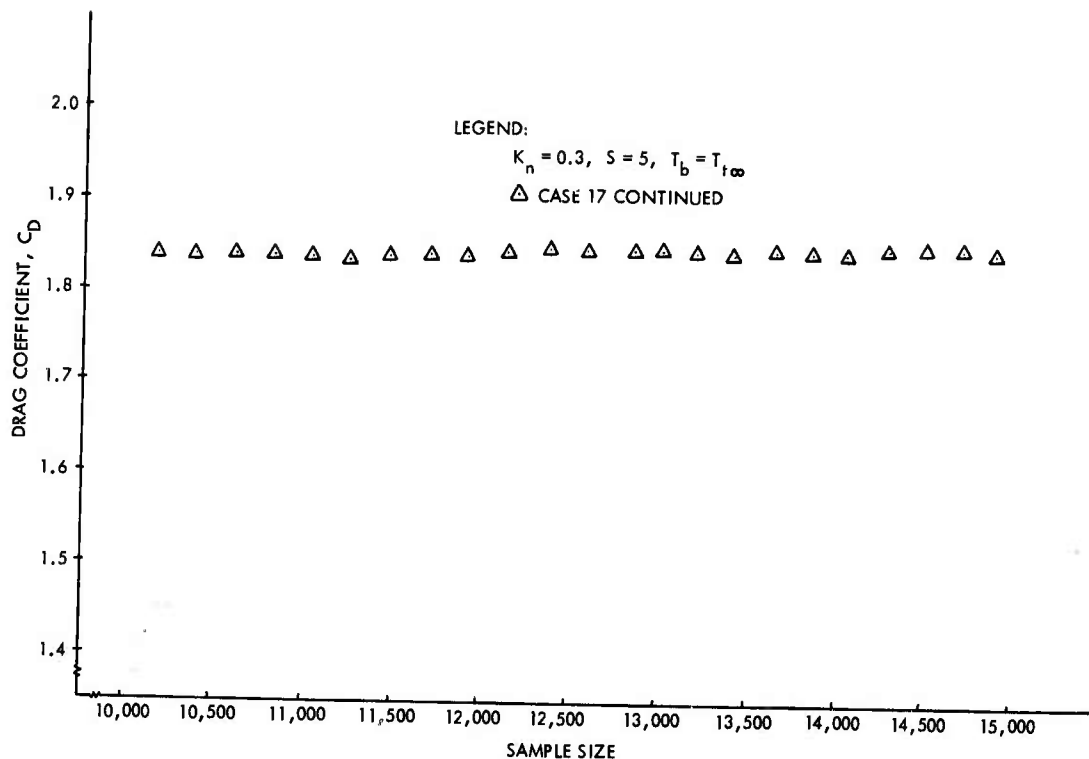


Figure 7. Cylinder Drag Coefficient vs Sample Size, Case 17 Continued

#### 2.3.4 Some Typical Flow Field Results

A collection of flow field results is shown in Figure 8 through 13 for a cylinder, sphere, sharp wedge and sharp cone.

The cylinder calculation is at  $K_n = 0.3$ ,  $S = 5$ ,  $T_b = T_{t\infty}$ . The arrangement of the spatial cells is shown in Figure 8 and constant density and temperature contours are shown in Figure 9 and 10. The Reynolds number for this case is 27, based on free stream conditions and cylinder diameter. The shock layer is a thick viscous region extending something like  $8\lambda_\infty$  in front of the body. Shock layer profiles near the stagnation line for this and other cases will be shown in the next section. There is a

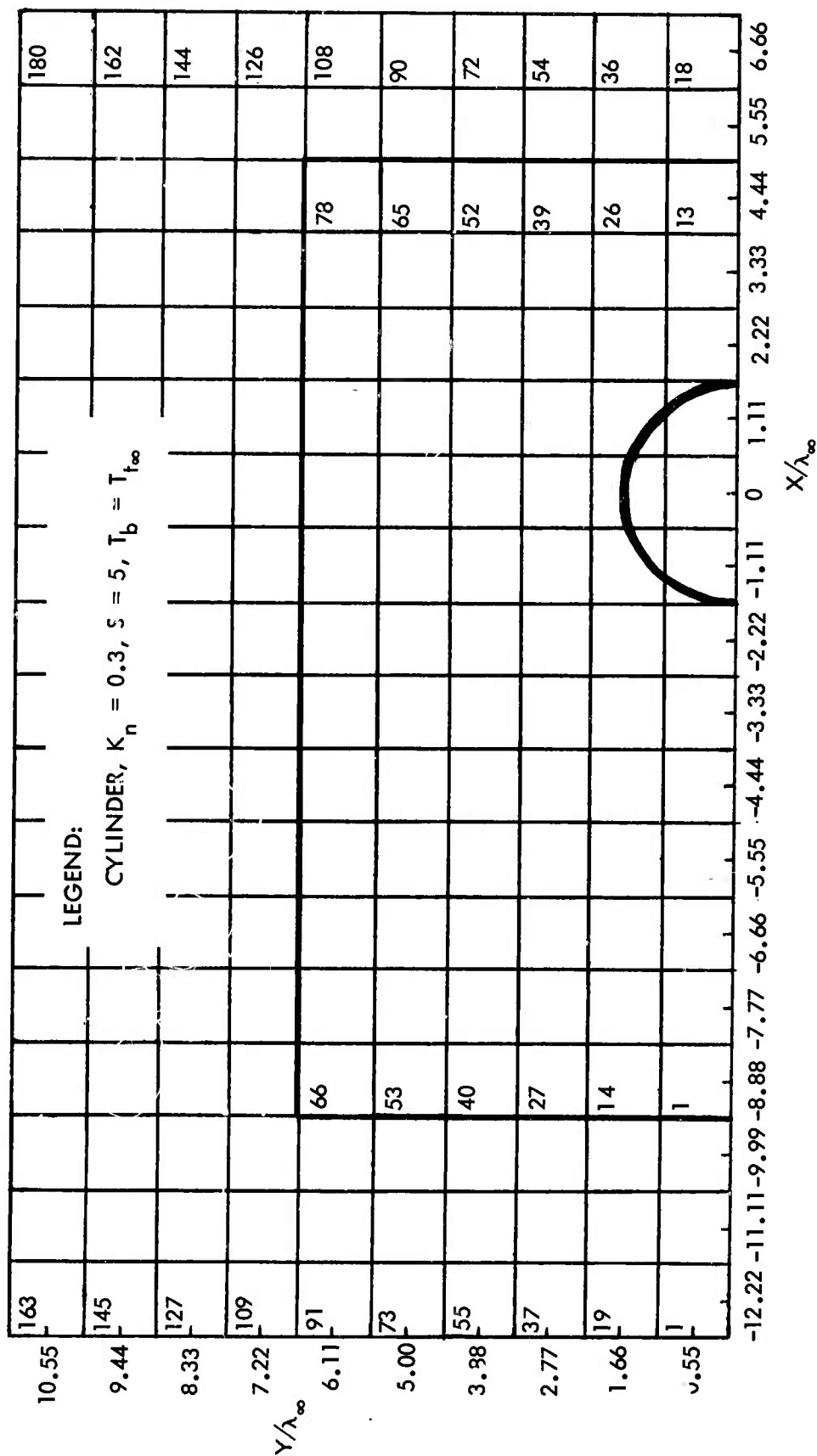


Figure 8. Cell Arrangement

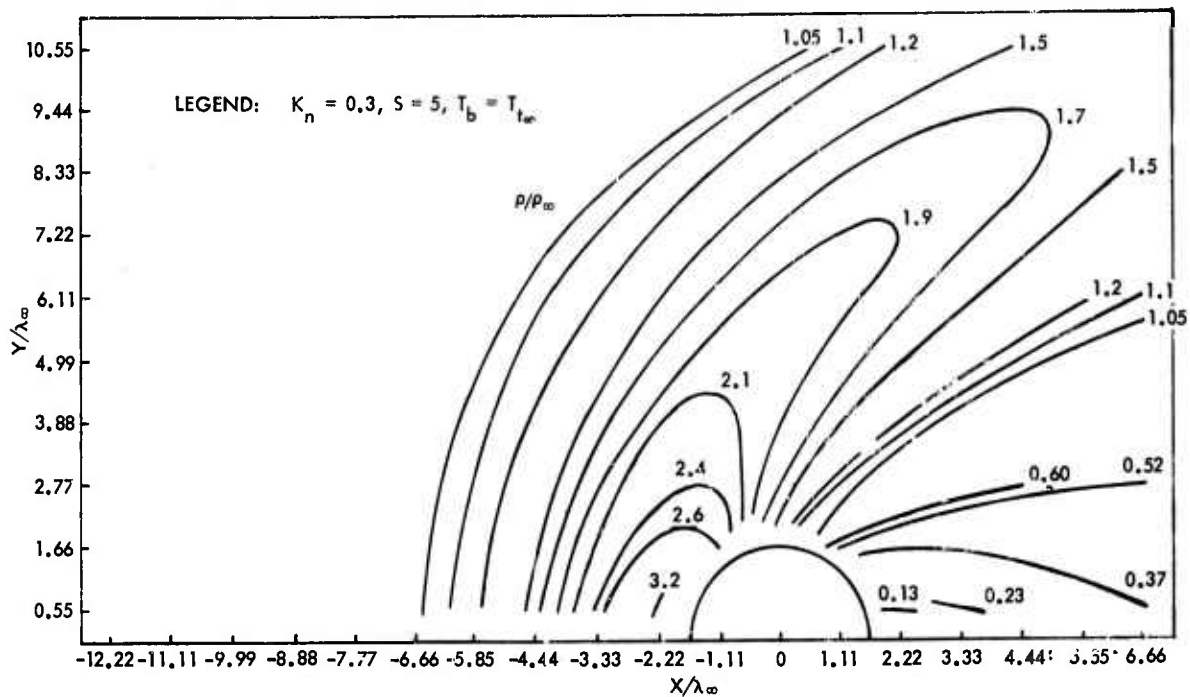


Figure 9. Density Contours in Flow Field of a Cylinder

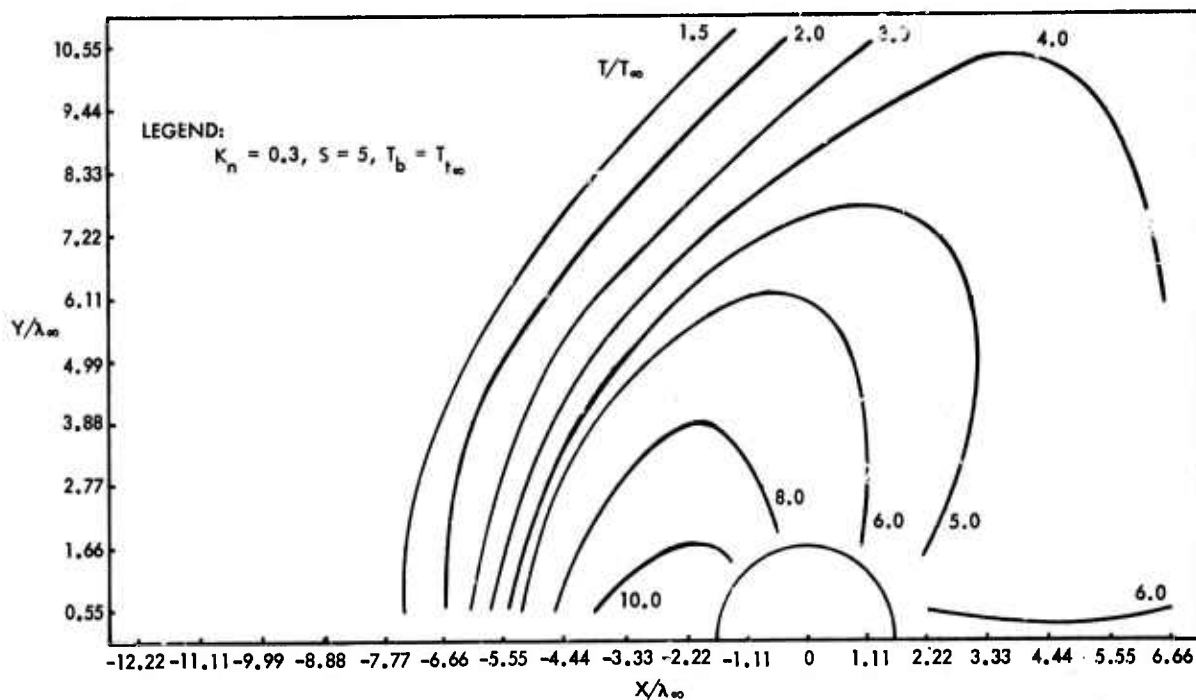


Figure 10. Temperature Contours in the Flow Field of a Cylinder

large lateral extent to the disturbance and a very low density wake behind the body spreading initially at something like  $20^\circ$ .

Density contours about a sphere at  $K_n = 0.26$ ,  $s = 5$ ,  $T_b = T_{t\infty}$ , Figure 11, show similar features with the upstream and lateral extent of the disturbance reduced, as would be expected.

Density contours about a  $20^\circ$  sharp wedge cooled to  $T_b = 0.09 T_{t\infty}$  and a  $22.5^\circ$  sharp cone held at  $T_b = T_{t\infty}$  are shown in Figure 12 and 13.

### 2.3.5 Some Typical Shock Layer Profiles

Shock layer profiles of density, temperature, velocity and total enthalpy are presented for cylinders and spheres over Knudsen number

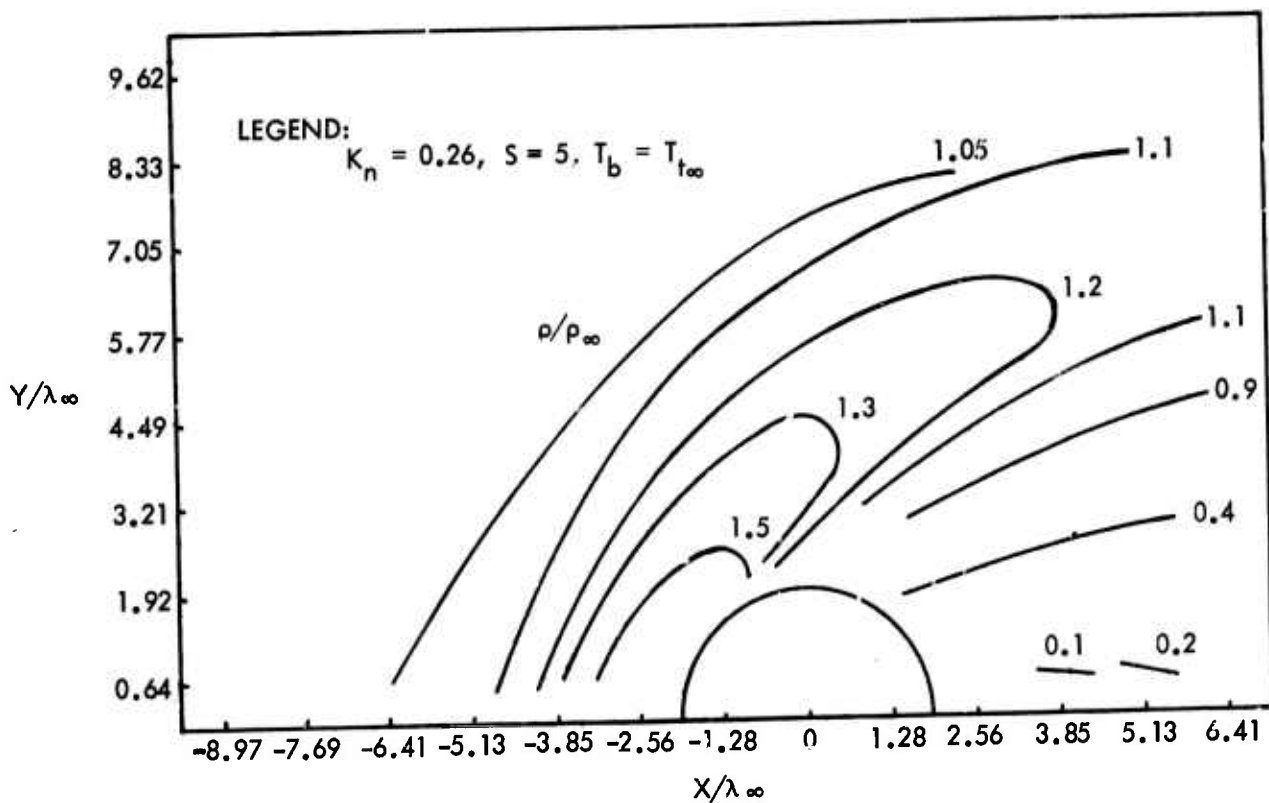


Figure 11. Density Contours in Flow Field of a Sphere

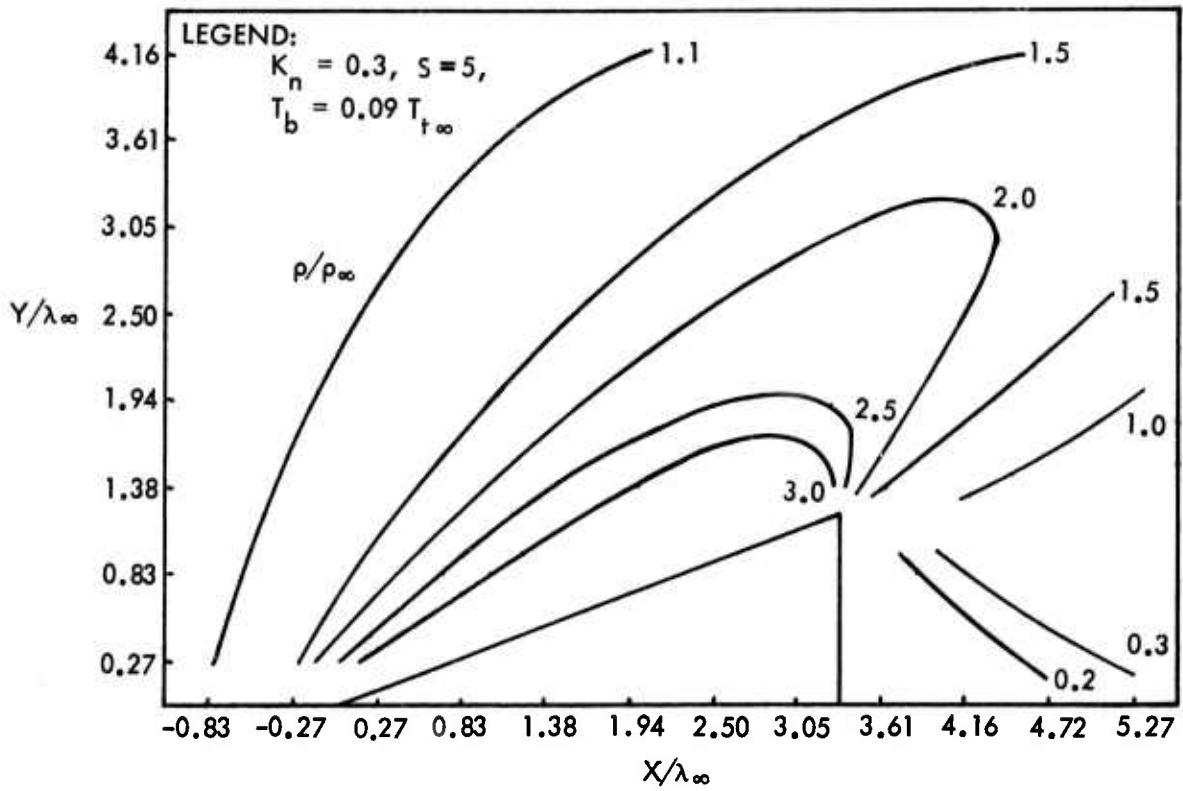


Figure 12. Density Contours in the Flow Field of a  $20^\circ$  Sharp Wedge

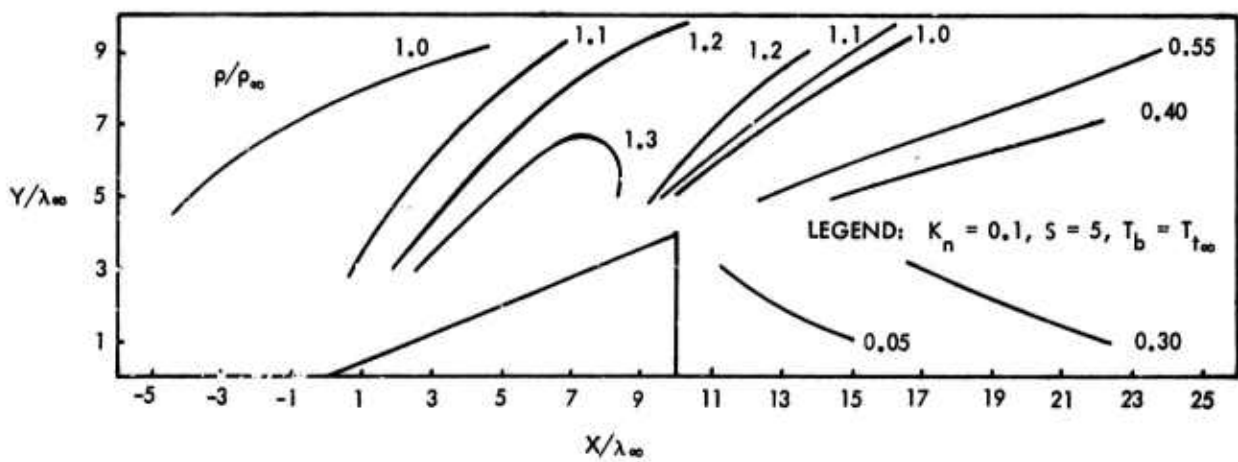


Figure 13. Density Contours in the Flow Field of a  $22.5^\circ$  Sharp Cone



range 0.025 to 0.3. The general structure of the layer agrees with what one would intuitively expect in that a thick, viscous shock wave is present and, for a cooled body, a thermal boundary layer exists.

In Figures 14 through 18 the variation of density, temperature, velocity and total enthalpy through the shock layer on the stagnation line is shown for a cylinder at  $K_n = 0.3$  and 0.025 and a sphere at  $K_n = 0.26$ .

Temperature appears to be a more sensitive property to detect the beginning of the disturbance. The temperature shock layer is  $\sim 9\lambda_\infty$  thick for the cylinder at  $K_n = 0.3$  (Figure 14) and  $\sim 6\lambda_\infty$  thick for the sphere at  $K_n = 0.26$  (Figure 15).

Two results are presented at  $K_n = 0.025$  for a cylinder, one at  $s = 5$  with  $T_b = T_{t_\infty}$ , Figure 17, and another at  $s = 10$  with  $T_b = 0.49 T_{t_\infty}$ , Figure 18. The hot cylinder temperature profile has a plateau at the free stream total temp  $T_{t_\infty}/T_\infty = 11$  which is reached at about half way through the shock layer. The Reynolds number  $Re_{D_\infty}$  was 364. This result still shows an appreciable amount of scatter and is considered preliminary.

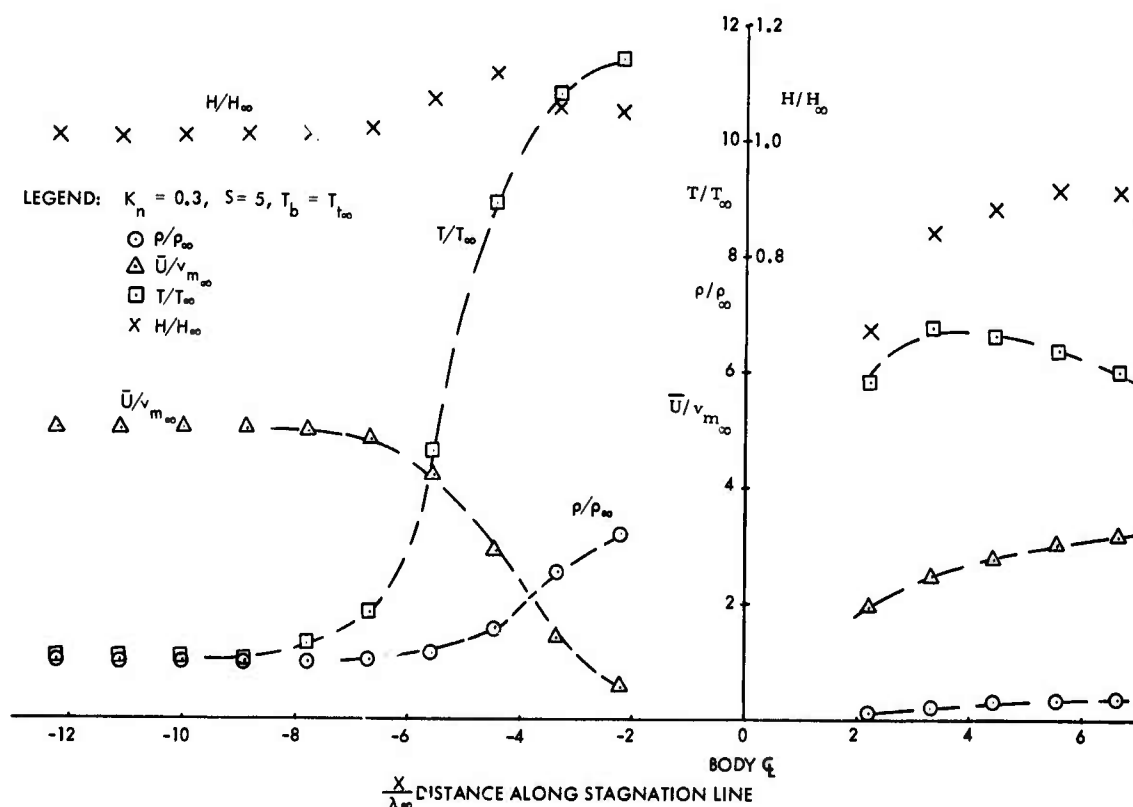


Figure 14. Cylinder Stagnation Line Profiles

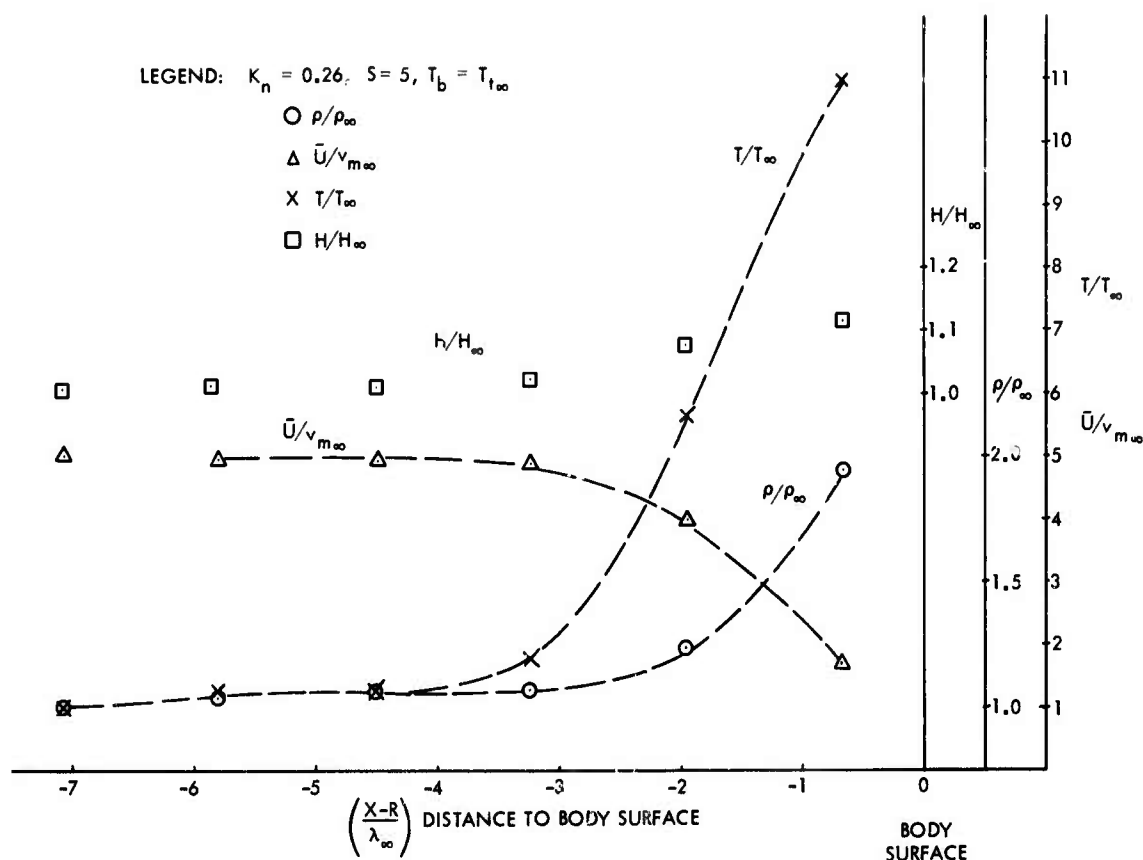


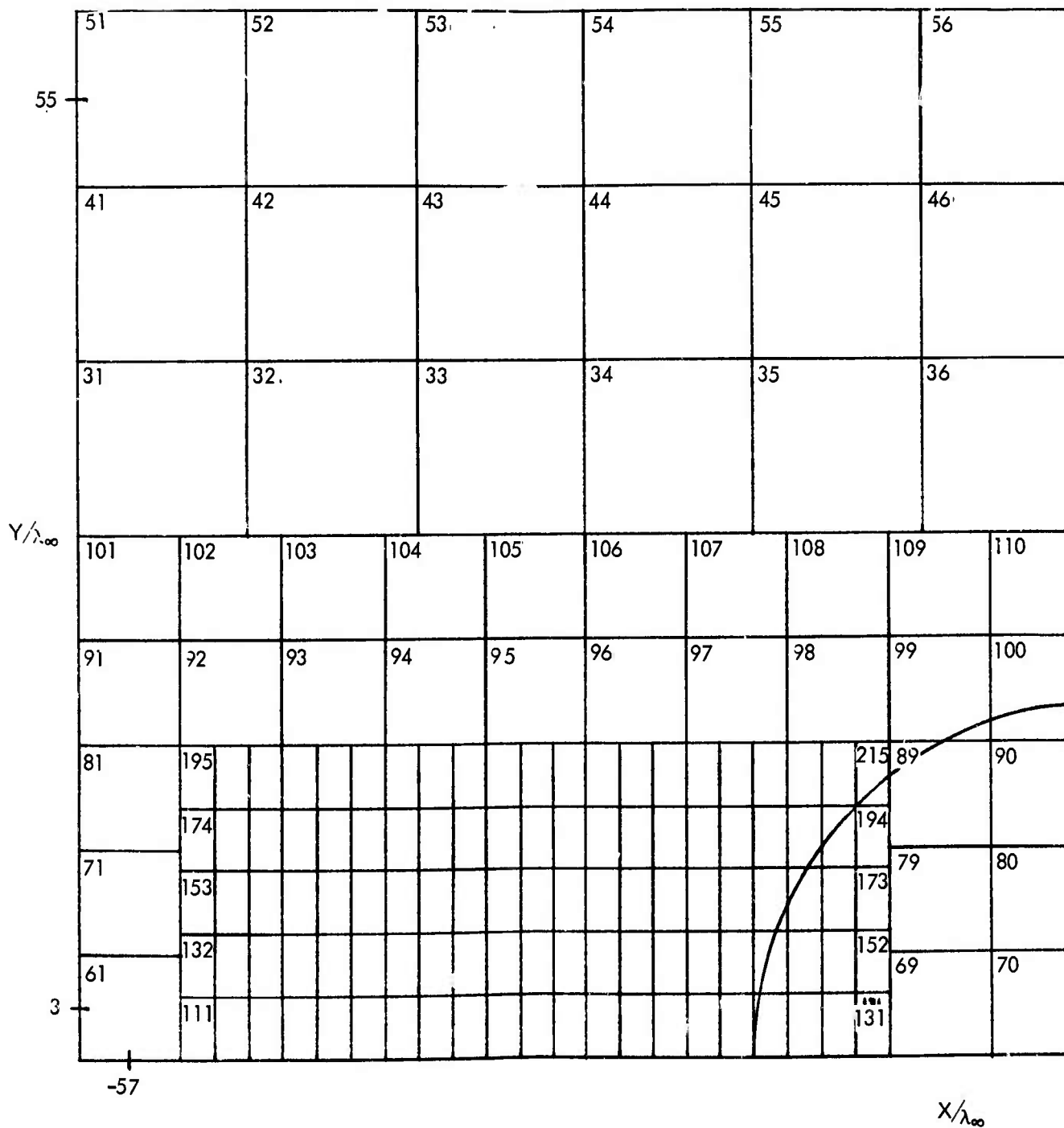
Figure 15. Sphere Stagnation Line Profiles

For the cooled cylinder, the stagnation line temperature rises to the free stream total temperature  $T_{t\infty}/T_\infty = 11$  about half way thru the shock layer and then falls in a thermal boundary layer to the body temperature.  $Re_{D_\infty} = 708$  for this case. This result shows considerable scatter. For both results the velocity profile resembles that for a completely merged viscous layer.

For all these results the total enthalpy rises through the shock layer to something like 10% above the free stream value near the body. This result is still being studied.

The stagnation line properties for a sphere at  $K_n = 0.03$ ,  $S = 3.5$  and  $T_b = T_{t\infty}$  are shown later in Figure 34.

CYLINDER  $K_n = 0.025$ ,  $S =$



CYLINDER  $K_n = 0.025$ ,  $S = 5$ ,  $T_b = T_{t_\infty}$

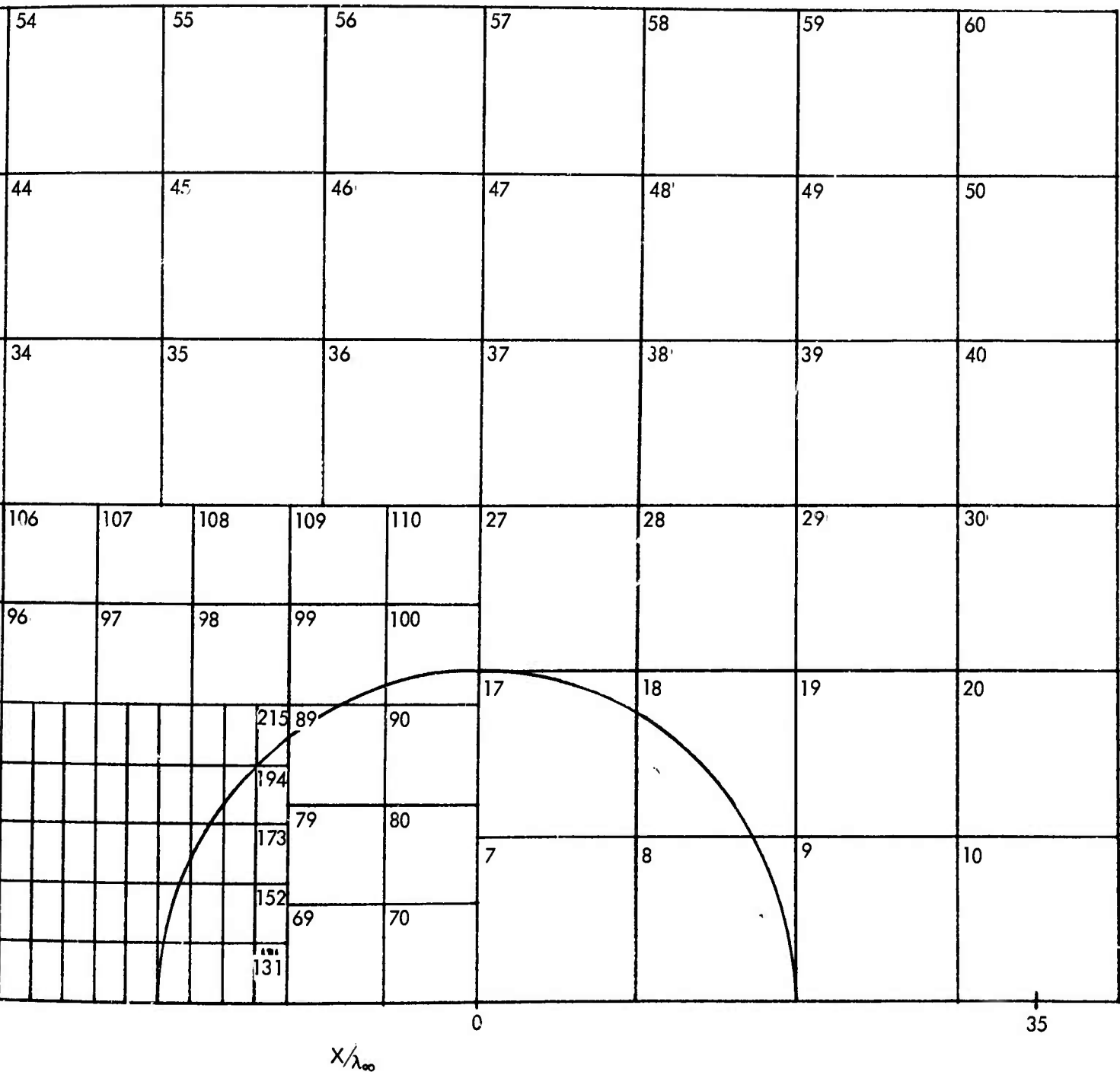


**Figure 16. Cell Arrangement**

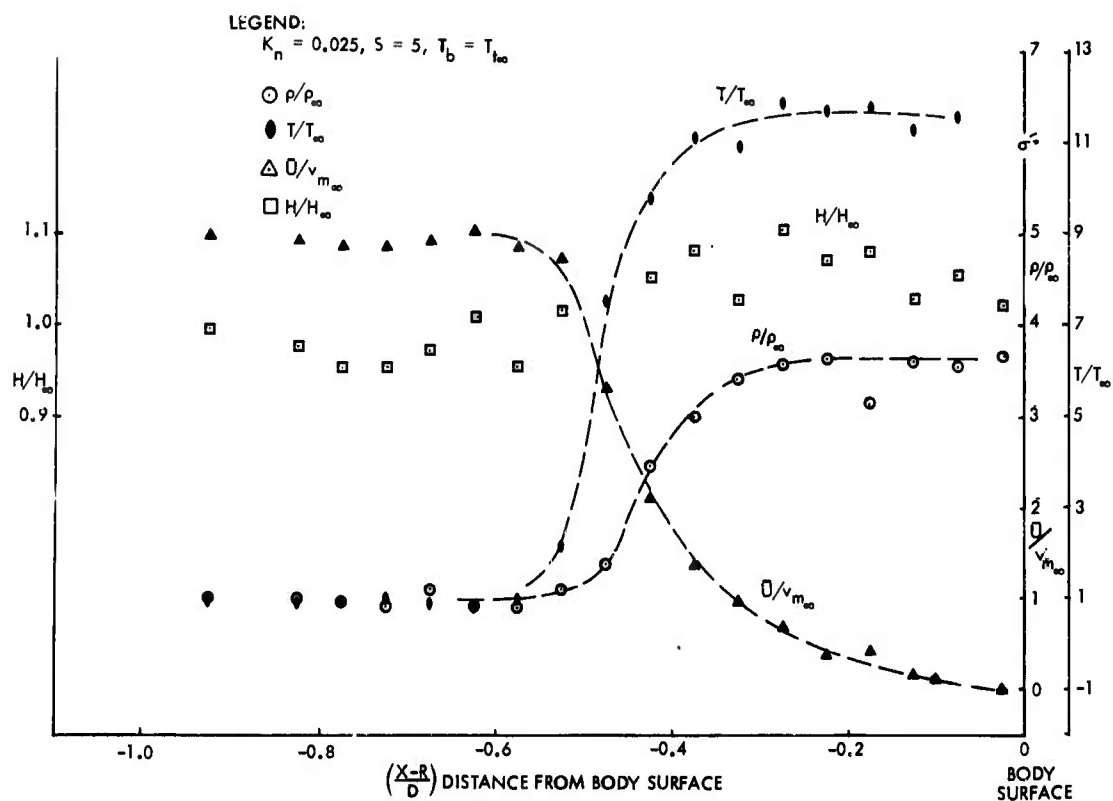


Figure 17. Cylinder Stagnation Line Profiles

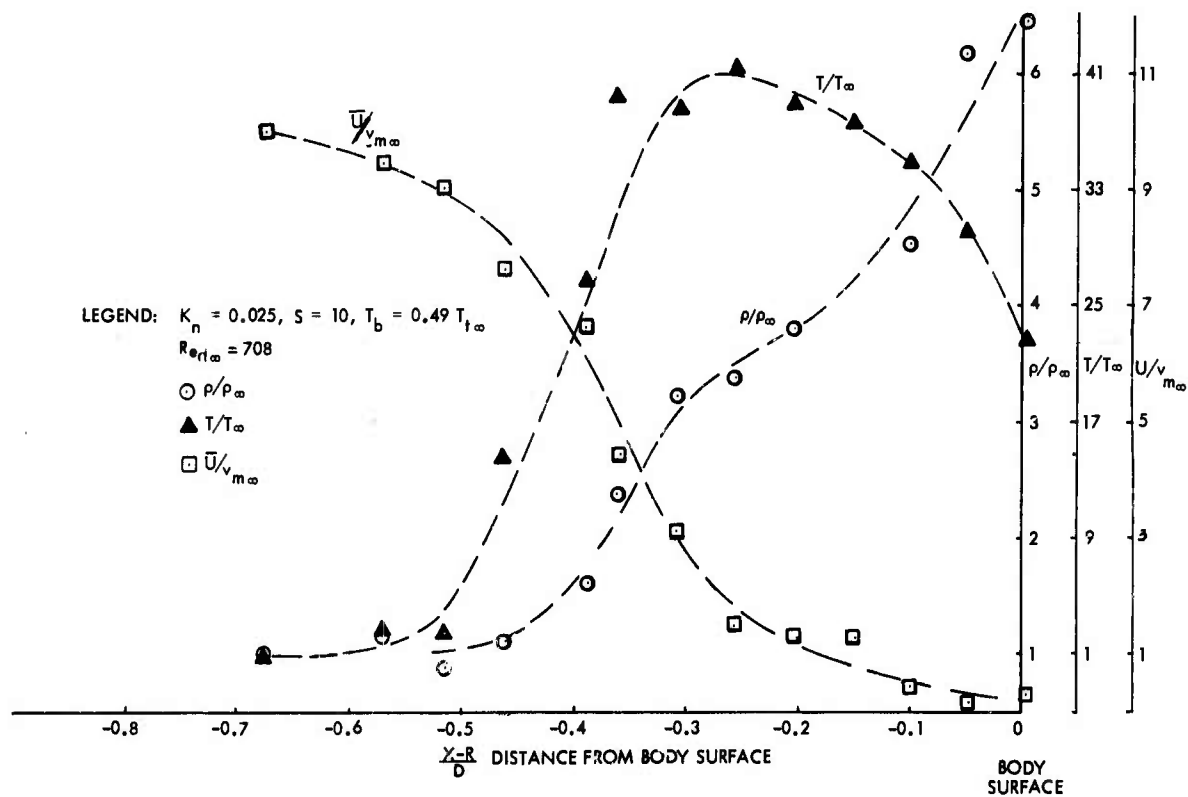


Figure 18. Cylinder Stagnation Line Profiles

## 2.4 LOW DENSITY WIND TUNNEL EXPERIMENTS

### 2.4.1 Sphere and Cone Drag Measurements

The purpose of these experiments, performed in the TRW Low Density Wind Tunnel, was to provide a small set of independent measurements of cone drag at Reynolds numbers of the order of a hundred. The sphere drag measurements serve, by comparison with the extensive existing literature, to indicate that the measurement system is accurate and that the sting drag can be properly accounted for. The wind tunnel is described in Appendix IV where the method of data reduction is also given. The comparison of the sphere drag measurements with the experimental and theoretical data is shown later in Figure 36. The agreement indicates that the present system is satisfactory.

The cone models had  $9^\circ$  half angles and were slightly blunted. The data is shown in Figure 19 where it is compared with that of Potter, Reference 19. The agreement at the lower Mach number, 4.3, is excellent but there is a small, systematic, and as yet unexplained, difference at Mach number 6.3.

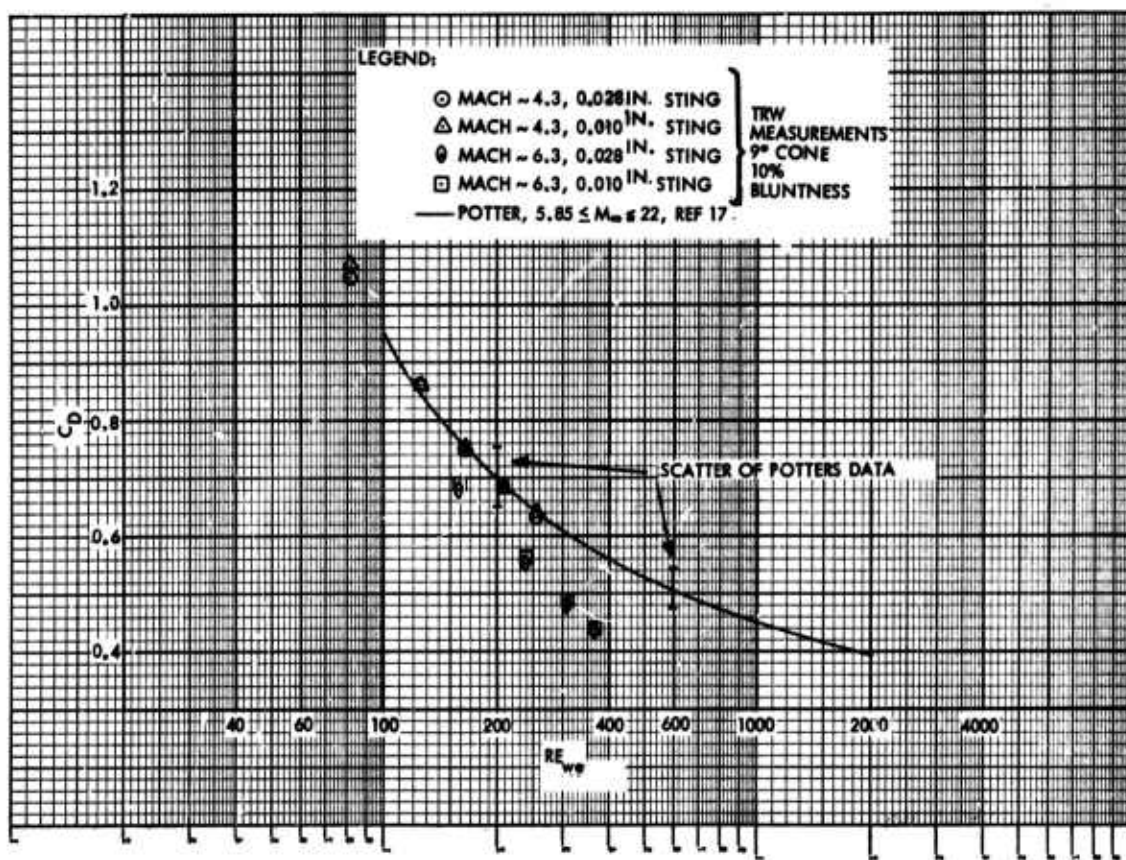


Figure 19. Drag Coefficients of Cones in Transition Flow

## 2.4.2 Two-Dimensional Flow Field Surveys

### 2.4.2.1 The Flow About Cylinders

In the experiments, also carried out in the Low Density Wind Tunnel, flow fields in the stagnation regions of cylinders in argon and nitrogen flow were surveyed with the free molecule equilibrium temperature probe. This probe, described in References 4 and 5, is a wire, the diameter of which is small compared to the mean free path, held traverse to the flow. The probe equilibrium temperature under these conditions is a useful property of the flow in that it changes significantly through a shock layer and may be measured quite accurately. The probe is described more fully in Appendix IV. The variation of probe temperature with Mach number in a uniform stream is shown in Figure 20.

To provide information about the character and extent of disturbances in front of cylinders at various Knudsen numbers, probe surveys were made in the stagnation regions of cylinders of several sizes. In Figures 21 through 24 lines of constant wire temperature are drawn to scale with the distance measured in free stream mean free paths. The

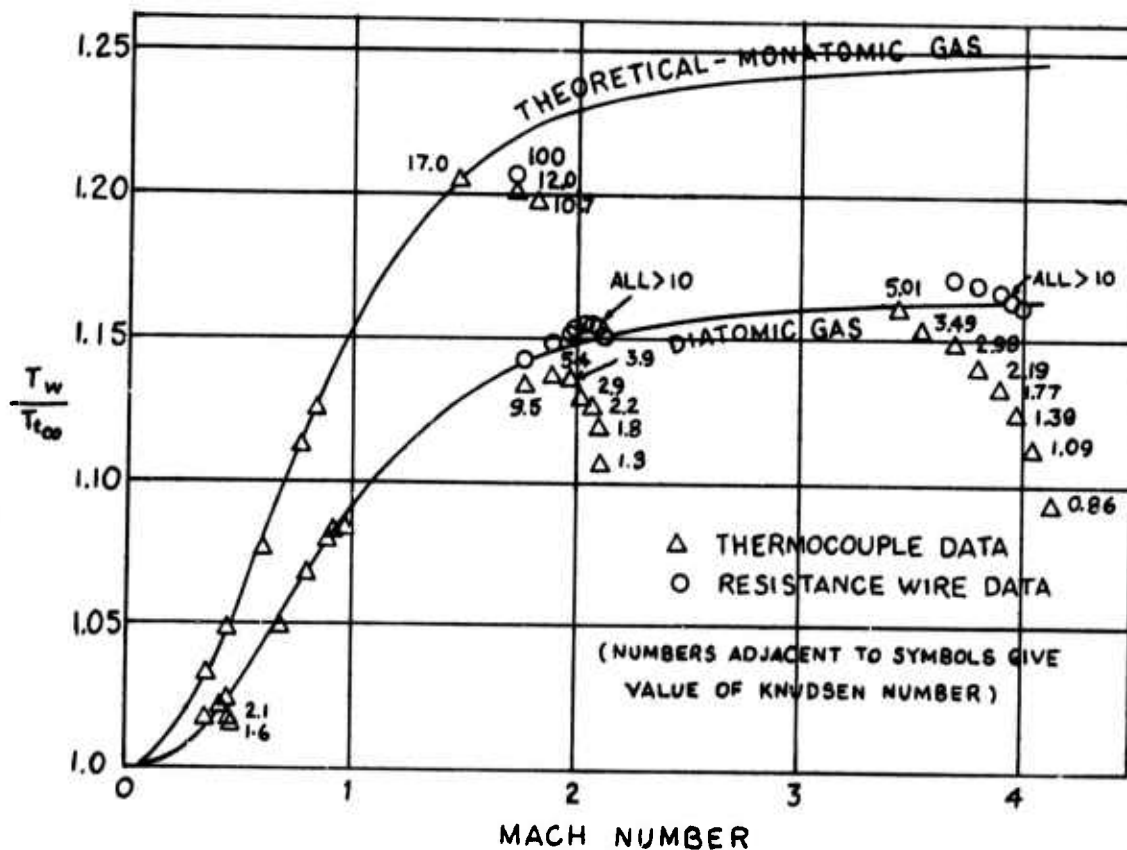


Figure 20. Variation of Free Molecule Equilibrium Temperature with Mach Number in a Uniform Flow (from Sherman, Ref 13)



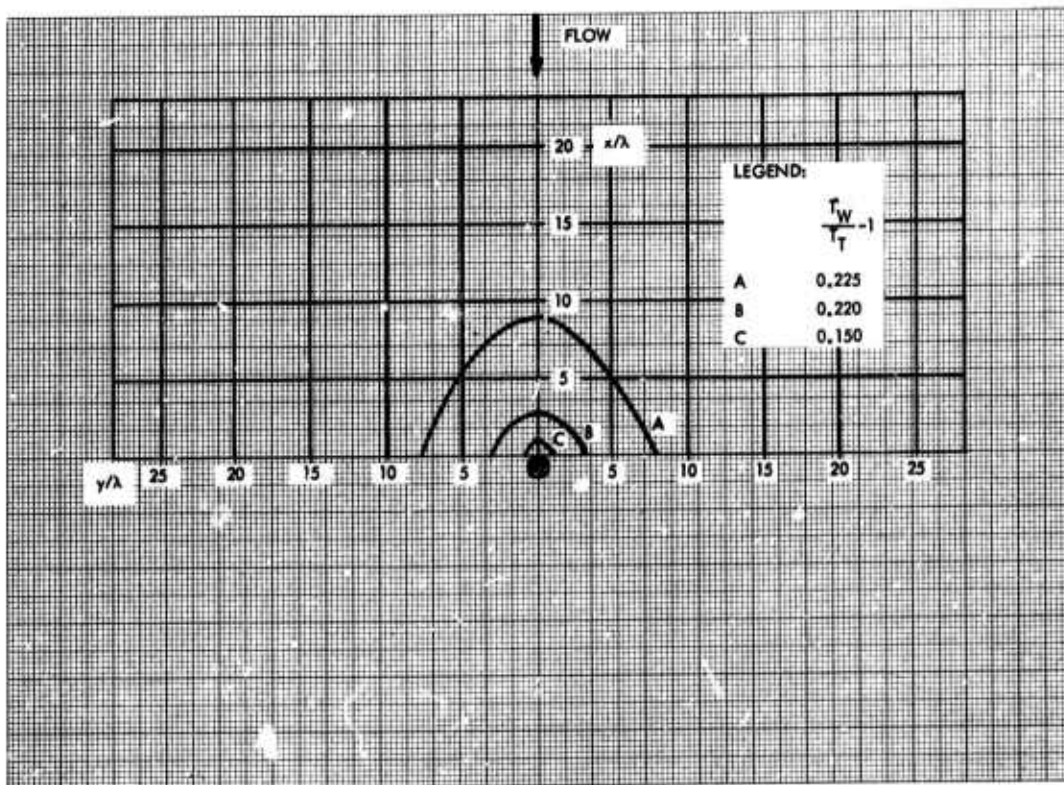


Figure 21. Lines of Constant Wire Temperature in the Stagnation Region of an Adiabatic Cylinder at  $M_\infty = 5.4$  and  $K_{n\infty} = 0.70$ , in Argon

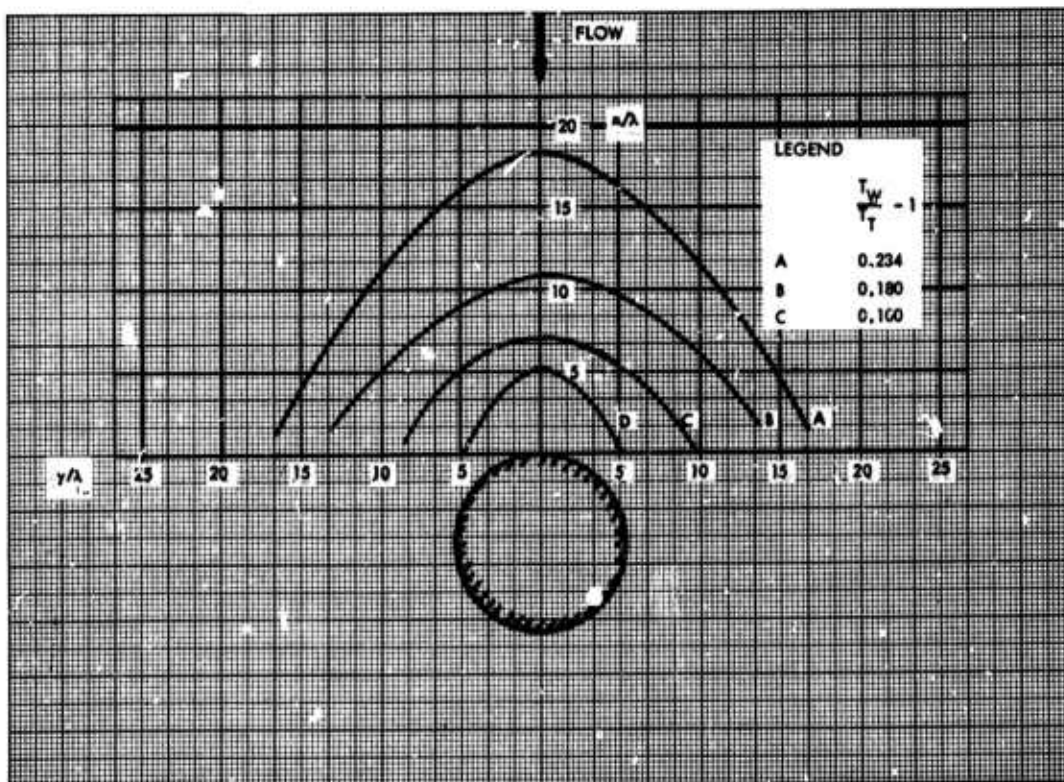


Figure 22. Lines of Constant Wire Temperature in the Stagnation Region of an Adiabatic Cylinder at  $M_\infty = 5.4$  and  $K_{n\infty} = 0.106$ , in Argon

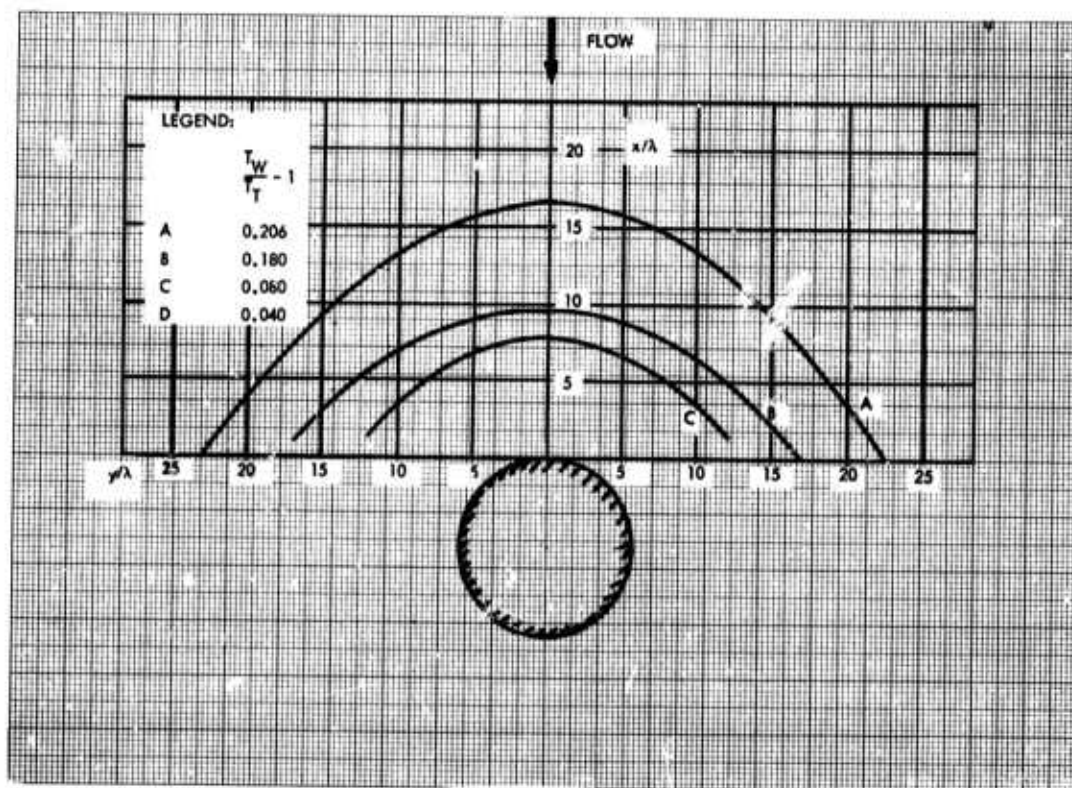


Figure 23. Lines of Constant Wire Temperature in the Stagnation Region of a Cylinder at  $M_\infty = 6.3$  and  $K_{n\infty} = 0.098$ , in Nitrogen

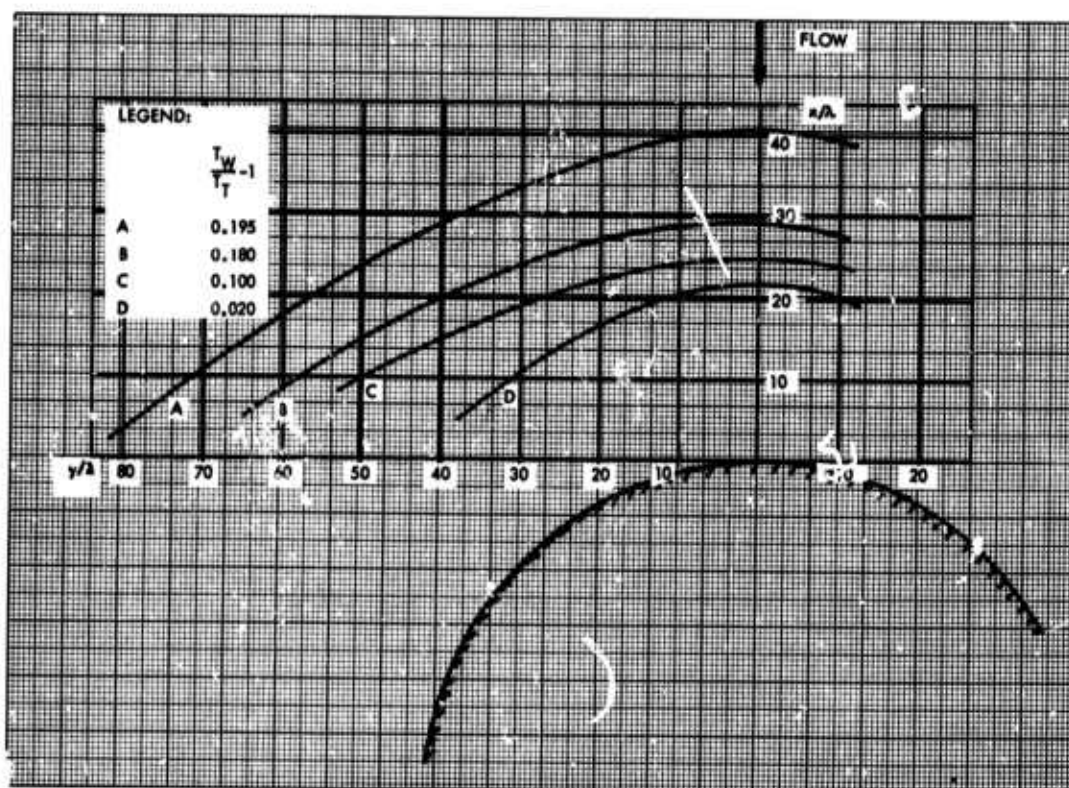


Figure 24. Lines of Constant Wire Temperature in the Stagnation Region of a Cylinder at  $M_\infty = 6.3$  and  $K_{n\infty} = 0.012$ , in Nitrogen

wire isotherm farthest away from the body (labelled A) is the beginning of the disturbance, i. e., the location of the first noticeable deviation from the free stream values. Because the change from the free stream is gradual, the location of A is the least accurate of the isotherms. In Figure 21 the body is comparable in diameter to the mean free path and the disturbance extends nine mean free paths in front of the body. Looking at the values of the temperature ratio isotherms, one can see that the shock is just beginning to develop.

In Figures 22 and 23, a body at approximately the same Knudsen number and Mach number is compared for argon and nitrogen. The extent of the disturbance on the stagnation line is greater for argon than for nitrogen while the lateral extent is less for argon. It should be mentioned that the argon flow is strongly supersaturated; so that while there was no indication of a condensation shock, it is not possible to be certain that condensation was completely absent.

Figure 24 shows the wire temperature contours about a body much larger than the mean free path; i. e., the flow here is closer to continuum flow. Here the extent of the disturbance and the low values reached by the wire temperature near the body shows that a shock wave has formed. It is interesting to see that the outer edge of the layer has moved away from the body, but that the shape of this disturbance has not changed much from the example in Figure 23. Hence, we start to have a shock wave at the conditions of Figure 23 and at the lower Knudsen number of Figure 24 we begin to see a fully developed shock wave and shock layer.

Figure 25 shows the variation of the stagnation line profiles for cylinders at various Knudsen numbers in argon. The profiles display the range of shock layer structure from a fully developed shock at  $K_{n_{\infty}} = 0.090$  to just the beginning of a disturbance at  $K_{n_{\infty}} = 0.70$ .

The theoretical value for the recovery temperature ratio of the probe in a uniform stream at high Mach number for a monatomic gas is  $T_w/T_T - 1 = 0.25$  (Figure 20). In general, the measured recovery temperature does not take on this value in the free stream. The error comes from heat conduction at the ends of the probe, which lie in the nozzle boundary layer. The  $K_{n_{\infty}} = 0.28$  data in Figure 25 were corrected for this

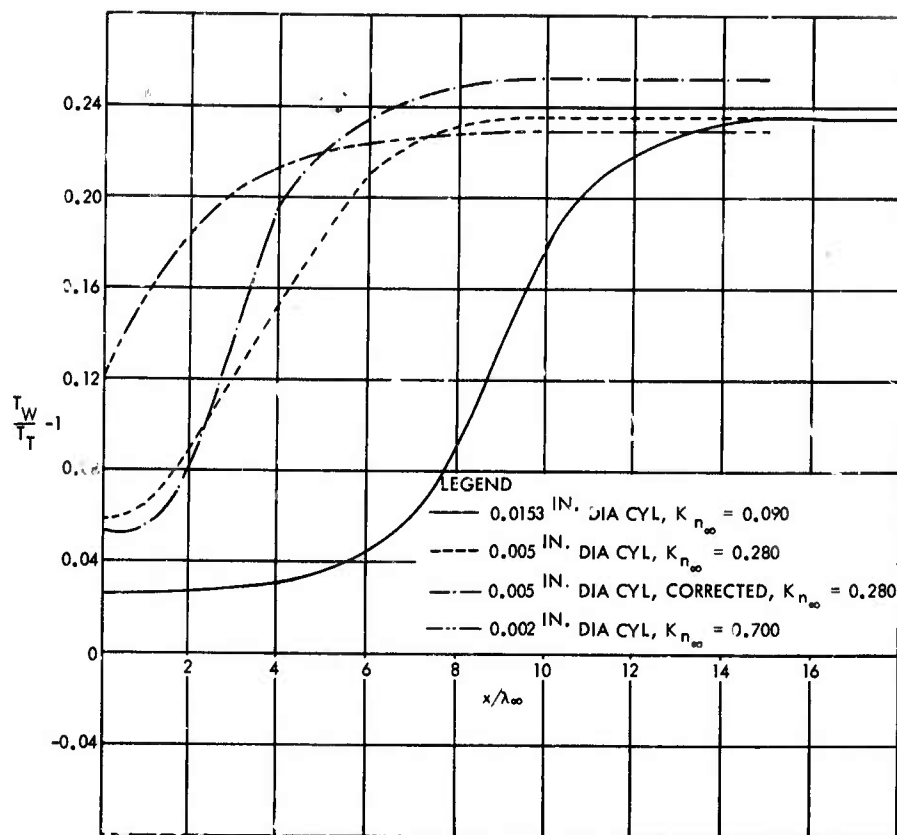


Figure 25. Stagnation Line Profiles on Cylinders at  $M_{\infty} = 5.4$  in Argon

effect and both corrected and uncorrected profiles are shown there. The correction makes use of the measured point temperatures at the thermocouple junctions of the probe and of the analytical solutions in NACA TN 2599 by Scadron and Warshawsky (Reference 13). These corrections require approximate values of temperature and velocity in the shock wave. These were obtained from the solutions of Liepmann, et al (Reference 18). The corrected curve at  $K_n = 0.28$  is also shown in Figure 33 elsewhere in the report where it is compared to a Monte Carlo calculation.

Shown in Figure 26 are stagnation line profiles at various Knudsen numbers in argon and nitrogen. In Figure 27 can be seen the development of a boundary layer between the shock and body, as discussed above, as the Knudsen number decreases from 0.098 to 0.0062.

#### 2.4.2.2 The Flow about Wedges

As in the case of the cylinder, the flow field in the stagnation region of various wedges was investigated.



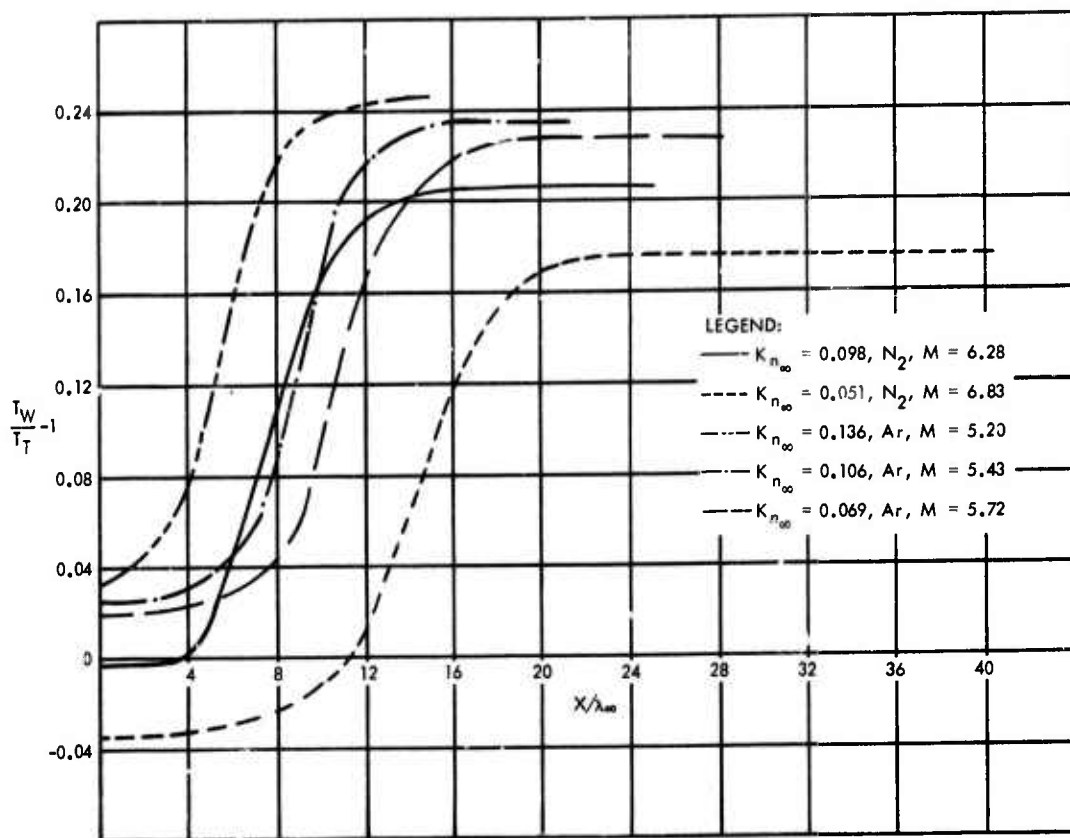


Figure 26. Stagnation Line Profiles on a 0.0153 in. Diameter Cylinder in Nitrogen and Argon

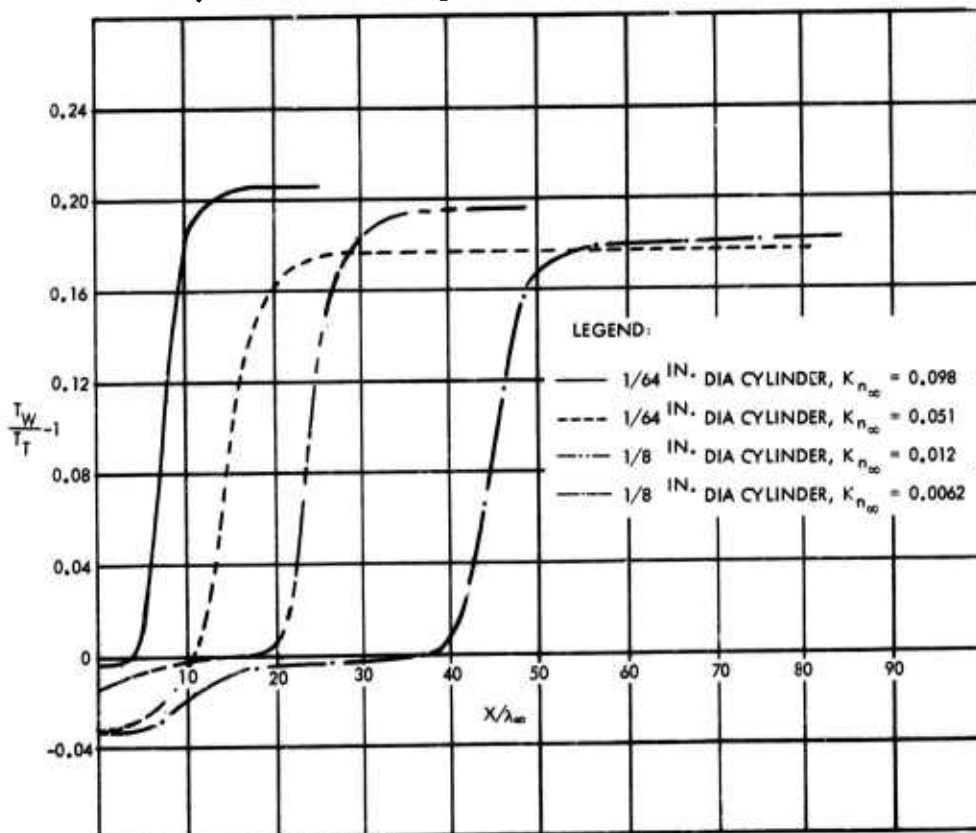


Figure 27. Stagnation Line Profiles on Cylinders at  $M_\infty = 6.3$  in Nitrogen

In Figure 28 is shown recovery temperature profiles in the flow field about a sharp (nose radius less than 0.0003 inch)  $20^\circ$  symmetrical wedge. It can be seen that a disturbance extends about 12 mean free paths in front of the wedge. As one might expect the strength of the disturbance is very slight. It can be seen in Figure 29 how the disturbance increases in strength as the mean free path becomes smaller.

In Figures 30 and 31 the flow field in front of a blunt  $18^\circ$  included angle wedge is presented for a warm and liquid-nitrogen cooled body. As one might expect, the beginnings of the disturbance moves in toward the body as it is cooled. A similar effect can be seen in the curves of Figure 32. Here we can see the entire shock structure pulled in toward the body for the cold cases, and the large drop in the temperature through the boundary layer.

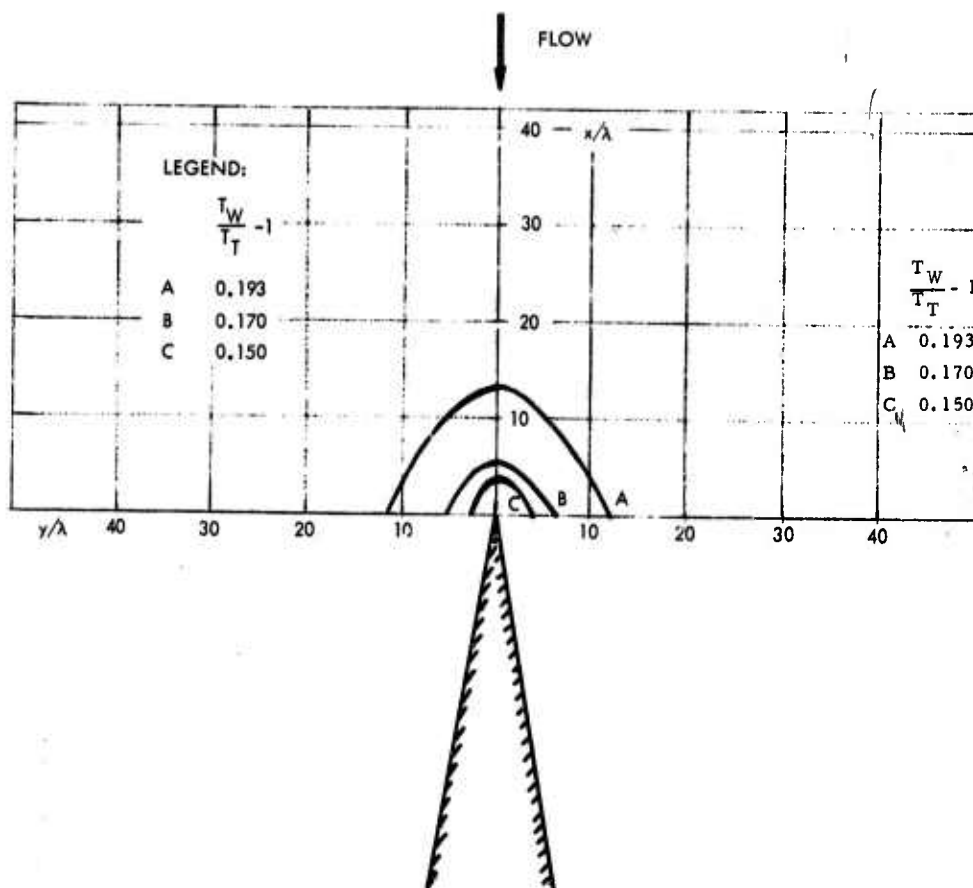


Figure 28. Lines of Constant Wire Temperature in the Stagnation Region of a Sharp  $20^\circ$  Wedge at  $M_\infty = 6.7$  in Nitrogen

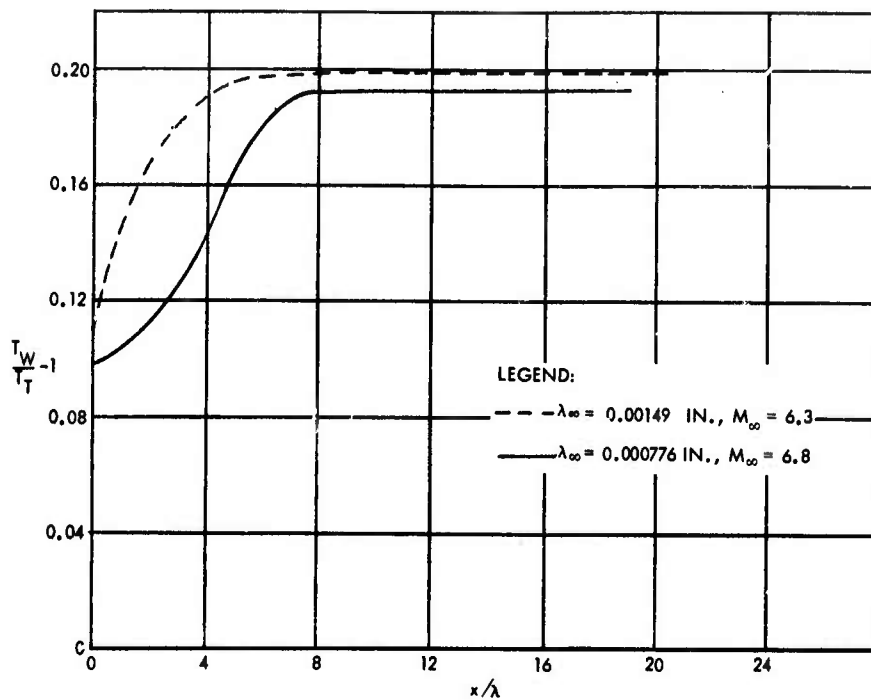


Figure 29. Stagnation Line Profiles on a Sharp 20° Wedge at  $M_\infty \sim 6.5$  in Nitrogen

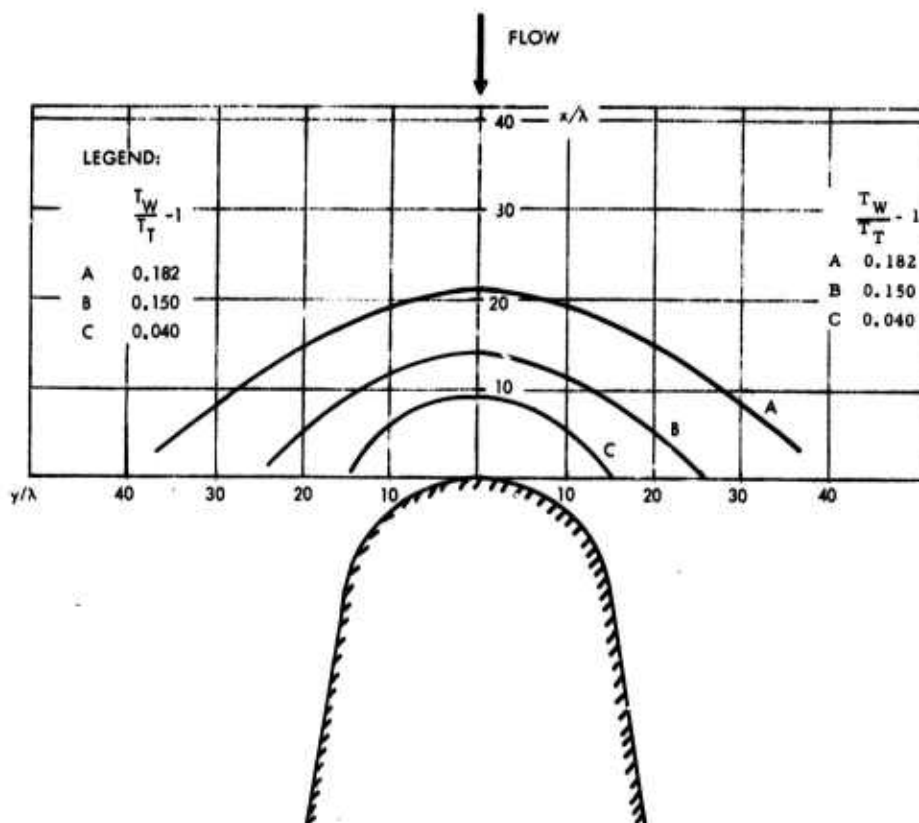


Figure 30. Lines of Constant Wire Temperature in the Stagnation Region of a Blunt 18° Wedge at  $M_\infty = 6.7$  in Nitrogen



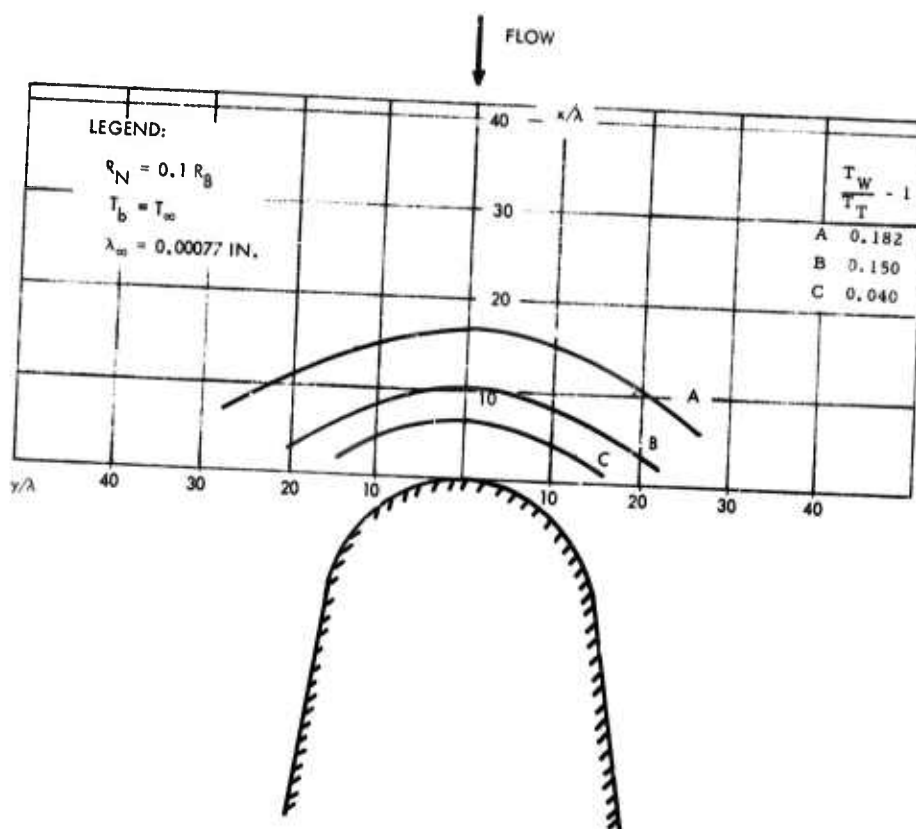


Figure 31. Lines of Constant Wire Temperature in the Stagnation Region of a Cold, Blunt  $18^\circ$  Wedge at  $M_\infty = 6.7$  in Nitrogen

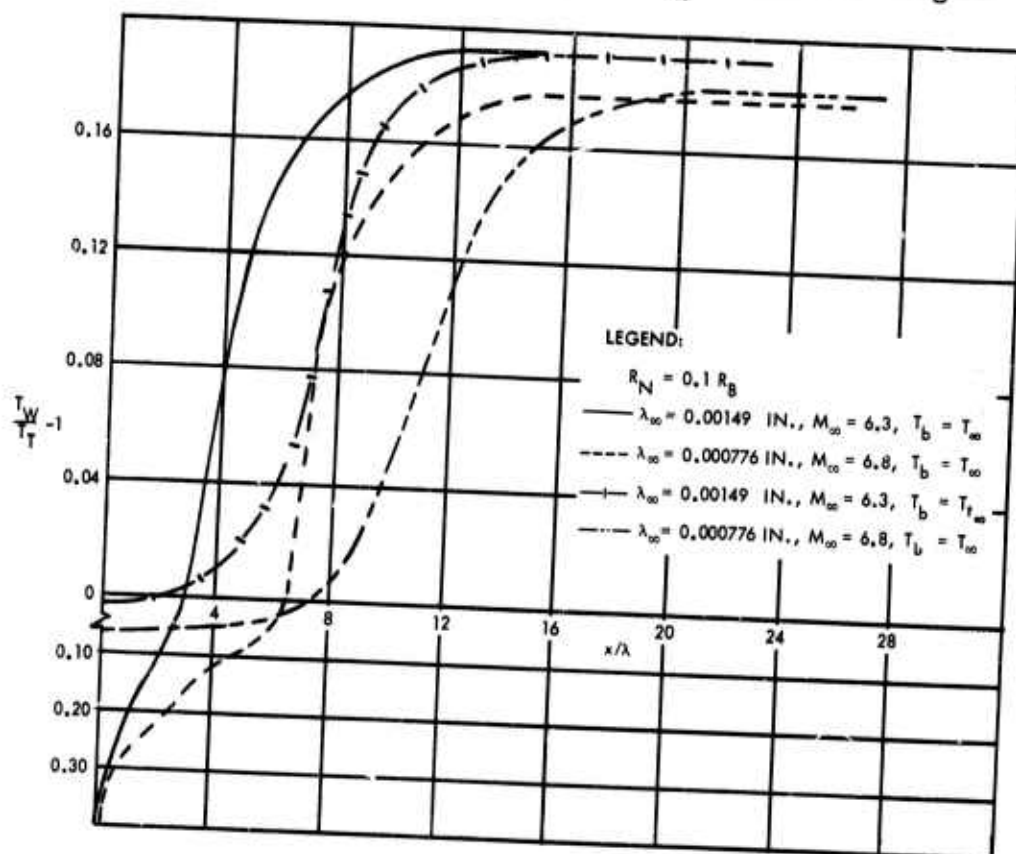


Figure 32. Stagnation Line Profiles on a Warm and Cold  $18^\circ$  Blunt Wedge at  $M_\infty \sim 6.5$  in Nitrogen

## 2.5 COMPARISONS OF MONTE CARLO THEORY WITH EXPERIMENT

### 2.5.1 Free Molecule Equilibrium Temperature Measurements and Calculations

The operation of the equilibrium temperature probe and the flow field survey performed with it in the TRW Low Density Wind Tunnel were discussed in the preceding section. Also mentioned previously was the fact that the Monte Carlo programs can compute the energy flux and molecular number flux impinging upon a circular region of arbitrary size and location in the flow field. Molecules do not collide with the circle; they pass through it in their normal movement in the field; hence, there is no disturbance to the flow. These circles simulate equilibrium temperature probes, and by assuming a reflection process, the recovery temperature which an actual probe at that location would reach can be computed.

Assuming complete accommodation and diffuse reflections and defining:

- $\dot{e}$  = energy flux impinging on the probe
- $\dot{n}$  = molecular number flux to the probe
- $T_w$  = probe recovery temperature
- $k$  = Boltzmann constant

An energy balance for a monatomic gas yields:

$$\dot{e} = 2 \dot{n} k T_w$$

(Since molecules effusing from the wire in Maxwellian equilibrium carry an average energy per molecule of  $2 k T_w$ .)

Then:

$$\frac{T_w}{T_{t_\infty}} = \frac{\dot{e}}{2 k \dot{n} T_{t_\infty}}$$

The Monte Carlo programs also compute the distribution function from which the probe recovery temperature can be computed. However, a large amount of numerical data handling would be required to do this, and the above procedure is far simpler. Note that since our "ideal" probes in the computer program do not disturb the flow they can be made larger than physical probes could be, the only requirement being that they be small compared to gradients in flow properties. Most of the calculations of probe temperature which will be discussed next were made with

probes of diameter  $d = 0.6\lambda_\infty$ . At the point in the shock layer where gradients were largest, check calculations were made with probes of diameter  $d = 0.3\lambda_\infty$  and  $0.2\lambda_\infty$ . There was negligible effect of "ideal" probe size on the recovery temperature.

In Figure 33 a comparison is shown of measured and calculated recovery temperature profile on the stagnation line of a cylinder at  $K_n = 0.30$ . The agreement is quite good in general, but the profiles differ near the free stream and near the body. In the calculation, the body was held at the free stream total temperature,  $T_{t_\infty}$ ; while the cylinder in the wind tunnel took on the recovery temperature, which at this Knudsen number is somewhat higher than  $T_{t_\infty}$ . This is the reason for the drop off in computed temperature near the body.

The free stream end of the computed profile does appear to be rather too rapid a beginning of the disturbance, resembling a Navier-Stokes profile, while the measured profile resembles H. W. Liepmann's Krook model calculations which are thought to be close to the truth. This matter is still being studied. The determination of the mean free path for argon in the density-temperature regime used for the measurements involved extrapolation of existing viscosity data, and there may be an error introduced here. More comparisons of this kind will be made in the near future.

#### 2.5.2 Density Measurements and Calculations on a Sphere

Some electron-beam density measurements on the stagnation line of a sphere at  $K_n = 0.03$ ,  $S = 3.5$  were kindly made available to us by Dr. David Russell of JPL. A comparison of these measurements with Monte Carlo results is shown in Figure 34. The calculation was made on the 7040 computer by Professor Bird in Sydney as a test case for some future work. This result is not as well converged as some of our other results, and there is some scatter. However, it is clear that there is very good agreement in the density profile except near the body where the calculated density is slightly lower. This is not unexpected since the density calculation represents a mean value for a small region of space slightly off the stagnation line. Away from the body, this is a good representation of the axis value since the velocity normal to the axis,  $v$  velocity, is negligible there. Near the body, the  $v$  velocity increases, however,

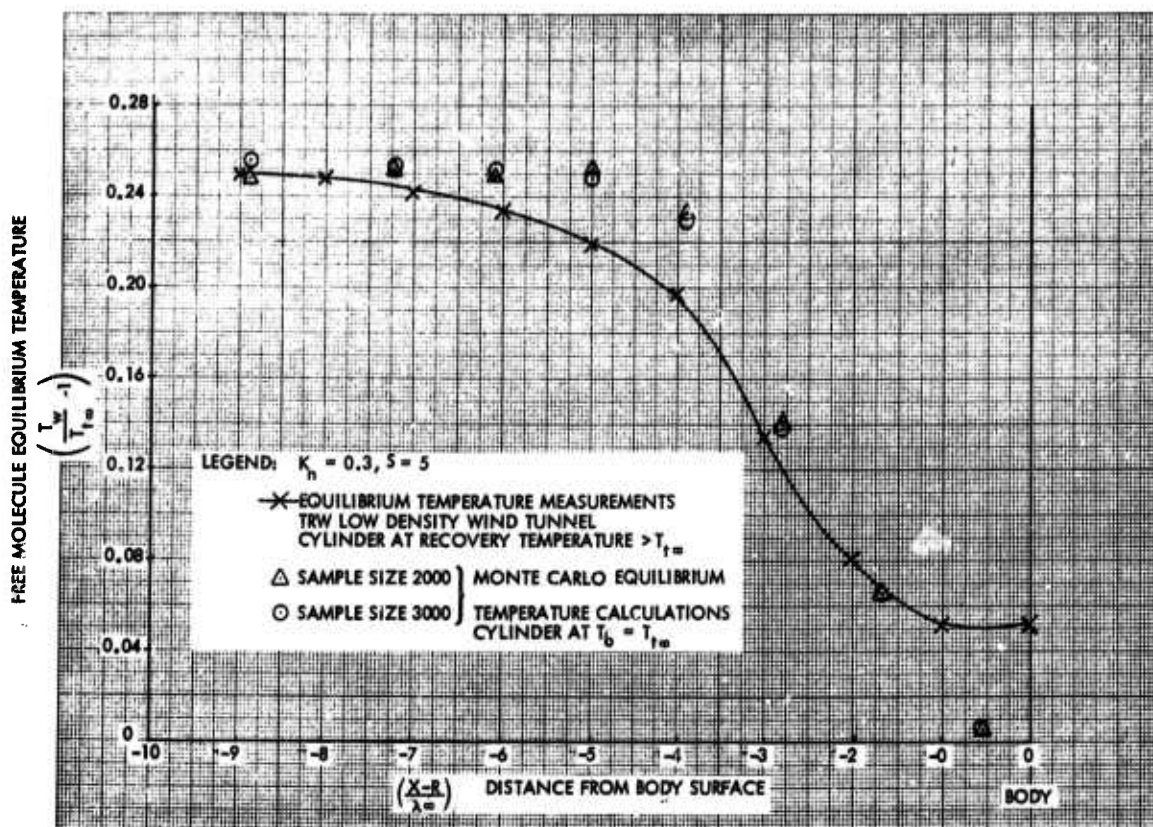


Figure 33. Comparison of Measured and Calculated Free Molecule Equilibrium Temperature Along Stagnation Line of a Cylinder

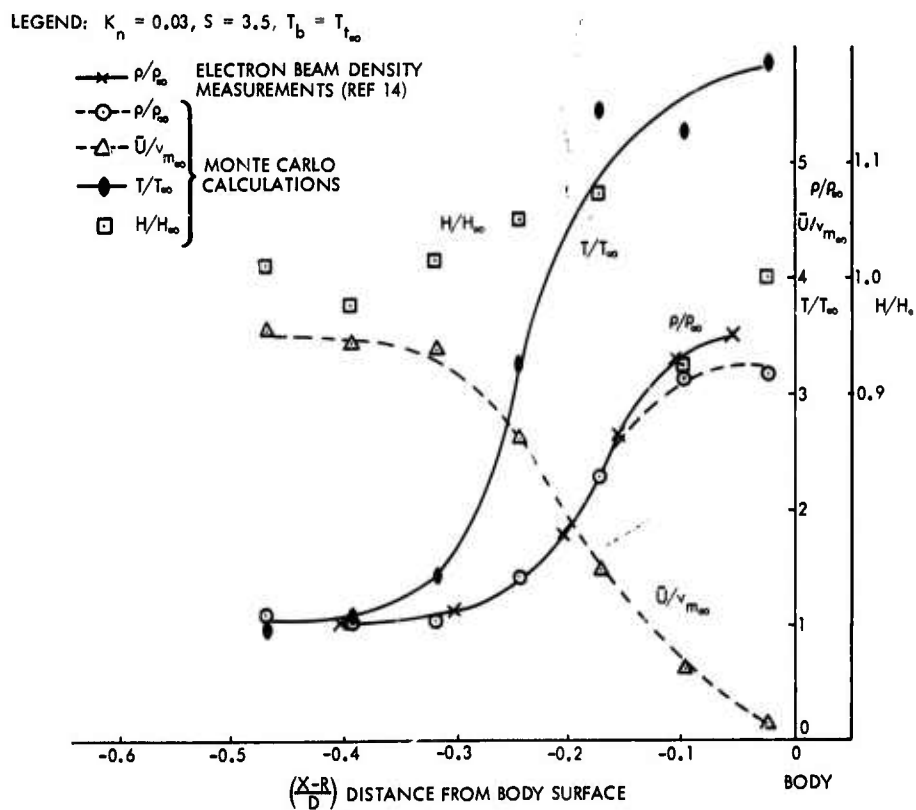


Figure 34. Comparison of Measured and Calculated Density Along Stagnation Line of a Sphere

and our spatial average density does not rise as much as the true stagnation line density. Reference to a picture of typical cell arrangement, say Figure 8, will make this clearer.

It is planned to do the calculation again with smaller cells in the stagnation region and a larger sample size.

### 2.5.3 Measured and Calculated Drag on Cylinders and Spheres

A comparison of Monte Carlo drag calculations on cylinders with a collection of measured drag data from the published literature is shown in Figure 35, covering the range from  $K_n = 0.025$  to 100, at  $S = 5$ . The measurements were made in air for body temperatures ranging from  $T_b/T_\infty = 8.0$  (free stream total temperature) to  $T_b/T_\infty = 9.15$ , which is close to free molecule recovery temperature for a diatomic gas. The calculations are for a body at  $T_b/T_\infty = 11$ , which is free stream total temperature for a monatomic gas at  $S = 5$ . This temperature difference should be negligible at the lower Knudsen numbers, but it does have a significant effect in the free molecule results. The calculated  $C_D$  shown at  $K_n = 100$ ,  $C_D = 2.99$ , is within 0.3% of the correct theoretical value for  $T_b/T_\infty = 11$ , which is 3.0. The diffuse free molecule limit shown is the correct theoretical value for  $T_b/T_\infty = 8.0$ . An asymptotic expression for  $C_D$  free molecule is

$$C_{Df. m.} \sim 2 + \frac{2}{S^2} + \frac{(\pi)^{3/2}}{4S} \sqrt{\frac{T_b}{T_\infty}}$$

for

$$S \geq 5$$

from which these results may be verified.

The maximum expected experimental error is shown in the figure. Estimates of the statistical uncertainty in the Monte Carlo results are shown in Table 2. They range from 0.5% to 2.3%.

A similar comparison for sphere drag at  $M = 4$  and 6 is shown in Figure 36, where  $Re_{D_\infty}$  is used as parameter. The TRW measurements of sphere drag obtained during this investigation are included in this comparison.

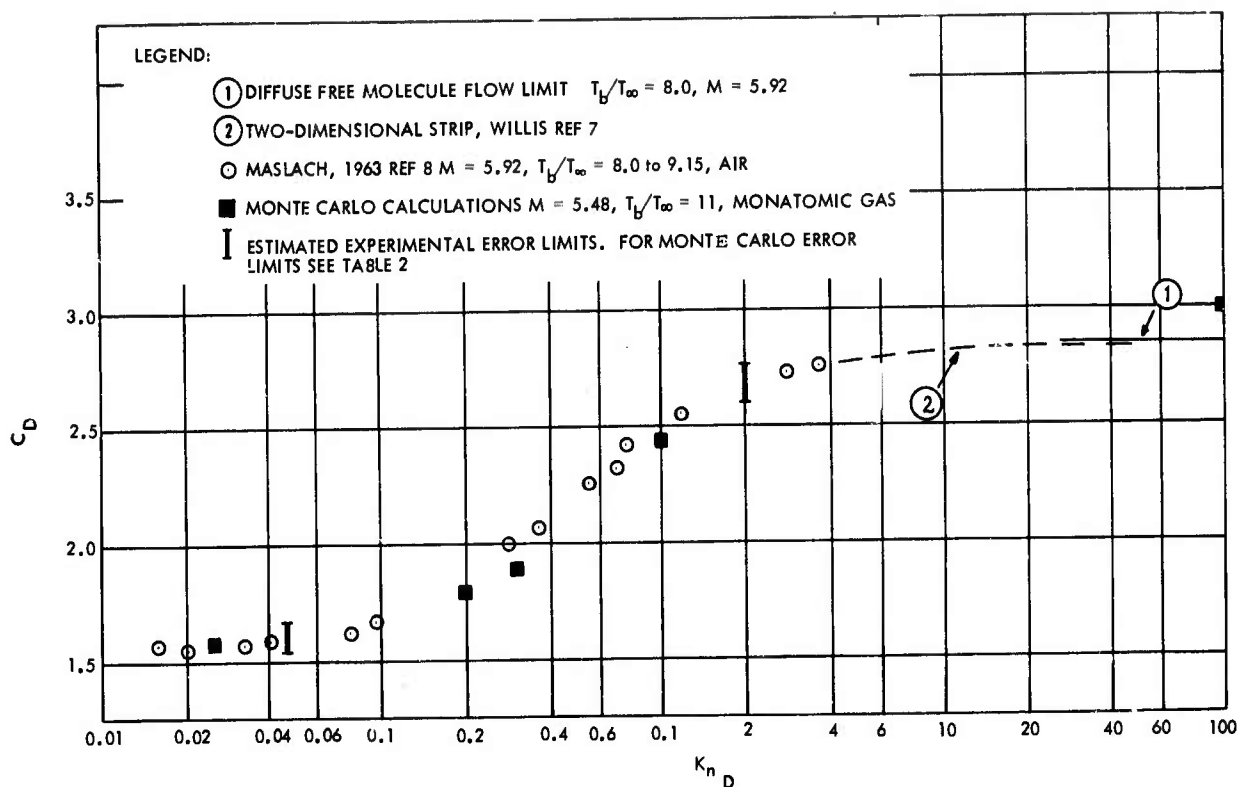


Figure 35. Comparison of Measured and Computed Cylinder Drag

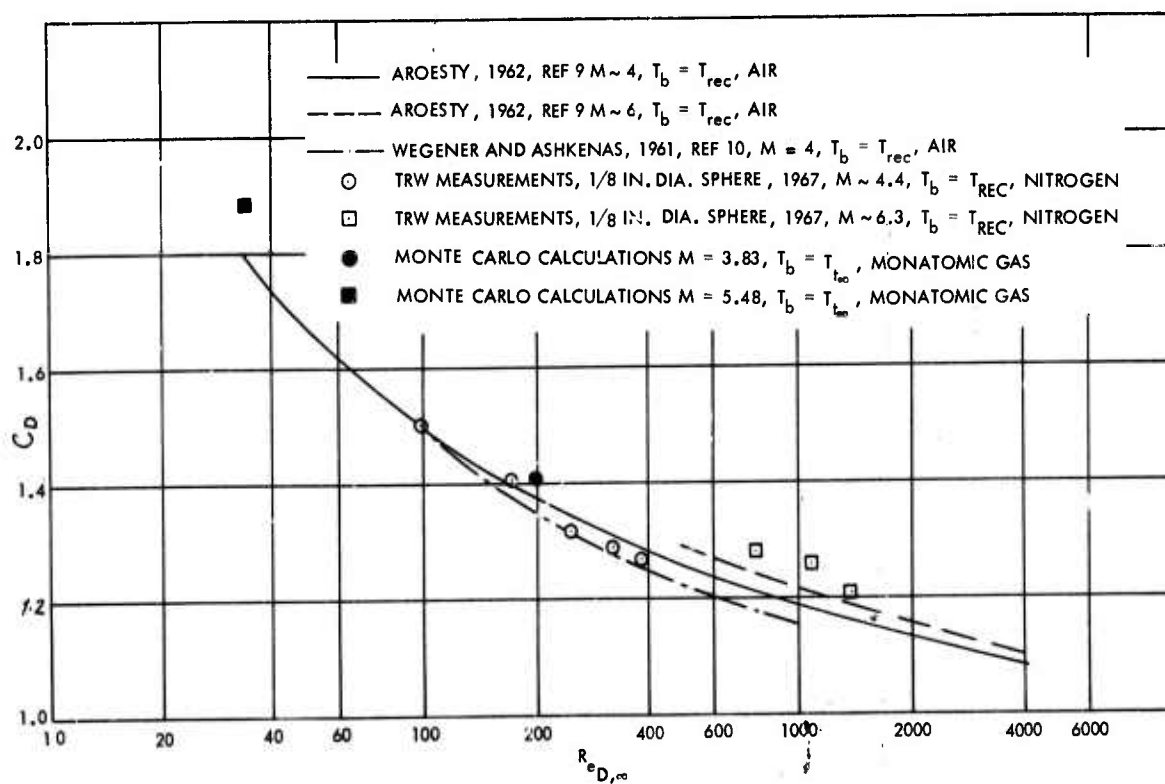


Figure 36. Comparison of Measured and Computed Sphere Drag



The agreement between measured and computed drag on these body shapes over the range of  $K_n$  and  $M$  considered is excellent.

More comparisons are planned at other Knudsen numbers, Mach numbers and body temperatures, and for other body shapes such as wedges and cones.

## 2.6 CONCLUSIONS

A Monte Carlo method for computing flow fields and body forces has been extensively developed. Monte Carlo calculations have been made for cylinders, spheres, sharp wedges, and sharp cones over the Knudsen number range 0.025 to 100.0 and Mach number range 3.8 to 11.0. These results are unique in that there are no other theoretical results for complete bodies over the entire transition regime.

Drag measurements on spheres and slightly blunted slender cones have been made in the TRW Low Density Wind Tunnel over the Knudsen number range 0.005 to 0.025 and Mach number range 4.0 to 6.0. The agreement with existing drag data in the literature is very good.

Flow field surveys with an equilibrium temperature probe have been carried out in the TRW Low Density Wind Tunnel on cylinders and wedges in the Knudsen number range 0.005 to 0.30 and Mach number range 4.0 to 6.0. These results provide information in a Knudsen number range not previously studied.

A number of comparisons of the Monte Carlo theoretical results with experimental results has been made; viz,

- 1) Measured and computed equilibrium temperature profiles on the stagnation line of a cylinder at  $K_n = 0.3$ .
- 2) Measured and computed density profiles on the stagnation line of a sphere at  $K_n = 0.03$ .
- 3) Drag measurements and calculations on cylinders and spheres over range  $K_n = 0.025$  to 100.

In all comparisons above, the agreement was quite close, strongly suggesting that the Monte Carlo theory can describe the transitional flow regime with considerable accuracy.

## 2.7 RECOMMENDATIONS FOR FUTURE WORK

While the degree of agreement to date between measurements and the predictions of the Monte Carlo method is very encouraging, there are many more comparisons which can be and should be made; e. g. ,

- 1) comparisons with the TRW equilibrium temperature surveys off the stagnation line and at other Knudsen numbers;
- 2) comparison with measurements of heat transfer to fine wires, a large collection of which exists in the literature;
- 3) it has been claimed that the distribution function of a gas can be measured by an electron beam technique. Such measurements, if available, could provide another direct check on the calculated distribution function.
- 4) extensive drag measurements exist in the literature, especially on spheres and cones. More direct comparisons should be made of measured and computed drag.

The Monte Carlo method presently uses the rigid elastic sphere collision model with a perfectly accommodating, diffusely reflecting surface model. Other collision and surface reflection models should be investigated.

Extension of the method to include internal degrees of freedom looks to be within the realm of possibility and this should be pursued.

The method can very easily be extended to include other body shapes; e. g. , wedges and cones of arbitrary bluntness and apex angle.

Comparison with experimental data for a very complicated flow which can be handled inexpensively on the computer should be made. An experimental program at California Institute of Technology to measure shock reflection from a wall is underway. This flow could be described inexpensively on the computer since it is one-dimensional, and it would be a very exacting test of the theory.

## SECTION III

### WAKE TURBULENCE MEASUREMENTS (HYPERSONIC WAKE AND BOUNDARY LAYER TECHNOLOGY)

#### 3.1 INTRODUCTION AND BACKGROUND

A knowledge of the fluid dynamical turbulent wake properties is needed to understand and predict radar scattering from reentry vehicle wakes. Among the turbulent wake properties, the three-dimensional correlation length plays a major role in the current theories of radar backscatter. Previous experiments in the TRW Systems ballistic range measured the wake turbulence behind .22 caliber projectiles traveling at 4000 feet per second. A single anemometer probe was placed close to the projectile path to sense the quickly growing wake behind the projectile; analysis of the fluctuating data providing correlation times. Radars, however, sense space correlation lengths. Therefore, it was an objective to obtain experimental data of wake turbulence fluctuations at more than one point simultaneously. It was an additional objective to relate the measured space correlation lengths to those in the turbulent wake behind a typical slender reentry vehicle. The accomplishments during the contract period are described in the following sections.

#### 3.2 SPACE CORRELATION LENGTH MEASUREMENTS

This program was begun with two hot-film anemometers placed adjacent to the projectile path in a newly established range. Two types of projectiles were launched from a .22 caliber rifle at 4000 fps, one type being more slender than the other.\* The fluctuating anemometer data was produced shortly behind the projectile by the growing wake which enveloped the anemometer. Later statistical analysis of the recorded data on a digital computer produced auto and cross correlations together with their Fourier transforms, power spectral densities and cross spectra. Eddy convection velocities, space correlation length scales, and time scales were also produced, the latter having been

\*The sphere-ogive-cylinder shapes of these commercial bullets is shown in Figure 4 of the report identified at the end of Section 3.2.

demonstrated earlier in a measurement program with a single anemometer (19). Space correlation length of the wake turbulence was shown for the first time in these measurements to increase with distance behind the projectile as predicted by the Lees-Hromas-Webb (20, 21) theory. Previous measurements of the wake core turbulence (22, 23) had shown a constant space correlation length up to 9000 diameters behind projectiles. These latter measurements had been made using optical methods (Schlieren and interferometer) which integrate along the light beam passing completely through the wake. In contrast, the anemometer makes a local measurement, its length (.20-inch) being much smaller than the wake.

These measurements were presented at the AIAA Fifth Aerospace Sciences Meeting, New York, January, 1967 as AIAA Paper No. 67-19. They are also available as TRW Report No. 07854-6021-R000, BSD-TR-67-82. This report has been scheduled for publication in the February, 1968, issue of the AIAA Journal.

### 3.3 EXTENDED X/D DATA

The next series of measurements utilized the more blunt .22 caliber projectile<sup>\*</sup> and two different spacings between the anemometers. A two-data estimate was thus obtained for the space correlation function and its integral, the space correlation length. Three different anemometer temperatures, 62°C, 166°C and 270°C, were used to provide data for reduction to velocity, density, and temperature fluctuations. In all, data from 35 shots were reduced. The statistical analyses were made over a much greater range of X/D than that used previously. As shown in Figure 37, the data from X/D = 100 to 160,000 was used in the analyses. The delay times in the auto and cross correlations of Figure 37, as well as the frequencies in power spectral densities of Figure 38, extend over four orders of magnitude. The definitions of autocorrelation and cross correlation coefficients used in Figure 37 were retained from the previously mentioned report, namely,

$$C_g(\Delta t) = \frac{\sum g(t) g(t + \Delta t)}{\sum g(t) g(t)}$$

\*Bluntness ratio of 0.6.

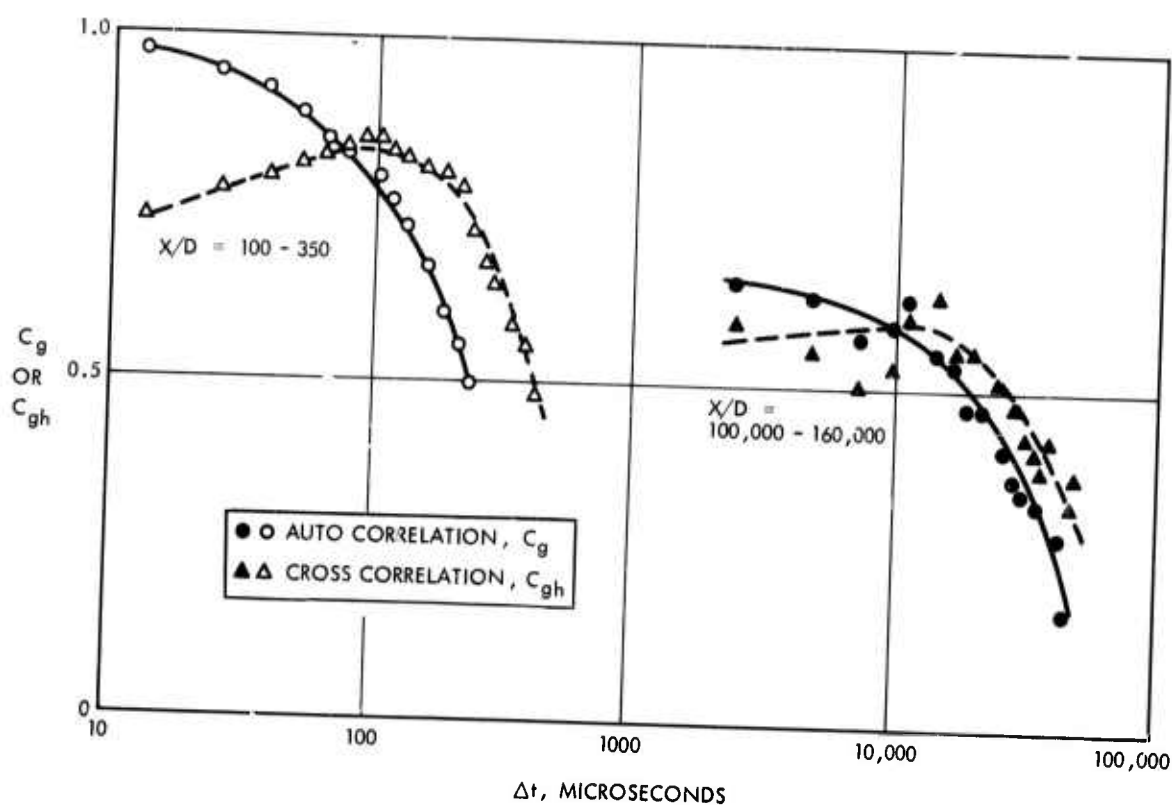


Figure 37. Typical Autocorrelation and Cross Correlation for Small and Large  $X/D$

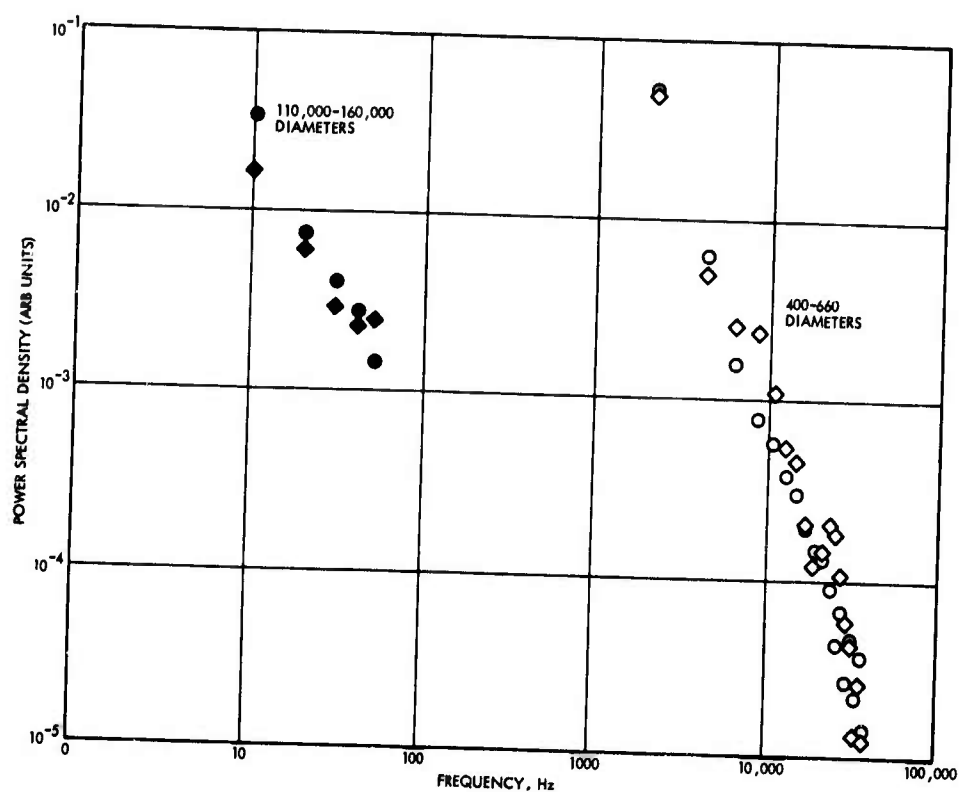


Figure 38. Typical Power Spectral Densities for Small and Large  $X/D$

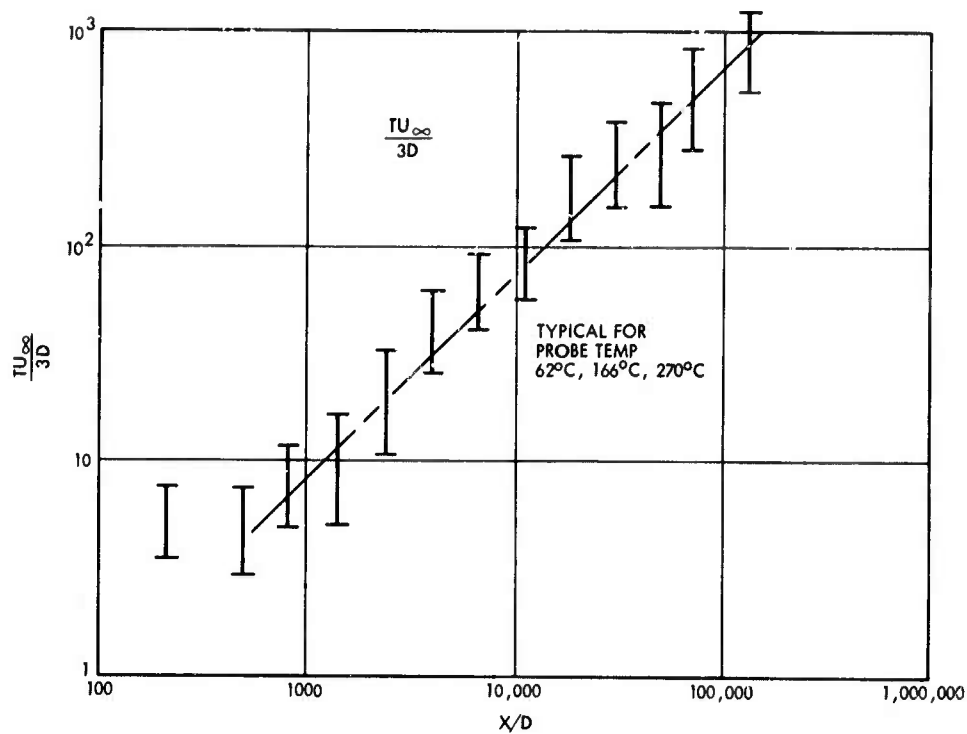


Figure 39. Time Correlation Scale for Extended  $X/D$

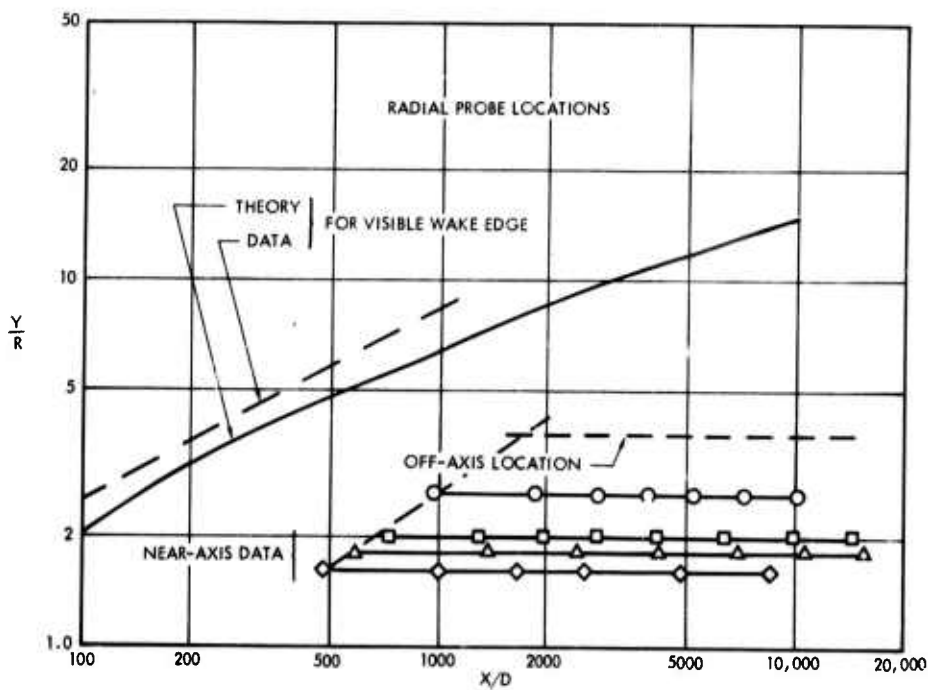


Figure 40. Radial Probe Locations Compared with Wake Width



and

$$C_{gh}(\Delta x, \Delta t) = \frac{\sum g(0, t) h(\Delta x, t + \Delta t)}{\left[ \sum g(t) g(t) \right]^{1/2} \left[ \sum h(\Delta x, t) h(\Delta x, t) \right]^{1/2}}$$

where  $g(t)$  and  $h(\Delta x, t)$  are the digitized data from the two anemometers, the respective mean values having been previously subtracted away. The time integral scale,  $T$ , which is shown in Figure 39 factored by the projectile velocity,  $U_\infty$  produced an acceptable trend over the length of the wake. The statistical techniques used to obtain these quantities are described in the previously mentioned reports.

### 3.4 OFF-AXIS DATA

Five of the previously mentioned 35 shots that were reduced utilized a near-axis location on one anemometer and an off-axis location on the other. This configuration was tested in response to a SAMSO/Aerospace request for an off-axis survey. The planning for the off-axis shots is shown in Figure 40 where the wake edge and anemometer probe locations are shown in units of projectile radii  $R$ . At  $Y/R = 1$ , the probe and projectile make contact. The off-axis probe was one projectile diameter farther away from the projectile axis than the near-axis probe.

The reduced data that was obtained was autocorrelation, power spectra, and time integral scales; probe separation being too great for space correlation data. The off-axis time-correlation data followed the same trends as the near-axis data, which is shown in Figures 37, 38, 39. No additional off-axis tests were conducted during the contract period.

The "theory" wake edge shown in Figure 40 was provided by a new calculation using the Lees-Hromas-Webb theory together with a  $C_D = 0.4$ , which is more accurate for this projectile than the previously used  $C_D = 0.7$ . (This revision is reflected in all of the theoretical results shown in this section.) In the theory, the wake width is really an energy diffusion width, whereas the experimental wake width is the average across the scalloped wake projection on a shadowgraph. In view of these limitations of the comparison, the agreement in Figure 40 between the Lees-Hromas-Webb theory prediction and the measured

wake edge is considered satisfactory.

### 3.5 TWO-DATA SPACE CORRELATION LENGTH SCALE

Anemometer probe separations  $\Delta x$  of  $R/2$  and  $R$  were used in acquiring data. Cross correlation output produced the statistical data needed to estimate the space correlation function, the integral of which is the space correlation length (distance over which fluctuations are correlated). The cross correlation data were first averaged over 10 to 15 shots with all probe temperatures being utilized. The averaged cross correlations were then smoothed in  $X/D$  with a weighted average scheme; 50 percent of the point in question was averaged with 25 percent of each of two adjacent data points. A curve was fit to the two data for  $\Delta x = R/2$  and  $R$  at each  $X/D$ . This curve extended from unity at a zero separation ( $\Delta x = 0$ ) to zero at a large separation ( $\Delta x = \infty$ ). The integral of that curve, namely, the space correlation length  $\Lambda$ , is shown in Figure 41. It agrees with the prediction of the Lees-Hromas-Webb theory, thus verifying one of the major features of the theory that affect the radar backscatter cross section.

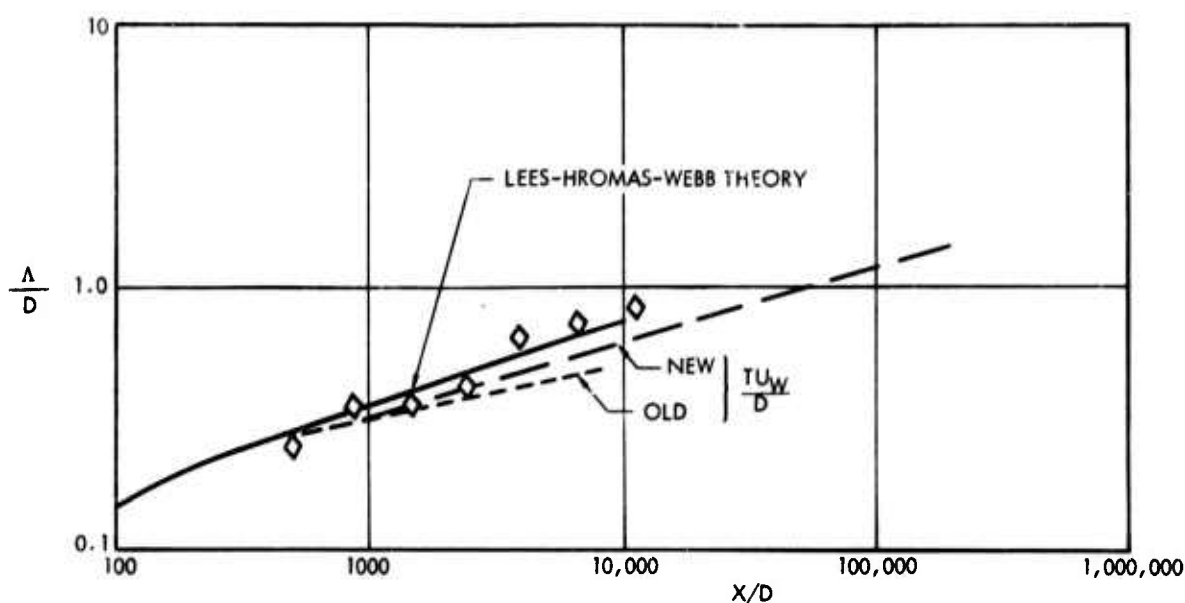


Figure 41. Space Correlation Length

Separate studies of  $\Lambda$  measurements, considering the low anemometer temperature data and high anemometer temperature data separately, gave no trend of  $\Lambda$  with probe temperature. The random irregularities of the  $\Lambda$  data were greater in this case because a smaller number of shots contributed to the averaging. Thus any conclusions about the lack of trend in the data must be qualified by the averaging irregularities. It will be explained in a later section that the data taken at low anemometer temperature are mostly wake temperature data and those at high anemometer temperature are mostly wake velocity data. Thus the lack of trend of  $\Lambda$  with anemometer temperature indicates that a single  $\Lambda$  characterizes both temperature and velocity fluctuations, within the precision of the measurements.

By Taylor's hypothesis, the product of the time integral scale  $T$  and the mean wake velocity, as predicted by the Lees-Hromas-Webb theory is comparable to  $\Lambda$ . This comparison is indeed shown to be good for both the old data, which was obtained during the first program described in 3.2, and the new extended-range data. The lesser  $X/D$  range obtained for  $\Lambda/D$  compared with  $TU_w/D$  suggests that extraneous effects in the ballistic range alter space correlations more quickly than they alter time correlations.

### 3.6 MEAN VELOCITY, TEMPERATURE AND DENSITY

The original reduction of mean wake velocity and temperature was taken from oscilloscope photographs, this reduction being later confirmed by digital computer output. The data were smoothed and averaged between three to five shots. Data for two different probe temperatures were thus obtained from projectile wakes and compared with calibrated responses obtained with the probes in a heated jet and in an oven. The data obtained with low probe temperature was mostly temperature, whereas the high probe temperature data was mostly velocity.

Mean wake velocity and temperature obtained by this technique is shown in Figures 42 and 43. The density can be obtained directly from the temperature data because the pressure is constant in the far wake, and perfect gas laws are valid. Both the velocity and temperature are somewhat lower than the Lees-Hromas-Webb theory prediction.

As shown in Figure 40, the near-axis data are located a significant fraction of the wake radius away from the wake axis when  $X/D$  is small. In order to make a better comparison with the axis values that are predicted by the Lees-Hromas-Webb theory, an equivalent to the measured data was constructed using a profile curve fitted to the wake width which passed through the near-axis data. The axis values of the fitted curves are shown in Figures 42 and 43 as the axis equivalents of the measured data. The axis velocity gives good agreement with the Lees-Hromas-Webb prediction up to the limit of calibration at  $X/D = 2,000$ . This agreement verifies another major feature of the Lees-Hromas-Webb theory which is directly related to the radar Doppler return. Somewhat less agreement is obtained by the axis temperature in Figure 43, although the correct trend is obtained.

Greater  $X/D$  range was obtained with mean convection velocities  $U_c$ , that is, the velocity of convection of fluctuations from one anemometer to the other, as determined by best cross correlation delay time. The average of at least 9 and as many as 25 shots are shown in Figure 44. It is reasonable that the convection velocity  $U_c$  falls below the previously determined mean wake velocity, shown in Figure 42, because the average over many more shots was used for the convection velocity. The probe-to-axis distance was greater for most shots than those few used to obtain the mean wake velocity measurement, resulting in a higher mean wake velocity than convection velocity up to the limit of calibration. It is, indeed, reassuring that a trend parallel to the predicted velocity was obtained for convection velocity up to an extended  $X/D$  of 70,000.

### 3.7 FLUCTUATION MEASUREMENTS OF VELOCITY, TEMPERATURE AND DENSITY

Among the 35 shots, data was taken with three different probe temperatures so that the fluctuations of velocity, temperature and density could be obtained. The calibration function  $q/T = A + B\sqrt{U}$  was utilized with mean and fluctuating components being substituted and then mean squared. The resulting expression contained  $\overline{q'^2}$  and the mean properties as known factors, and  $\overline{U'^2}$ ,  $\overline{U'T'}$ , and  $\overline{T'^2}$  as unknowns. The three sets of data formulated three linear equations that were inverted to obtain the three unknowns. A qualified success was obtained

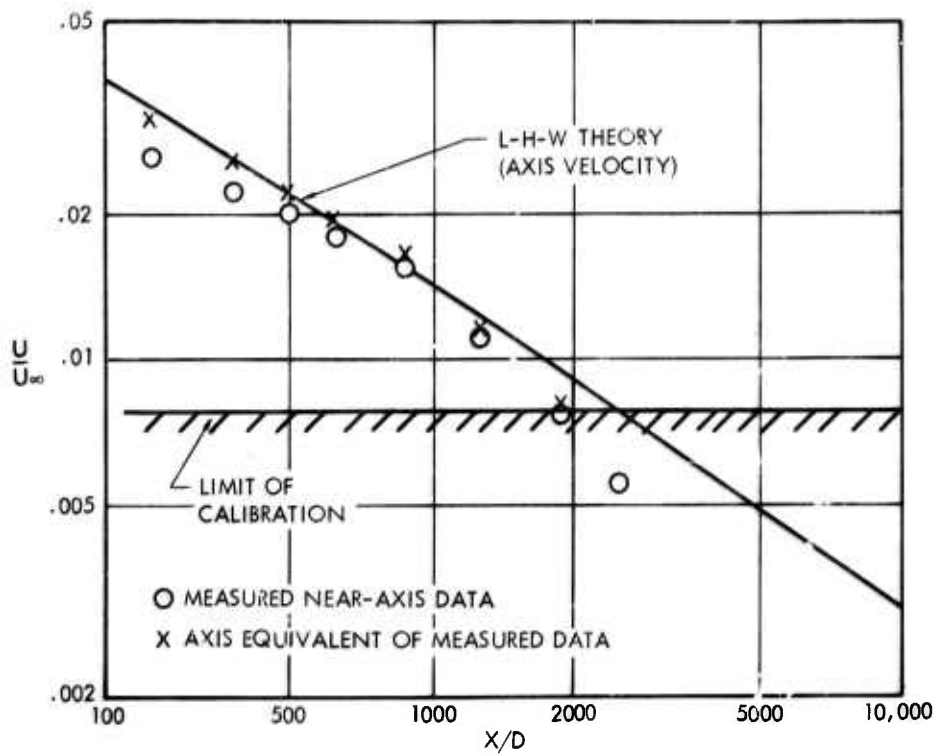


Figure 42. Mean Wake Velocity

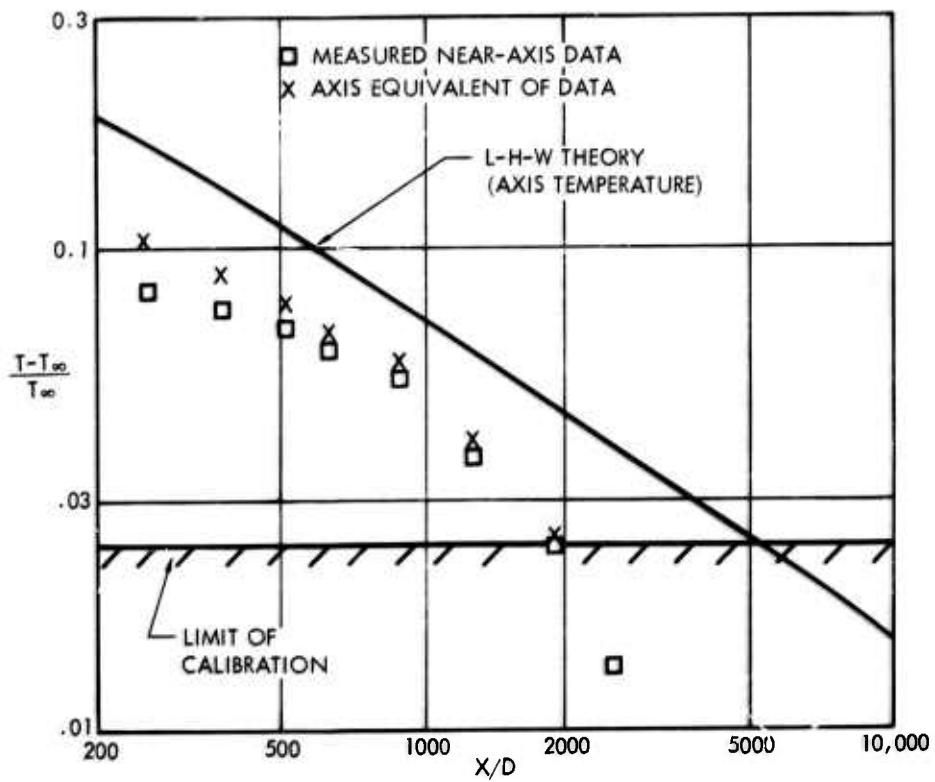


Figure 43. Mean Wake Temperature

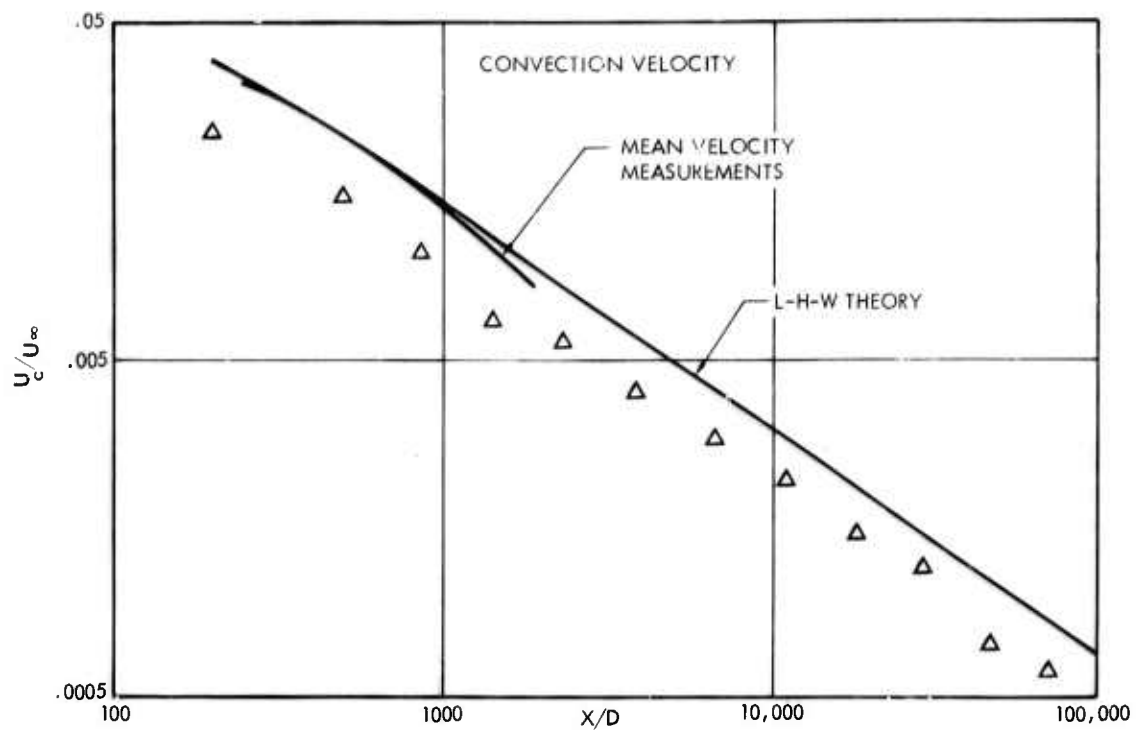


Figure 44. Convection Velocity Compared with Mean Wake Velocity

at  $X/D = 840$  where the following values were obtained

$$\frac{\overline{U'^2}}{\overline{U_w}}^{1/2} = 0.46$$

$$\frac{\overline{T'^2}}{(\overline{T_w} - \overline{T_\infty})}^{1/2} = 0.39$$

$$\frac{\overline{\rho'^2}}{(\overline{\rho_\infty} - \overline{\rho_w})}^{1/2} = 0.37$$

where the density fluctuations were obtained from the temperature fluctuations in much the same manner as that used for the mean values.

These values are in remarkable agreement with Townsend's (24) cylinder results and the recent axi-symmetric measurements of Demetriades (25) and Gibson (26). The necessary reduction of the cross product produced

$$\frac{\overline{U'T'}}{\overline{U'^2}^{1/2} \overline{T'^2}^{1/2}} = -1.16$$

which has the correct sign and is only slightly too large. At greater X/D the agreement in magnitude was poorer, although the correct signs were maintained. These results definitely prove the feasibility of the measurement technique and serve to indicate the needed refinements. These refinements include a wider range of probe operating temperatures, up to 300°C, and calibrations to lower velocities, down to 15 fps.

The underlying philosophy of the Lees-Hromas-Webb theory considers the turbulence structure of the far wake as basically similar to low speed turbulent structure. The verification obtained in these measurements supports that philosophy and lends credence to its use in describing electromagnetic backscatter. To the extent that the electron field can be considered locked to the flow field of the R/V wake, the understanding of electromagnetic backscatter has been enhanced, especially with respect to space correlation length  $\Lambda$  and the wake velocity. These quantities contribute to the radar cross section and Doppler, respectively. Both quantities have been shown to be predictable by the Lees-Hromas-Webb theory. Thus, R/V wake predictions using this theory have support from controlled laboratory measurements.

### 3.8 SPHERE WAKE MEASUREMENTS

Half-inch spheres were launched with near-zero scatter at 6500 fps, using a new smooth-bore gun. A wake measurement program was begun to better resolve velocity and temperature fluctuations. Higher probe temperatures (to 450°C), a greater range of probe temperatures (300°C), and a refined jet velocity instrumentation for calibration were employed in this program. An interruption in the program was allowed for the cone wake measurements, and the program was again underway at the end of



the contract period.

### 3.9 CONE WAKE MEASUREMENTS

Over 100 launchings of a 12-1/2 degree half-angle cone with 3/8-inch base diameter were accomplished, using a rifled barrel to obtain speeds of 6500 fps. Measurements were obtained using probe temperatures of 450°C. A range pressure of 100 mm was used to permit sabot separation with minimum scatter of the projectiles. Data records from eight launchings were delivered to the TRW Computer and Data Reduction Center. The reduction and statistical analysis of the data was underway at the end of the contract period. From these data, the correlation length scales will be obtained that are comparable with a slender reentry vehicle.

### 3.10 CONCLUSIONS

1. The understanding of electromagnetic scattering from reentry vehicle wakes has been enhanced by the verification of the Lees-Hromas-Webb theory under laboratory conditions. The measurements of space correlation length and wake velocity were adequately predicted by the theory these quantities being especially significant for radar backscatter.
2. Space correlation length for temperature fluctuations is the same as that for velocity fluctuations within the precision of the data.
3. Time correlation measurements can be made to much greater X/D than that for space correlation measurements.
4. Time correlation scales show no effect of off-axis location.
5. Comparison of the results to those in the turbulent wake behind a slender reentry vehicle will be possible when the data from the slender-cone program is reduced.
6. Mean wake velocities, densities and convection velocities in the wake can be measured with relative ease using anemometers in the ballistic range. Fluctuating components of velocity and density are more difficult to obtain.

### 3.11 RECOMMENDATIONS

1. The measurements of space correlation length and velocity and mass density fluctuations using anemometers should be extended to wakes behind projectiles with higher speeds, higher Mach number, larger diameter and varying shape. More complete comparison with slender-cone reentry vehicle wakes requires the variation of these important parameters.

2. Electron density fluctuations should be measured at the same time as the mass density fluctuations. Radar back-scatter measurements from reentry vehicle measurements can then be compared with the mass density measurements and electron density measurements available from the ballistic range.

## SECTION IV

### TURBULENT CHEMICALLY REACTING BOUNDARY LAYER (HYPERSONIC WAKE AND BOUNDARY LAYER TECHNOLOGY)

#### 4.1 INTRODUCTION AND BACKGROUND

The objective of this task is to develop an analytical description of the compressible, turbulent, chemically reacting boundary layer and to confirm the essential features of the theoretical model by experimentation. The primary reason for performing this task is to provide the necessary initial conditions for the calculation of the near wake. These calculations require definition of the dynamic, thermodynamic and chemical state of the boundary layer leaving the body.

The technical approach to this formidable problem has been to:

- Develop a theoretical description of an incompressible turbulent boundary layer;
- Extend the application of Coles' mathematical transformation to include pressure gradient, heat transfer and mass transfer in order to account for the effects of compressibility;
- Estimate the effect of turbulence on chemical reaction rates. (It has been assumed that the energy released by chemical reactions is sufficiently small that the fluid mechanical state of the boundary layer will not be affected.)

Emphasis has been placed on developing a sound theoretical model and not on quick programming to obtain meaningless numbers.

#### 4.2 LOW SPEED TURBULENT BOUNDARY LAYER

In order to gain insight into the important mechanisms of turbulent momentum transport, the case of a parallel turbulent shear flow has been considered prior to attacking the more difficult boundary layer flow.

A self-contained analysis for parallel turbulent flows in dynamic equilibrium has been derived. The theory predicts a priori the existence of the laminar sublayer and, when account of viscous dissipation effects near the wall is taken, agrees well with detailed experimental data for both mean and fluctuating quantities without the need for ad hoc fitting

constants. The detailed analysis and comparisons to experimental data are given in TRW Report 07854-6024-R000 entitled "A New Mixing Length Theory for Turbulent Flows in Dynamic Equilibrium" by W. H. Webb.

The advantage of the method developed, namely, the elimination of unnecessary empirical constants which have in the past been required to describe such flows, is clear. Examination of details of experiments performed in the past shows that these "constants" are not actually constant at all but rather may vary with Reynolds number, for example (see paper by J. O. Hinze "Turbulent Pipe Flow" in The Mechanics of Turbulence, Gordon and Breach, New York, 1964). Thus, an obvious advantage of the analysis developed is that variations of this kind are accounted for. Further, since the model may be applicable to boundary layers (as well as confined flows for which it was developed) questions which have arisen in the past such as whether the empirical "constants" are the same for pipe flow and boundary layer flow need no longer concern us. In addition, the applicability of the method to heat transfer and mass transfer calculations (Deissler has shown how this may be done) may permit such results to be obtained without further empiricism.

The approach for the extension of the above theory to the boundary layer has been defined. The physical situation is believed to be well represented by two regions: an inner region in which the flow behaves like a parallel flow, and an outer region in which the velocity does not deviate appreciably from the external velocity, thereby allowing an Oseen type approximation.

As in the model of Townsend, in the outer region energy is extracted from the mean flow by the turbulent shear stress  $\overline{u'v'}$ . The energy is converted to turbulent energy and dissipated mainly in the inner, nearly constant stress region. (See Figure 45.) Both regions are bounded by layers which are laminar in the sense that laminar shear dominates turbulent shear in these layers. The viscous sublayer plays the role of transferring stress to the wall; the viscous superlayer plays the role of converting nonturbulent fluid to turbulent fluid across an irregular (intermittent) boundary.

Mathematically these regions are conveniently (albeit approximately) described by a Couette flow approximation (constant shear) in the inner

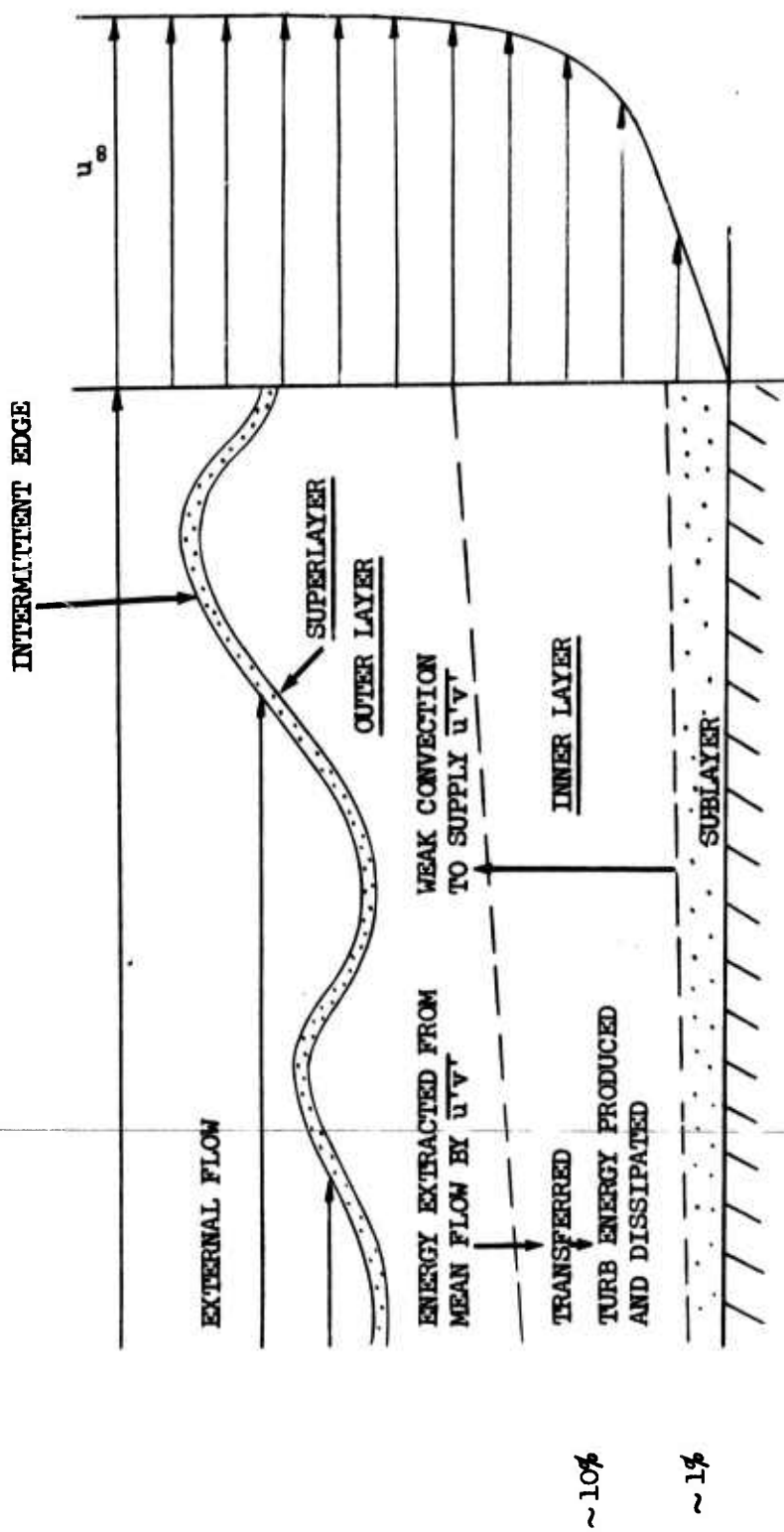


Figure 45. High Reynolds Number Turbulent Boundary Layer

region and an Oseen flow approximation (constant mean velocity) in the outer region.

If the scaling velocity for the turbulent shear is taken to be

$$\Delta U = U(d) - \frac{1}{d} \int_0^d U dy$$

where  $d$  is the inner layer height, then, as for the case of equilibrium channel flow, by representing the turbulent shear stress by

$$\tau_t = f(x, y) \left( \frac{\partial U}{\partial y} \right)^2$$

where  $f(x, y)$  is an unspecified function of  $x$  and  $y$ , the assumption of constant shear leads to a solution for  $f(x, y)$  which results in the normalized shear stress

$$\begin{aligned} \tau_t &= C_f \left( 1 - \frac{\delta_s}{y} \right) & \delta_s \leq y \leq d \\ \tau_t &= 0 & 0 \leq y \leq \delta_s \end{aligned}$$

where  $\delta_s$  is the sublayer thickness which is given by

$$\delta_s = \frac{R_s / R_\delta}{(C_f R_s)^{1/2}} \delta, \quad R_s = \frac{U(\delta_s) \delta_s}{\nu}$$

The velocity then can be obtained as

$$\frac{U}{U_\tau} = R_s^{1/2} \left[ 1 + \log R_s^{-1/2} \frac{y U_\tau}{\nu} \right]$$

where  $U_\tau$  is the friction velocity. This law is, of course, of the form  $\frac{U}{U_\tau} = A + B \log \frac{y U_\tau}{\nu}$  where the constants  $A, B$  are related to the sublayer Reynolds number  $R_s$ . As shown previously, this number appears from Laufer's data to be a universal constant.

While the inner region is known to be similar in the  $\frac{U}{U_\tau}$  vs.  $\frac{y U_\tau}{\nu}$  coordinate, the outer region is weakly non-similar (see e.g. Clauser). If the same scaling velocity method is also applicable in this non-equilibrium outer layer, an analytical representation for this layer may

also be obtained. We again take

$$\tau_t = f(x, y) \left( \frac{\partial U}{\partial y} \right)^2$$

for the outer region. It is convenient to let  $1 - U = a(x)g(\eta)$  where  $\eta = y/\delta$ , in which case the boundary layer equation gives for  $h$ , where  $h' = g$ ,

$$h''' \left( 2fh'' - \frac{1}{aR_\delta} \right) + f_\eta h''^2 = \delta' (1 - a'\delta) hh'' - \frac{\delta a'}{a} (1 - ah')^2$$

a third order equation in  $h$ . At this point, we use the Oseen approximation for the outer layer so that  $h \rightarrow \eta$  and  $h' \rightarrow 0$ , then calling  $G = g'$  we get

$$G' + \frac{f_\eta G^2 - \delta' (1 - a'\delta) \eta G + \frac{\delta a'}{a}}{2fG - \frac{1}{aR_\delta}} = 0$$

By assuming quasi-similarity, i.e., that  $a'$  may be neglected; and also by ignoring the superlayer, i.e., dropping the  $(aR_\delta)^{-1}$  term compared to the  $2fG$  term, we get

$$G' + \frac{f_\eta}{2f} G - \frac{\delta'}{2} \frac{\eta}{f} = 0$$

This equation may be solved for the velocity gradient  $G$  and, employing the velocity difference

$$\Delta U = 1 - \int_d^\delta U dy$$

as the scaling velocity, we obtain for the turbulent shear stress

$$\tau_t = C_f \left\{ 1 - \frac{\delta_s/\delta}{\eta_o} - \frac{\eta - \eta_o}{1 - 2(C_f R_s)^{1/2}} \right\}$$

where  $\eta_o = d/\delta$  is the normalized inner layer height.

In order to obtain  $\eta_o$  we conserve energy flux in the boundary layer by satisfying the integral mechanical energy equation



$$\delta' \theta_1 = 2 \int_0^1 \tau \frac{\partial U}{\partial \eta} d\eta$$

$$\theta_1 = \int_0^1 U(1 - U^2) d\eta$$

The result is

$$\frac{\eta_o^2 - (1 - 2a) \exp(1 - a^{-1}) \ln \eta_o}{\eta_o - 3a} = 1$$

where  $a = (C_f R_s)^{1/2}$ .

This equation has the solution shown in Figure 46 which indicates that for most turbulent boundary layers of interest where  $a \approx .1$  then  $\eta_o \approx 1$ . That is, the inner layer is about 10% of the total thickness of the boundary layer, a result in accord with experiment.

The boundary layer thickness is obtained by satisfying the integral momentum equation

$$\delta' \theta = C_f$$

$$\theta = \int_0^1 U(1 - U) d\eta$$

The result is the parametric set

$$\frac{x}{\delta_o} = \frac{R_s}{b_o} \left\{ (1 - 3b + b^2) \exp(b - b_o) - (1 - 3b_o + b_o^2) \right\}$$

$$\frac{\delta}{\delta_o} = \frac{b}{b_o} \exp(b - b_o), \quad C_f = (R_s b^2)^{-1}$$

$$b_o \exp b_o = e \frac{R_{\delta o}}{R_s}$$

These results are shown in Figures 47 and 48.

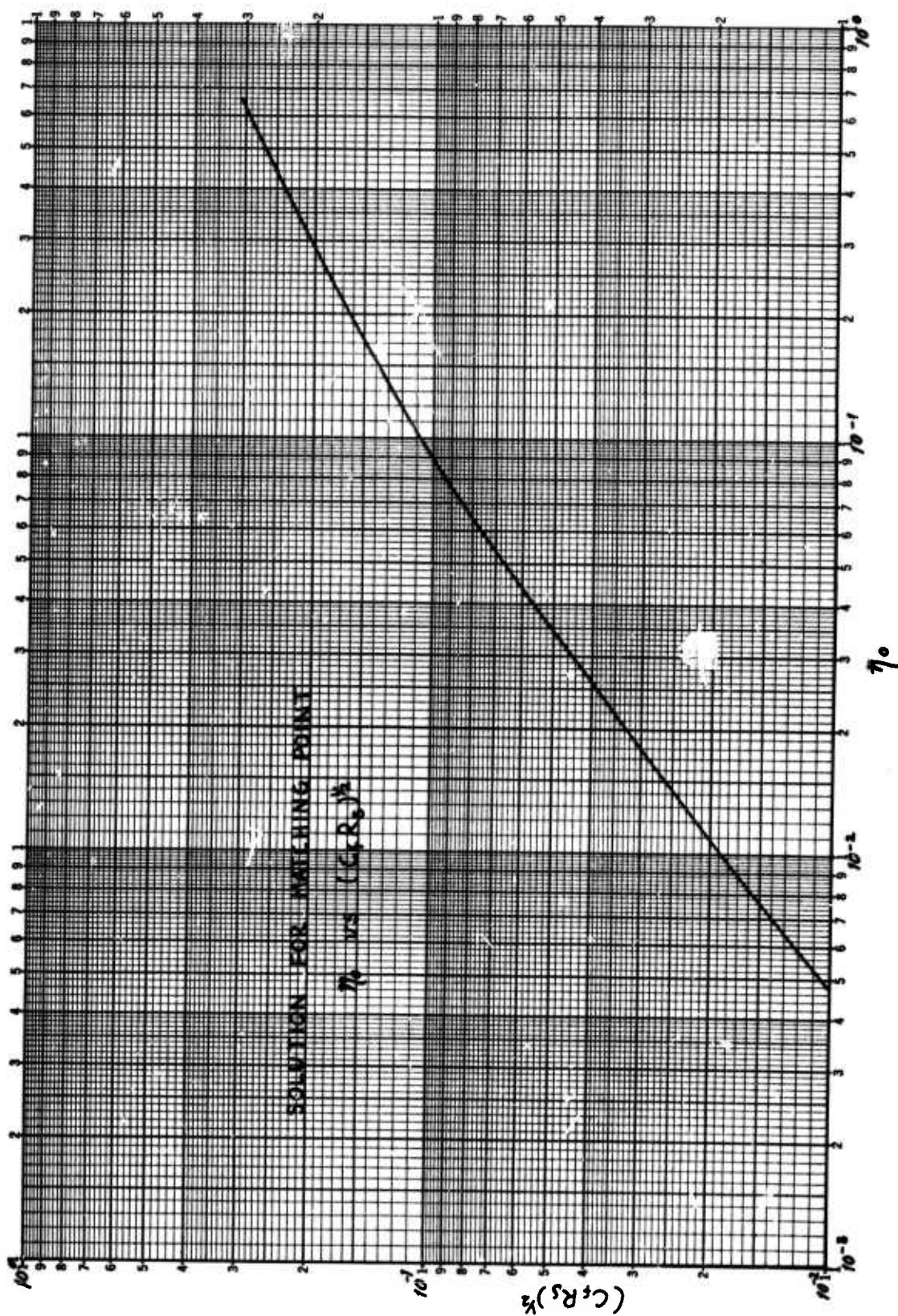


Figure 46. Solution for Matching Point,  $\eta_0$  vs.  $(C_f R_s)^{1/2}$

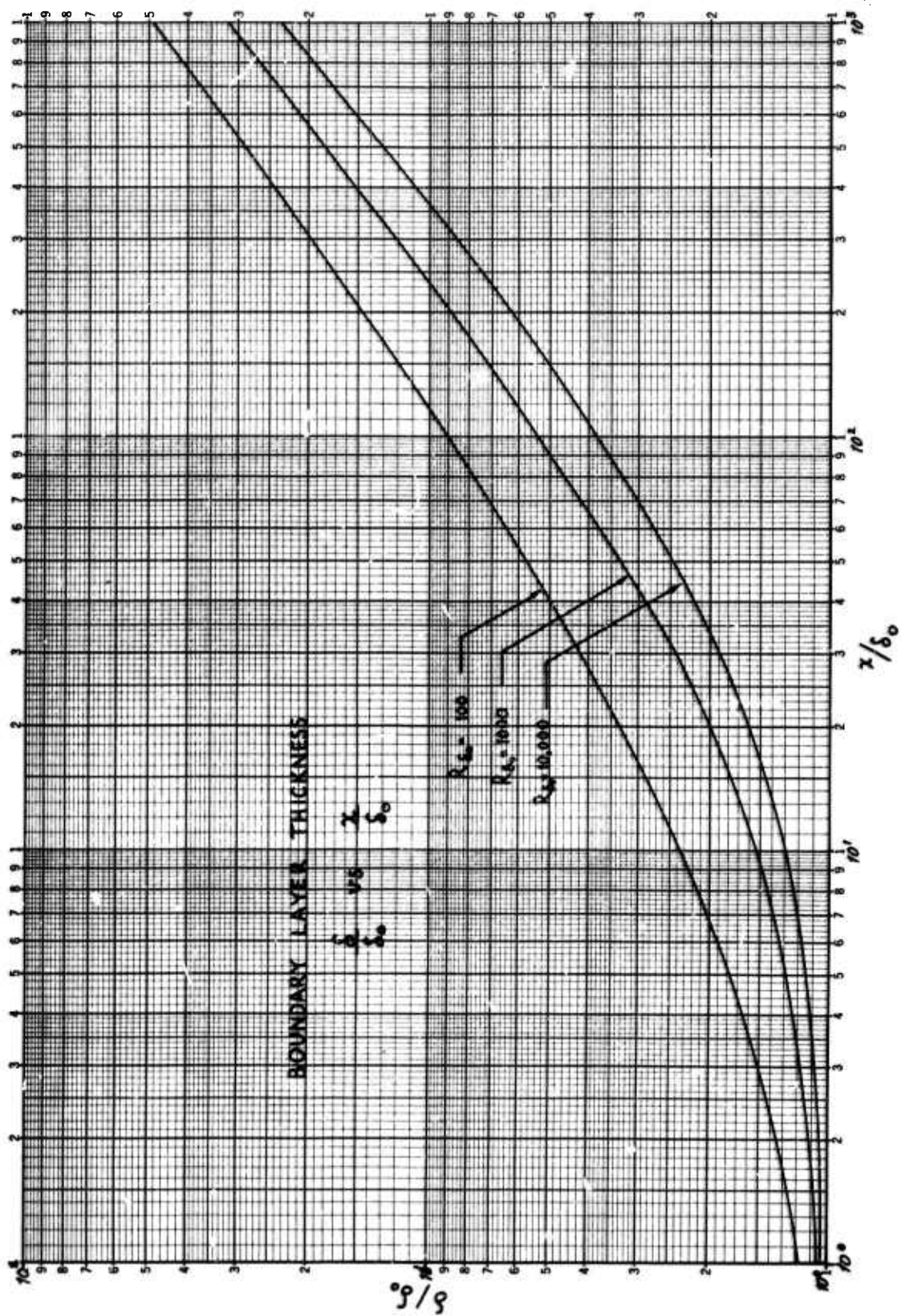


Figure 47. Boundary Layer Thickness,  $\frac{\delta}{\delta_0}$  vs.  $\frac{x}{\delta_0}$

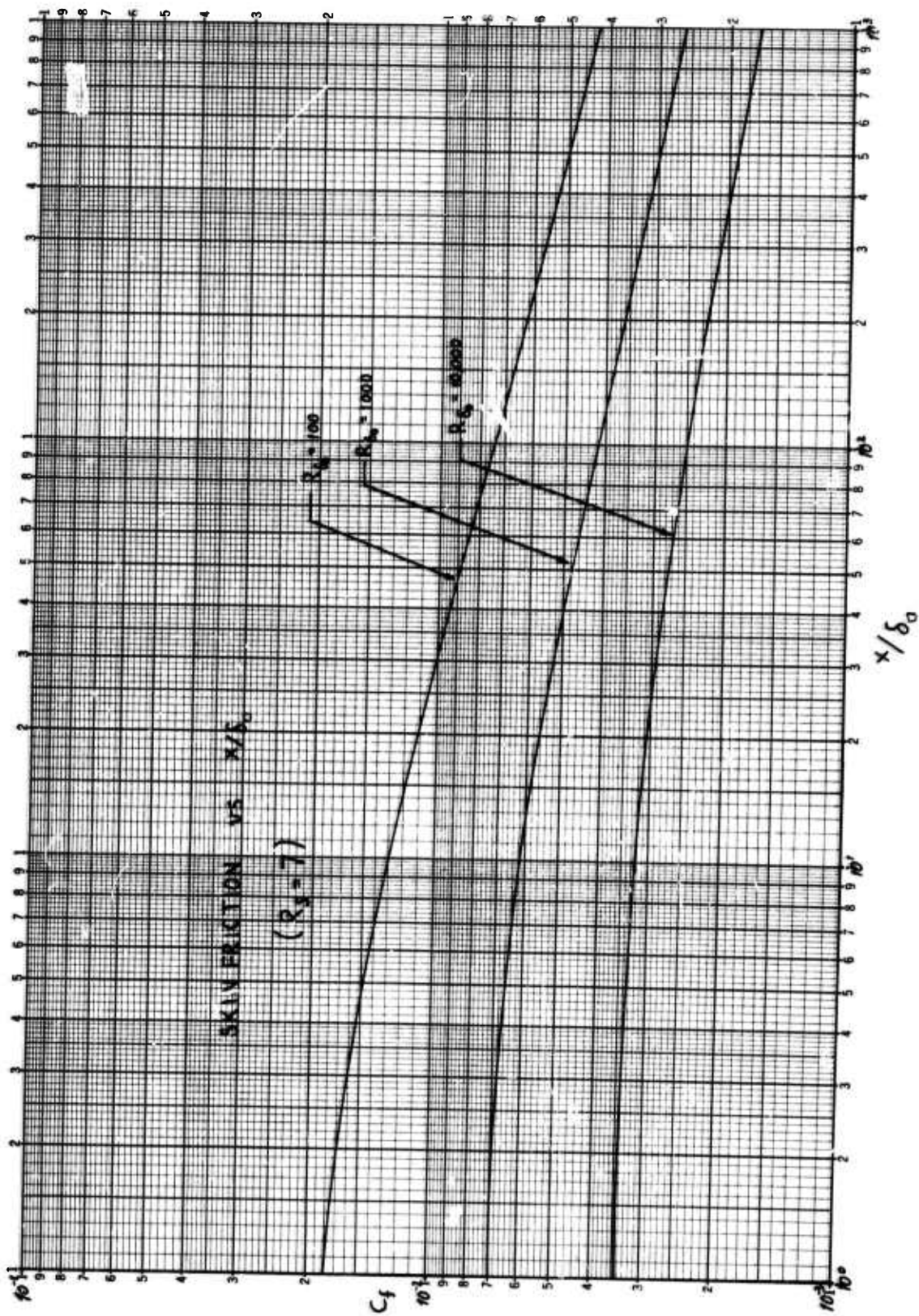


Figure 48. Skin Friction vs.  $\frac{x}{\delta_0}$



The procedure outlined above thus provides a general method for obtaining detailed properties of the turbulent boundary layer with a minimum of empirical data. In order to obtain quantitative accuracy it is expected that, as in the channel flow case, the effect of viscous dissipation on the turbulent shear stress near the wall must be taken into account. Further, the effect of intermittency on reducing the shear stress of the outer layer must also be included. These effects can be added as corrections in a straightforward way and work on this is in progress.

Of course, the accuracy of this method must be tested against experiment as for the channel flow case; however, it is clear that if an accurate representation of the turbulent shear stress does result, then the method may be applied directly (as shown, e.g., by Deissler) to the calculation of the transport of mass or energy in the turbulent boundary layer without further empirical data. The extension of this method to such cases as well as to cases with pressure gradient, blowing, and compressibility effects then holds the promise of reducing much of the empiricism currently required for the analysis of such problems.

#### 4.3 COMPRESSIBILITY TRANSFORMATION

The application of Coles' transformation to boundary layers with pressure gradient, heat transfer and mass transfer has been accomplished to the extent of deriving the complete set of laws of corresponding stations which govern these parameters:

$$C_f R_\theta = \bar{C}_f \bar{R}_\theta \quad \begin{array}{l} \text{Skin friction} \\ \text{(previously derived by Coles)} \end{array}$$

$$\frac{\rho_e}{\rho_w} \frac{\theta}{\tau_w} \frac{dp}{dx} = \frac{\bar{\rho}_e}{\bar{\rho}_w} \frac{\bar{\theta}}{\bar{\tau}_w} \frac{d\bar{p}}{d\bar{x}} \quad \text{Pressure gradient}$$

$$\frac{\theta}{T_e} \left( \frac{\partial T}{\partial y} \right)_w = \frac{\bar{\theta}}{\bar{T}_e} \left( \frac{\partial \bar{T}}{\partial \bar{y}} \right)_w \quad \text{Heat transfer}$$

$$\frac{\rho_w V_w}{\rho_e u_e} R_\theta = \frac{\bar{\rho}_w \bar{V}_w}{\bar{\rho}_w \bar{u}_e} \bar{R}_\theta \quad \text{Mass transfer}$$

The details of the analysis can be found in TRW Report 07854-6065-R000 entitled "The Compressible Boundary Layer with Pressure Gradient, Heat Transfer and Mass Transfer and Its Low Speed Equivalent," by J. E. Lewis.

#### 4.4 CHEMICAL KINETICS

##### 4.4.1 Hypersonic Boundary Layer Kinetics

The first effort undertaken in the study of turbulent fluctuation effects on chemical kinetics was the determination of certain laminar or molecular chemical relations needed for a practical application to the boundary layer of an ablating R/V, setting aside for the moment the problem of applying these relations to turbulent flow. The particular case of an ablating graphite boundary layer was chosen for its relative simplicity.

The thermochemical model of dissociated air flowing over a pure carbon surface was selected for detailed study since, at surface temperatures below  $3000^{\circ}\text{K}$ , there are only nine important electron-producing and thermally significant species, (namely,  $\text{N}_2$ ,  $\text{N}$ ,  $\text{O}_2$ ,  $\text{O}$ ,  $\text{NO}$ ,  $\text{NO}^+$ ,  $\text{e}^-$ ,  $\text{CO}$  and  $\text{CO}_2$ ), gaseous carbon being noteworthy by its absence at these temperatures but not at higher temperatures.

A set of ten homogeneous reactions and three heterogeneous reactions were identified through a literature survey as the significant reactions involving the above nine species. These reactions and their corresponding rate constants are presented in Table III. The rates for reactions I through VII were obtained from Reference 28. The rates for the homogeneous reactions VIII, IX and X were taken from References 29, 30 and 31, respectively. The rates for the heterogeneous reactions XI, XII and XIII were extracted from References 32, 33 and 34, respectively.

A method was needed to transpose these molecular relations into a calculation method to describe the time average of the fluctuating turbulent flow and chemistry in the boundary layer. It was clear from the outset that the time-average properties of mass-fraction, density, and temperature could not be substituted into the laminar or molecular expressions for chemical kinetics to produce an "effective" turbulent reaction rate. The effect of mixing, for example, cannot be described by such a method.

An examination of the Rubel-Zeiberg (Reference 35) theory for the effective turbulent reaction rate was undertaken. The essence of the theory is the substitution of mean-plus-fluctuating properties into the molecular or laminar kinetics relation and then taking the time average of the resulting expression. The new terms that are generated are average products of two or three fluctuating quantities such as the density,  $\rho$ ; mass fraction of each species,  $\alpha_i$ ; and temperature rate factor of each reaction,  $k_{ij}$ . It is evident that the number of these average products, or correlation coefficients, that appear increase extremely rapidly with the number of reactants present and with the number of important reactions. In fact, the application of the Rubel-Zeiberg method to the ten homogeneous reactions listed in Table I would require values for approximately 200 correlation coefficients. The magnitude of these coefficients could only be estimated for a few of the air species reactions and were unknown for the remaining reactions. Efforts to apply the method to the R/V boundary layer ceased and attention was turned to experimental methods to obtain the effect of a fluctuating field on the chemical kinetics. These efforts included the definition of an experiment to be conducted in a wind tunnel and the studies of water-tunnel experiments and suitable low-speed theories.

#### 4.4.2 Water-Tunnel Kinetics Experiments

A literature search yielded a series of three experiments in a water tunnel (References 36, 38), the last of which measured the effective rate of reaction in the wake of a cylinder. One opaque reactant was injected through the porous wall of a cylinder, the other transparent reactant being in the free stream. Reaction rate was measured by time photographs of the disappearing wake. The calibrated photographs were measured with a densitometer. Profiles were thus obtained as well as integrated quantities across the wake. The mean concentrations and the cylinder sizes were varied. Injection was also done in the wake of the large cylinder, using a small tube as a "line source".

For this irreversible reaction, the molecular reaction rate term was  $k C_1 C_2$ , where  $k$  was a constant for the isothermal experiment and  $C_1$  and  $C_2$  are the two reactant concentrations. Thus the experimental



Table III. Chemical Reactions and Rate Constants

Number	Reaction	Third Body (p)	Forward Rate Constant	Units
I	$2O + (p) \xrightleftharpoons[k^I]{k^I} O_2 + (p)$	N, NO, NO <sup>+</sup> -e <sup>-</sup> N <sub>2</sub> , CO, CO <sub>2</sub> O <sub>2</sub> O	$k^I = 3.01 \times 10^{15} T^{-1/2}$ $k^I = 6.02 \times 10^{15} T^{-1/2}$ $k^I = 8.00 \times 10^{19} T^{-3/2}$ $k^I = 2.24 \times 10^{20} T^{-3/2}$	$\frac{cm.^6}{Mole^2 \text{ sec.}}$
II	$2N + (p) \xrightleftharpoons[k^{II}]{k^{II}} N_2 + (p)$	O <sub>2</sub> , O, NO, NO <sup>+</sup> -e <sup>-</sup> N <sub>2</sub> , CO, CO <sub>2</sub> N	$k^{II} = 1.09 \times 10^{16} T^{-1/2}$ $k^{II} = 2.76 \times 10^{16} T^{-1/2}$ $k^{II} = 2.36 \times 10^{21} T^{-3/2}$	$\frac{cm.^6}{Mole^2 \text{ sec.}}$
III	$N + O + (p) \xrightleftharpoons[k^{III}]{k^{III}} NO + (p)$	N <sub>2</sub> , N, O <sub>2</sub> , O CO, CO <sub>2</sub> NO, NO <sup>+</sup> -e <sup>-</sup>	$k^{III} = 1.02 \times 10^{20} T^{-3/2}$ $k^{III} = 2.04 \times 10^{21} T^{-3/2}$	$\frac{cm.^6}{Mole^2 \text{ sec.}}$
IV	$O_2 + N \xrightleftharpoons[k^{IV}]{k^{IV}} NO + O$		$k^{IV} = 1.33 \times 10^{10} T e^{-3560/T}$	$\frac{cm.^3}{Mole \text{ sec.}}$
V	$NO + N \xrightleftharpoons[k^V]{k^V} N_2 + O$		$k^V = 1.63 \times 10^{13}$	$\frac{cm.^3}{Mole \text{ sec.}}$
VI	$2NO \xrightleftharpoons[k^{VI}]{k^{VI}} N_2 + O_2$		$k^{VI} = 2.41 \times 10^{23} T^{-5/2} e^{-43000/T}$	$\frac{cm.^3}{Mole \text{ sec.}}$
VII	$NO^+ + e^- \xrightleftharpoons[k^{VII}]{k^{VII}} N + O$		$k^{VII} = 1.81 \times 10^{21} T^{-3/2}$	$\frac{cm.^3}{Mole \text{ sec.}}$
VIII	$CO_2 + (p) \xrightleftharpoons[k^{VIII}]{k^{VIII}} CO + O + (p)$	N <sub>2</sub> , N, O <sub>2</sub> , O, NO, NO <sup>+</sup> -e <sup>-</sup> , CO CO <sub>2</sub>	$k^{VIII} = 5.33 \times 10^{11} T^{1/2} e^{-39800/T}$	$\frac{cm.^3}{Mole \text{ sec.}}$
IX	$CO + O_2 \xrightleftharpoons[k^{IX}]{k^{IX}} CO_2 + O$		$k^{IX} = 3.5 \times 10^{12} e^{-25500/T}$	$\frac{cm.^3}{Mole \text{ sec.}}$
X	$CO_2 + N \xrightleftharpoons[k^X]{k^X} CO + NO$		$k^X = 2.47 \times 10^{15} T^{-1.0}$	$\frac{cm.^3}{Mole \text{ sec.}}$

Table III. Chemical Reactions and Rate Constants (Continued)

Number	Reaction	Third Body (p)	Reaction Order	Units
XI	$C(s) + CO_2 \xrightarrow{k^{XI}} 2CO$	$k^{XI} = 2.6 \times 10^9 e^{-\frac{43000}{T}}$	1	$\left(\frac{C \text{ Atoms}}{CM^2 \text{ sec.}}\right) \left(\frac{CO_2 \text{ Molecules}}{CM^3}\right)^{-1}$
XII	$2C(s) + O_2 \xrightarrow{k^{XII}} 2CO$	$k^{XII} = 2.57 \times 10^3 T^{3/2} e^{-\frac{1000}{T}}$	1/2	$\left(\frac{C \text{ Atoms}}{CM^2 \text{ sec.}}\right) \left(\frac{O_2 \text{ Molecules}}{CM^3}\right)^{-1/2}$
XIII	$C(s) + O \xrightarrow{k^{XIII}} CO$	$k^{XIII} = 1.82 \times 10^3 T^{3/2} e^{-\frac{1000}{T}}$	1/2	$\left(\frac{C \text{ Atoms}}{CM^2 \text{ sec.}}\right) \left(\frac{O \text{ Molecules}}{CM^3}\right)^{-1/2}$

situation could be described by allowing mean and fluctuating concentrations to be averaged. The resulting effective reaction rate term was  $k(\bar{C}_1\bar{C}_2 + \overline{C_1'C_2'})$ , where  $\bar{C}_1$  and  $\bar{C}_2$  are mean concentrations,  $C_1'$  and  $C_2'$  are the fluctuating concentrations and  $\overline{C_1'C_2'}$  is the average product or correlation coefficient. An equation was generated for  $\overline{C_1'C_2'}$ , the terms being identified and assessed as to their significance. An effect of incomplete mixing was identified that later proved to be especially significant for calculations of fast reactions. For incomplete mixing,  $\overline{C_1'C_2'}$  tended to become negative, thus reducing the effective reaction rate  $k(\bar{C}_1\bar{C}_2 + \overline{C_1'C_2'})$  below  $k\bar{C}_1\bar{C}_2$  which is the rate for the ideal case of complete mixing on a molecular level. Unmixed reactants passing by a point in the flow field contribute to the mean concentration term, but the actual reaction was only taking place on the edge of the "clumps" of the reactants where just a few of the reactant molecules were mixed. It should be noted that the effective turbulent reaction rate is still higher than that for a laminar wake flow because the reactants are turbulently dispersed over a larger volume and partially mixed, creating many more sharp gradients for molecular diffusion than would exist in a laminar flow. The comparison of the equations with the theory was limited because only one of the two reactants was measured. It was evident, however, that the effect of incomplete mixing compared with ideal complete mixing was similar to the effect of a nonequilibrium reaction in that the reaction is delayed. Further, it also is evident that the  $\overline{C_1'C_2'}$  term which was typical of the Rubel-Zeiberg terms, was a variable throughout the flow field and not a constant.

The fast-reaction theory of Toor (Reference 39) was investigated toward the end of the contract period. It treats the limiting case of reactions that are fast compared with the rate of molecular diffusion. Parts of the Toor theory were developed in the study of turbulent flames (Reference 40) which are an example of diffusion-limited reactions. For isotropic turbulent mixing that was induced by a grid in a pipe, the theory has been verified (Reference 41) experimentally. It should be noted that the theory requires mean and fluctuating values of one reactant undergoing diffusion or mixing without the other being present. Thus, a mixing experiment is an input and the mean concentrations during the reaction is

the output of the theory. The actual kinetics of the reaction are eliminated from the problem by a transformation of variables that is based on equilibrium kinetics for the reaction rate terms in the instantaneous species conservation equations. Thus the actual reaction rate need not be known if it is fast compared to diffusion.

The Toor theory was compared with the results of the cylinder-wake experiment previously discussed. It should be noted that the molecular diffusion and reaction rates were not measured in this experiment. Moreover, they were not found in a literature search conducted during this study. The fact that the reaction is one of the fastest known to chemical analysts led to the belief that the experiment may be diffusion-controlled and thus be comparable to the theory of Toor. The major agreement between the Toor theory and the cylinder-wake experiment occurred on the wake axis. There the effective reaction rate from both the measurements and theory was higher because the mixing was greater.

It is clear from the low-speed water-tunnel studies undertaken thus far that diffusion or mixing must be studied at the same time as fluctuation effects on nonequilibrium chemistry. A practical calculation scheme for low-speed isothermal flows must specify the relation between diffusion, reaction and convection for each species and reaction occurring at each point in the turbulent flow. Some additional progress can be made by continued studies of the Toor theory for fast reaction and the Rubel-Zeiberg theory for slow reactions, as described above. It is clear, however, that a complete description of the reentry-vehicle boundary-layer flow and chemistry awaits additional experimental data on chemical reactions in gases undergoing turbulent flow. There, the effects of temperature and density fluctuations on the effective reaction rate will be revealed.

#### 4.4.3 Wind-Tunnel Kinetics Experiment

Under a TRW-sponsored program, a low speed wind tunnel has been designed and is in the process of being acquired with TRW funds. Experiments using dissociation and recombination of nitrogen oxides in turbulent flow at elevated temperatures are being planned. Both mean and fluctuating concentrations of  $\text{NO}_2$  will be measured locally with a light probe.

The attenuation of light at the proper wavelength passing over a short gap in the flow will be a direct measure of the  $\text{NO}_2$ , the other species being transparent at that wavelength. The light path in the flow will be between the ends of a fiber optics probe. Thus, the averaging length of the light beam will be a minimum consistent with the sensitivity of the instrumentation. Conditions in the tunnel will be established so that a wide range of reaction rates in turbulent flow can be examined by utilizing a range of elevated temperatures and flow configurations. Buoyancy effects will be minimized by utilizing vertical flow in the test section. Thus, the needed experimental data on fluctuation effects on chemical reactions in turbulent gaseous flow will be obtained.

#### 4.5 CONCLUSIONS

Considerable progress has been made in each of the areas of this task. The approach originally outlined still appears to offer the most promise with respect to accomplishing the overall objective of this task.

#### 4.6 RECOMMENDATIONS

TRW recommends that the following steps be taken to complete the analysis:

- Include the effects of viscous dissipation and intermittency in the low speed boundary layer analysis.

- Derive the actual scaling functions necessary to model a high speed flow to its low speed equivalent.

- Apply the transformation to the low speed analytical model.

- Complete the analysis required for the determination of the chemical kinetics.

- Include chemistry in the analytical boundary layer model.

- Verify, to whatever extent it is feasible, this model by comparison to experiment.

## SECTION V

### IMPROVED LAMINAR WAKE (HYPERSONIC WAKE AND BOUNDARY LAYER TECHNOLOGY)

#### 5.1 INTRODUCTION AND BACKGROUND

The objective of this task is to obtain a more accurate description of the extended slender body far wake in order to interpret recent ICBM flight data and ballistic range data, as related to the "break-through" problem (i.e., the radar return from slender body wakes seems to imply that the turbulent inner viscous core is shielded by an overdense rotational outer wake for a considerable distance downstream of the transition zone, and thus the turbulent front of the inner core is not observed until it "breaks through" this ionized portion of the outer wake).

The accomplishment of the Improved Laminar Wake task required two major activities:

- (a) programming of the TRW finite difference wake solution for 50 radial mesh points,
- (b) prediction of "breakthrough" and comparison with test data.

The first of the above activities was initially completed for the G. E. 635 computer. However, systems difficulties associated with this computer so degraded its reliability that the wake program was finally transferred to the C. D. C. 6600 machine. A sample calculation has been made to illustrate the scheme for describing the complete slender body far wake, and the details of this method are present in 5.3.

The TRW wake program of interest uses a finite difference method to solve the viscous wake equations for nonequilibrium flow. Initial conditions and outer edge conditions are arbitrary input data, and either laminar or turbulent transport properties may be used. The conservation equations, transformations, and numerical methods utilized in this program are presented in Reference 42.

The laminar version of the nonequilibrium wake program considers seven air species ( $N_2$ ,  $N$ ,  $O_2$ ,  $NO$ ,  $NO^+$ ,  $e^-$ ) plus one inert contaminant. Local equilibrium of vibrational and electronic excitation is assumed for

all species. Ambipolar diffusion is adopted for the  $\text{NO}^+ - \text{e}^-$  pair, and the complete multicomponent equations of Reference 43 are used to calculate the transport properties of the gas mixture (including thermal diffusion). The turbulent version of the program uses transport properties based on the eddy diffusivity concept (Reference 44) and also includes the two additional species  $\text{O}^-$  and  $\text{O}_2^-$ .

## 5.2 TECHNICAL APPROACH

One of the more interesting features of the far wake is that the radial pressure gradient,  $\partial p / \partial r$ , is small across both the inner and outer wake. This implies that the classical boundary layer approximations to the Navier-Stokes equations can be used for both flow regions. Hence, the major effort within this task was directed toward the problem of extending an existing TRW computer program which currently describes the inner viscous core of the nonequilibrium laminar wake downstream of the critical point, radially outward into that cold gas portion of the wake which is both upstream of transition and within the envelope of the wake and body shocks (Figure 49).

The techniques discussed in Section VI were employed to describe the outer flow at the beginning of the laminar far wake region; initial conditions for the inner viscous core will be estimated by using test data. The TRW integral method was utilized for the turbulent wake.

As noted above, the radial extension of the laminar wake solution does represent an improvement over the traditional method of allowing a viscous region to grow into a rotational inviscid flow in that once the initial conditions are established, no arbitrary separation of viscous laminar and inviscid rotational flow regimes is required; boundary conditions are applied in the cold undissociated flow at the extreme edge of the outer wake. Thus, the problem of matching gradients at the interface between the inner and outer wake is avoided. The rate at which the inner and outer wakes merge is governed by the molecular transport properties of the gas and was determined in the course of the calculation.



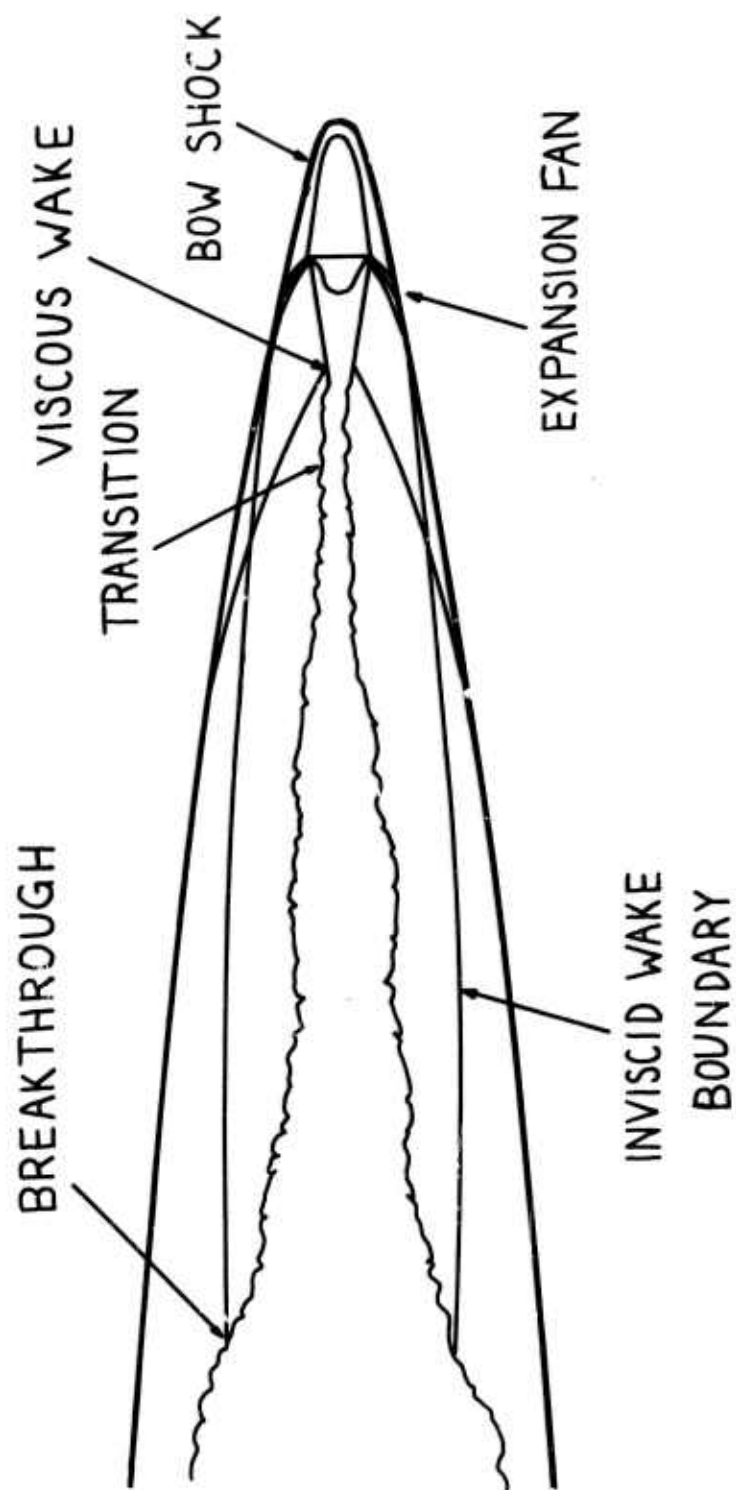


Figure 49. Flow Field Sketch

### 5.3 RESULTS

A far wake calculation was performed to compare "breakthrough" with the observed ballistic range results of Reference 58. The body was a 12.5 half-angle cone of .06 bluntness ratio with a base diameter of .25 inches. A velocity of 23,400 ft/sec and an ambient pressure of 75 torr were considered. The freestream Reynolds number  $R_{e,D}$  was  $3 \times 10^5$ . Transition of the viscous inner core from laminar to turbulent was assumed to occur at 50 X/D.

General results of the calculation are not presented herein; however, the radial enthalpy variation at the beginning and end of the laminar wake are indicated in Figure 50.

Growth of the turbulent core is shown in Figure 51 along with the predicted inviscid edge boundary. This calculation indicates "breakthrough" to occur about 300 body diameters downstream of the base. This is in agreement with the distance observed in Reference 58.

### 5.4 CONCLUSION

In conclusion, the TRW finite difference wake program has been modified to provide better radial definition of the laminar far wake. This program was successfully utilized in a calculation to determine the location of "breakthrough"; prediction and observation agreed satisfactorily.

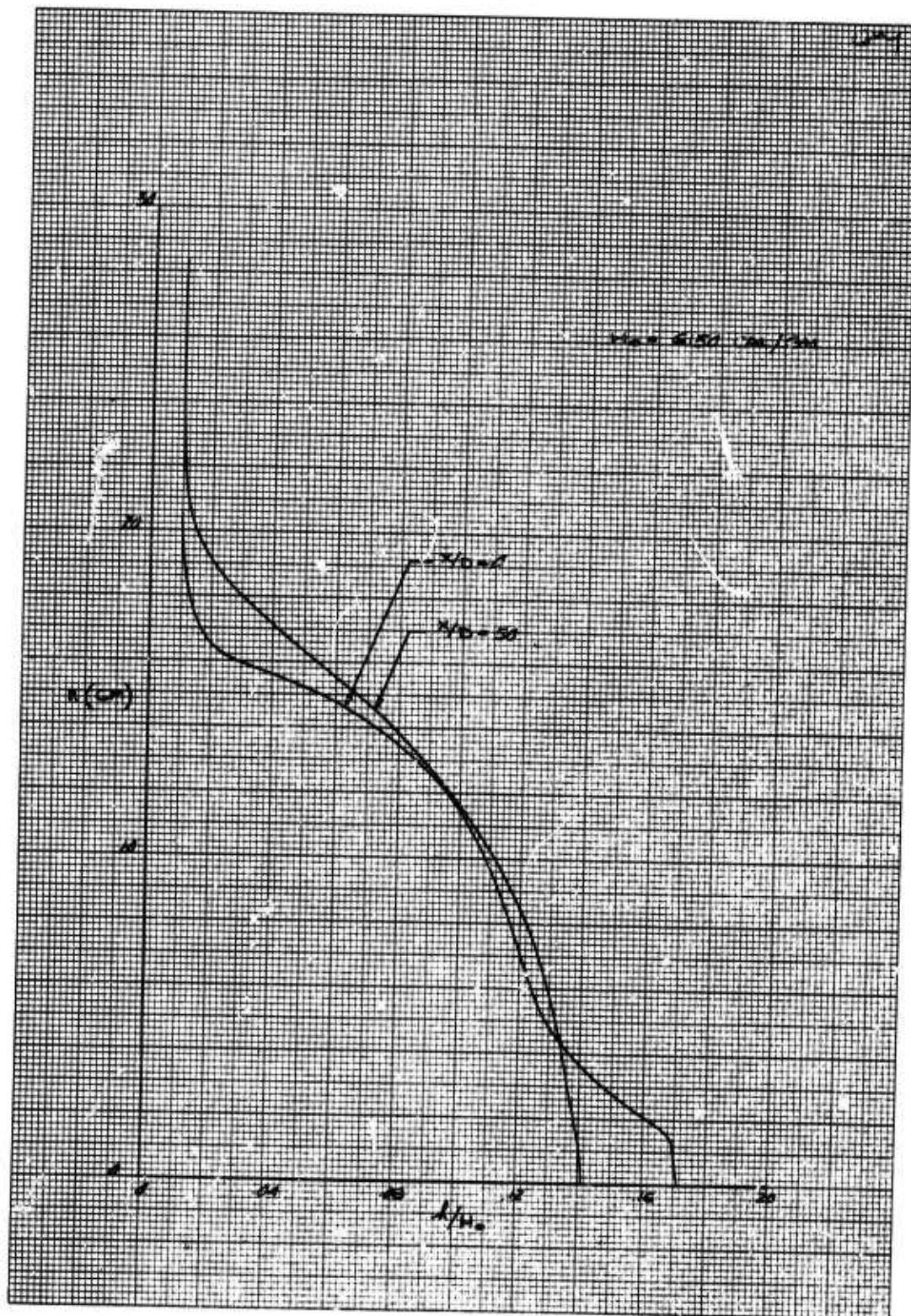


Figure 50. Radial Enthalpy Variation

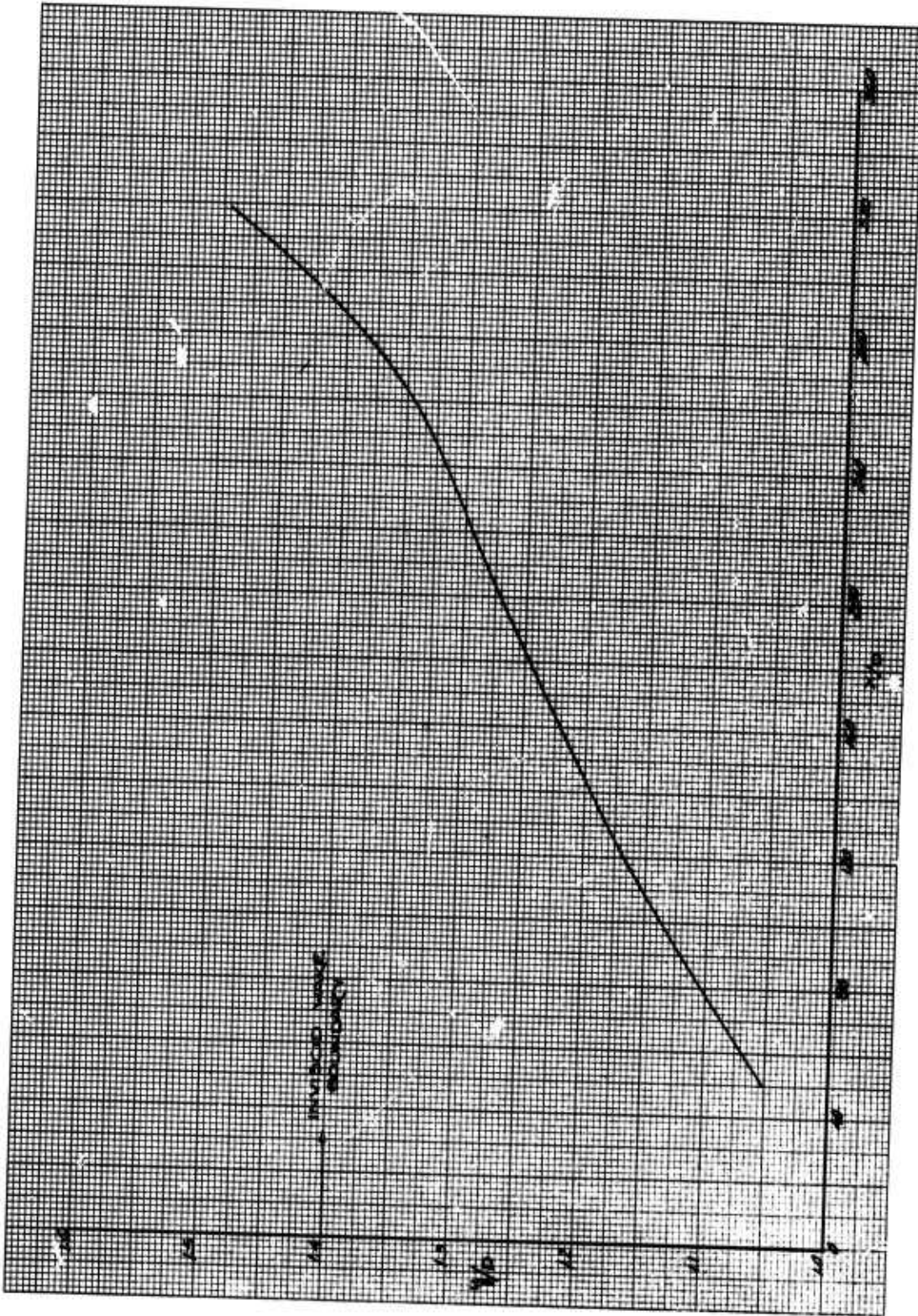


Figure 51. Turbulent Wake Growth



SECTION VI  
NEAR WAKE  
(HYPERSONIC WAKE AND BOUNDARY LAYER TECHNOLOGY)

6.1 INTRODUCTION AND BACKGROUND

The near wake of a slender body in hypersonic flow is a region of strong viscous interaction where large changes in pressure, flow direction, velocity, and temperature occur over but a few base diameters. It is the region which literally "sets the stage" for the flow hundreds of base diameters downstream, where much of the interest is on radar observables. In fact, electrons and contaminants from the boundary layer pass into the near wake where their concentrations are altered. In addition, electrons themselves can be produced due to the presence of local high temperatures brought about by viscous dissipation.

Since the near wake is instrumental in controlling the downstream flow, it must be a part of the development of a mathematical model for wake flows. However, the presence of many coupled and complex fluid dynamic phenomena in this relatively small region has made its analysis very difficult. As a result, various aspects have been studied in turn at TRW with the intent of establishing: 1) the basic mathematical methods which can be used in the overall problem, 2) models of various portions of the flow field, and 3) coupling schemes for joining the various regions. Background and more detailed descriptions of these efforts are discussed in the following paragraphs.

In the near wake region of a hypersonic slender body, shown in Figure 52, we are concerned with the analytical determination of the steady state flow field. There are two basic approaches to this problem. The first is to treat the steady state as the asymptotic limit of a time dependent solution. If we limit ourselves to continuum flow, the problem becomes mathematically parabolic in time with two space variables. There are some conceptual difficulties with the determination of downstream boundary conditions but this approach seems attractive for problems with a very small Reynolds number. However, for the Reynolds numbers we are interested in, the computing speed and storage capacity

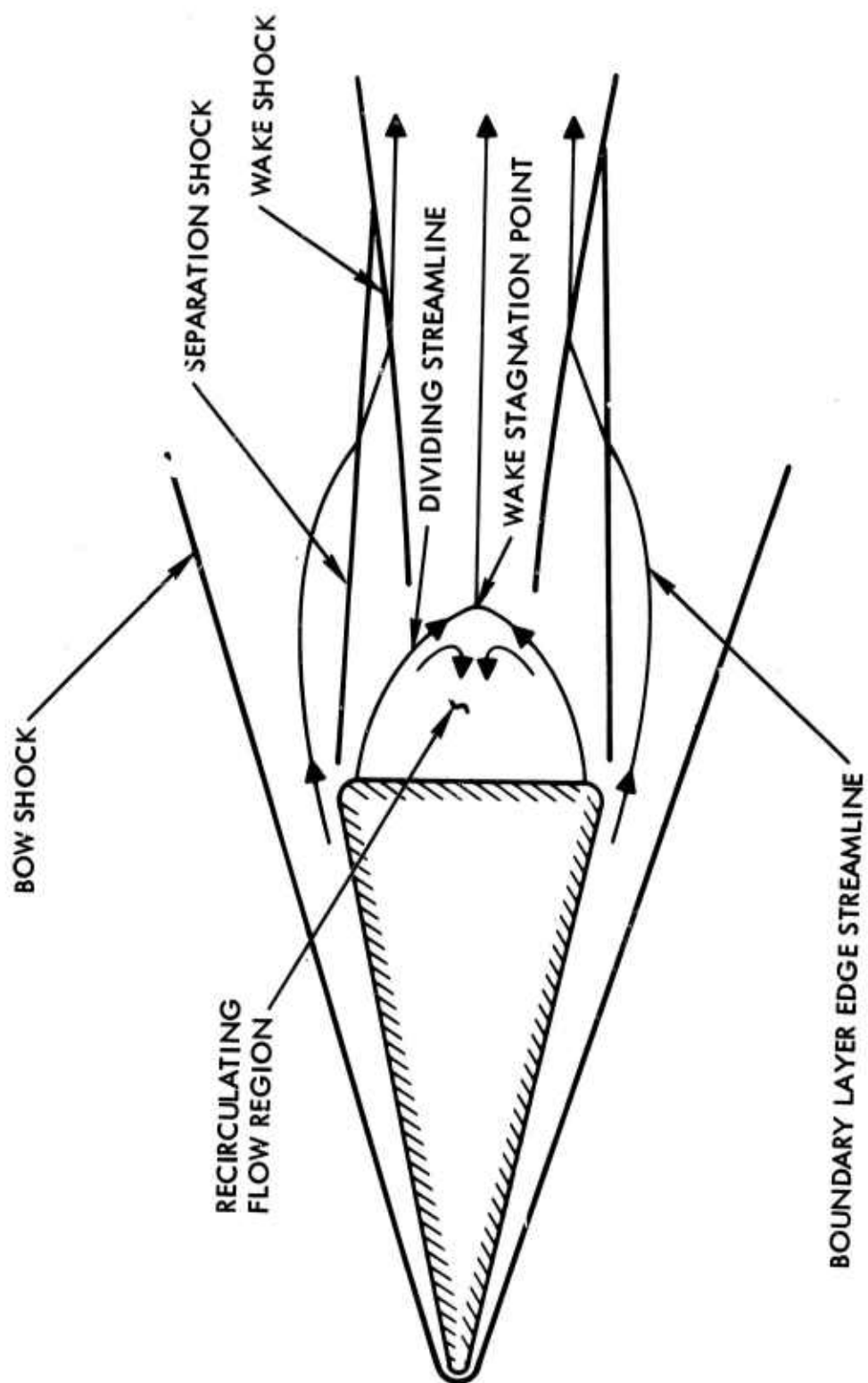


Figure 52. Slender Body Near Wake

needed to obtain the required spatial resolution are beyond the capabilities of current computers.

The second approach to this problem is to formulate it directly in terms of steady state equations. We will concern ourselves here only with continuum laminar flow described adequately by the steady state Navier-Stokes equations. The formal mathematical nature of these equations indicates that this then becomes a boundary value problem; that is, its solution requires the specification of boundary conditions along all boundaries. If no further simplifying assumptions are made, the problem formulated in this way suffers from the same difficulties at the Reynolds numbers of interest as does the time dependent approach. Fortunately however there are regions of the flow in which some of the higher order terms of the Navier-Stokes equations become negligible. For instance, the flow over the major portion of the body can be divided into a boundary layer and an outer inviscid supersonic flow, with the equations describing each region obtained by neglecting higher order terms in the Navier-Stokes equations. The boundary layer equations have a parabolic character, the inviscid supersonic flow equations are hyperbolic, and both are, of course, initial value problems. If the requisite boundary conditions are known a priori, as they are for these two problems, the calculation proceeds in a straightforward manner by marching in a generally downstream direction.

## 6.2 CORNER FLOW

As the body shoulder is approached, this rather simple flow model begins to become inadequate since it is then no longer possible to divide the flow into a constant pressure viscous (boundary layer) region and an exterior inviscid flow. The upstream influence of the low base pressure on the approaching boundary layer produces a strong streamwise pressure gradient and a corresponding cross-stream pressure gradient in the supersonic viscous region. Considerable progress has been made under the current Penetration Systems Studies contract toward the understanding of this flow region and the development of methods of computing the flow properties in detail. Reference 45 describes the analysis of flows approaching a sharp corner; Reference 46 includes, in addition, an analysis of the flow up to and around a rounded corner to the separation



point. In these analyses, the boundary layer equations are used to describe the subsonic portion of the flow with the effect of transverse pressure gradients in the supersonic viscous region included through the use of an inviscid transverse momentum equation. A relation between pressure and flow angle at the outer edge is obtained by coupling with an outer inviscid region. Initial profiles are assumed to be similar (Blasius) in shape, but with the boundary layer edge flow inclination not specified. When the equations are solved by an implicit finite difference method, it is found that the qualitative nature of the downstream flow is determined by the particular value of initial edge flow inclination chosen, with two families of solutions: either there is an unfavorable pressure gradient with boundary layer separation downstream, or there is a precipitous drop in pressure along the wall. Bounding these two families of solutions is the particular solution which continues downstream on the body without separation. In this formulation, higher order Navier-Stokes terms whose function is to determine the location of the separation point have been neglected. In the absence of these terms, solutions can be generated corresponding to all possible locations of the separation point and the appropriate solution is chosen by using independent information. This is illustrated in Figure 53, which shows the wall pressure distribution along the rounded base of a wedge. The experimental pressures measured by Hama (Reference 47) are given by the bars, and the solid lines are members of the computed families of pressure distributions. The family for which the pressure reaches a minimum and then begins to rise corresponds to solutions separating from the curved wall under an adverse pressure gradient, and all are valid solutions corresponding to different values of base pressure. These can be obtained experimentally by blowing or suction in the recirculation region to change the base pressure. The family for which the pressure drops rapidly corresponds to cases in which the wall curvature is increased just downstream of where the solution is terminated. The pressure drop corresponds to the upstream influence of this change in wall curvature, and can be obtained experimentally by truncating the rounded afterbody and rounding the newly created sharp corner.

In Figure 53, the solution best fitting the experimental pressure distribution after the separation process has been initiated has been

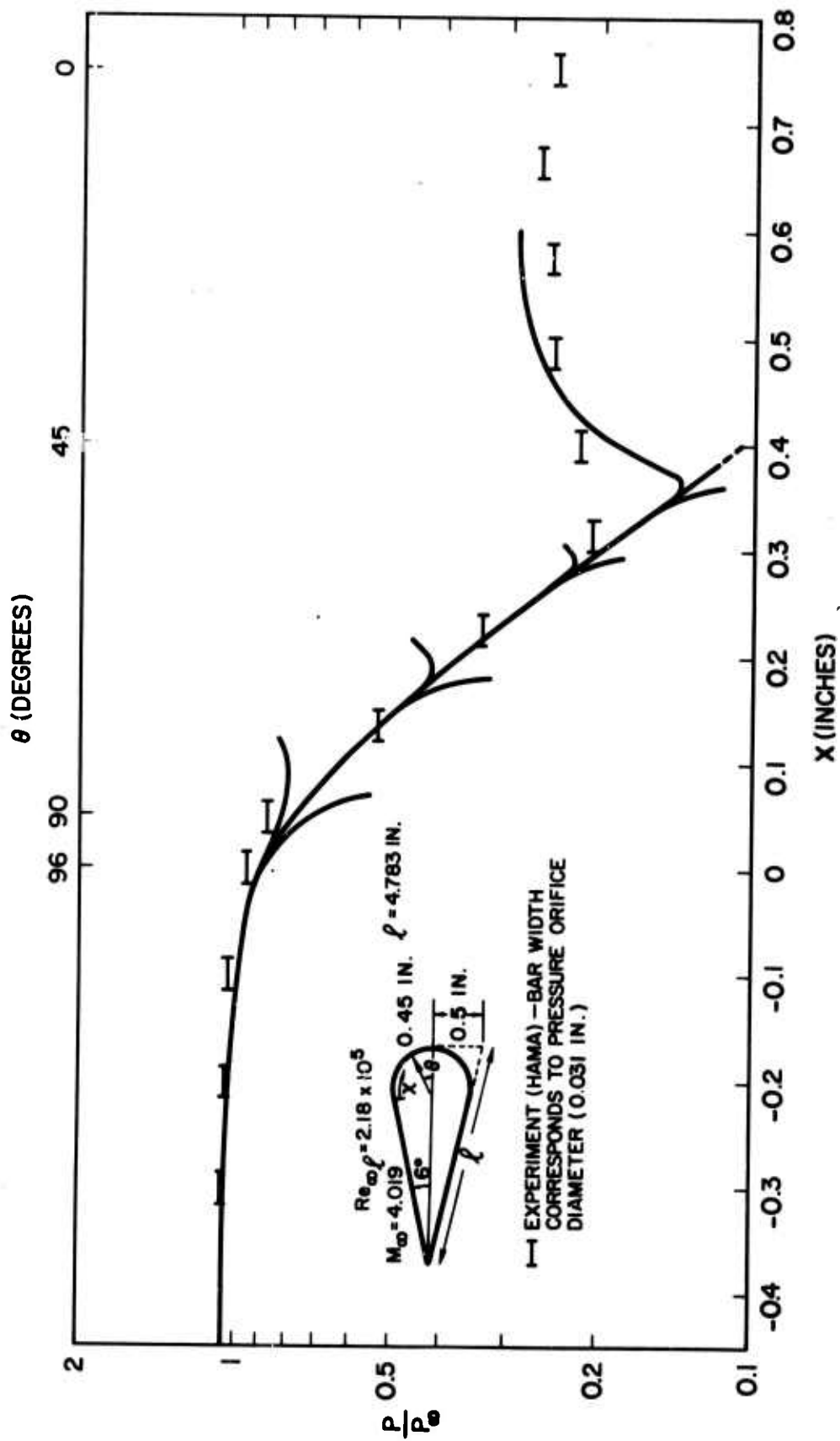


Figure 53. Comparison With Experiment of the Computed Pressure Distribution on a Rounded Backward Facing Step

carried out to the separation point itself. The detailed flow field corresponding to this calculation is shown in Figure 54, and the point which is immediately apparent is that the calculation produces a separation (or lip) shock deeply imbedded in the boundary layer. In Figure 53, the computed separation shock location and streamlines are superimposed over a shadowgraph corresponding to the same flow conditions. The agreement is striking.

A further examination of Figure 54 shows that viscous effects are important out to about that streamline which is initially at Mach 1. This immediately suggests a simplified model in which the supersonic boundary layer is expanded inviscidly around the body, say by using the method of characteristics. Unfortunately, however, an examination of the shape of the streamline initially at Mach 1 discloses that there is no obvious relation between its shape and that of the wall. A calculation assuming that this streamline follows the shape of the wall results in pressures which are far below those measured. It therefore appears that such a simplified model is inadequate.

In Figure 55, the computed pressure distribution on a sharp cornered wedge is compared with experimental values for three flow conditions, again with strikingly good agreement.

### 6.3 DOWNSTREAM EFFECTS OF UPSTREAM INFLUENCE

There is another important aspect of the corner flow problem which was discovered as the result of calculations using an overly simplified model of the corner expansion. The model was proposed by Weinbaum (Reference 48), and assumes that the supersonic boundary layer undergoes an inviscid centered expansion at the body corner from the body surface pressure to the base pressure. Such a model ignores the upstream influence of the base pressure on the boundary layer. Calculations of this type were performed at TRW using the method of rotational-characteristics (Reference 49) with initial conditions which were consistent with experiments conducted by Batt (Reference 50) on a 20-degree wedge at a free stream Mach number of 6. Batt was able to resolve all of the details of the flow (static and total pressure and temperature, streamline orientation, and velocity distribution) in the near wake beginning just downstream of the corner. Some of his results are shown in Figure 56.

$$Re = 1.7 \times 10^5$$

$$M = 4.019$$

$$KL = 8.155 \text{ FOR } S/L > 0.12$$

$$\Psi = \int_0^Y \frac{p u}{\rho u_\infty} d\left(\frac{Y}{L}\right)$$

$$K = 1/r$$

STREAMLINE	$\Psi$	$u/u_\infty$ AT $X/L = 0.09$
a	$1.023 \times 10^{-4}$	0.168
b	$4.152 \times 10^{-4}$	0.331
c	$9.601 \times 10^{-4}$	0.491
d	$1.906 \times 10^{-3}$	0.661
e	$3.474 \times 10^{-3}$	0.835
f	$6.543 \times 10^{-3}$	0.968
g	$1.065 \times 10^{-2}$	0.998

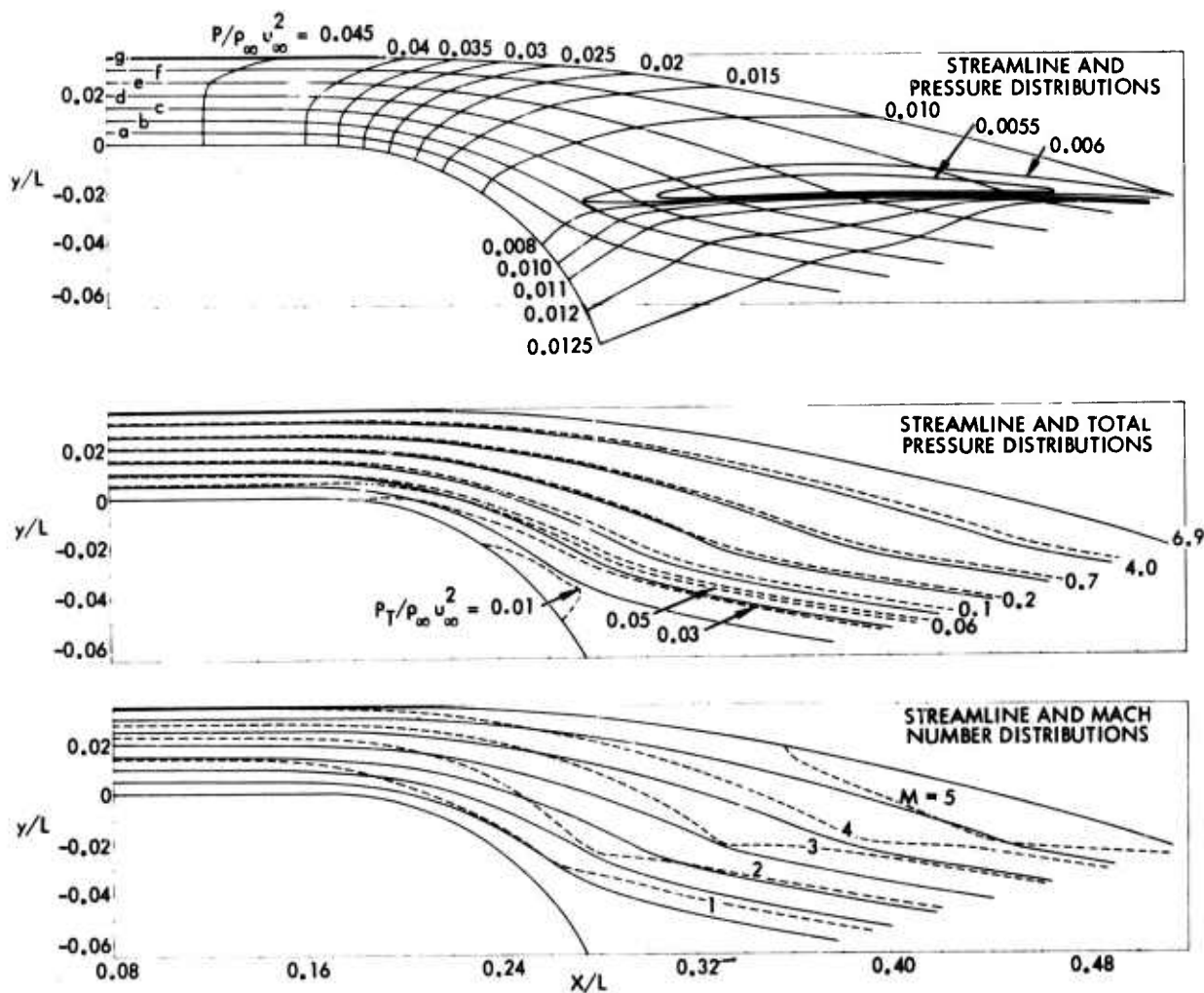
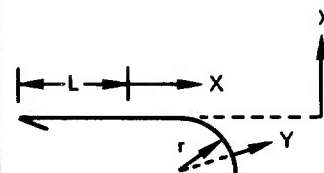


Figure 54. Detailed Flow Properties for a Boundary Layer Separating from a Rounded Backward Facing Step

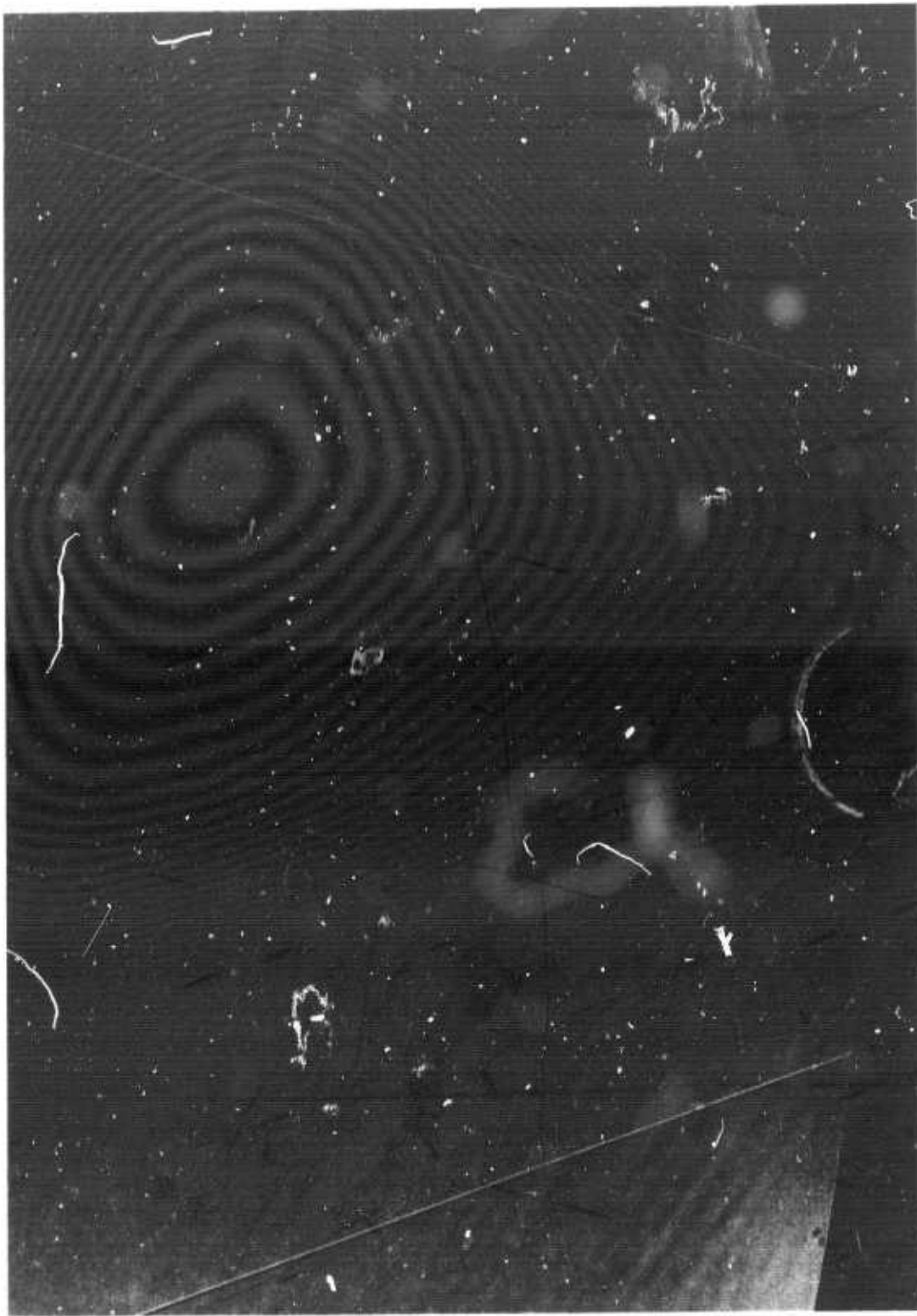


Figure 55. Computed Streamlines and Separation  
Shock Superimposed on Shadowgraph  
Corresponding to the Same Conditions

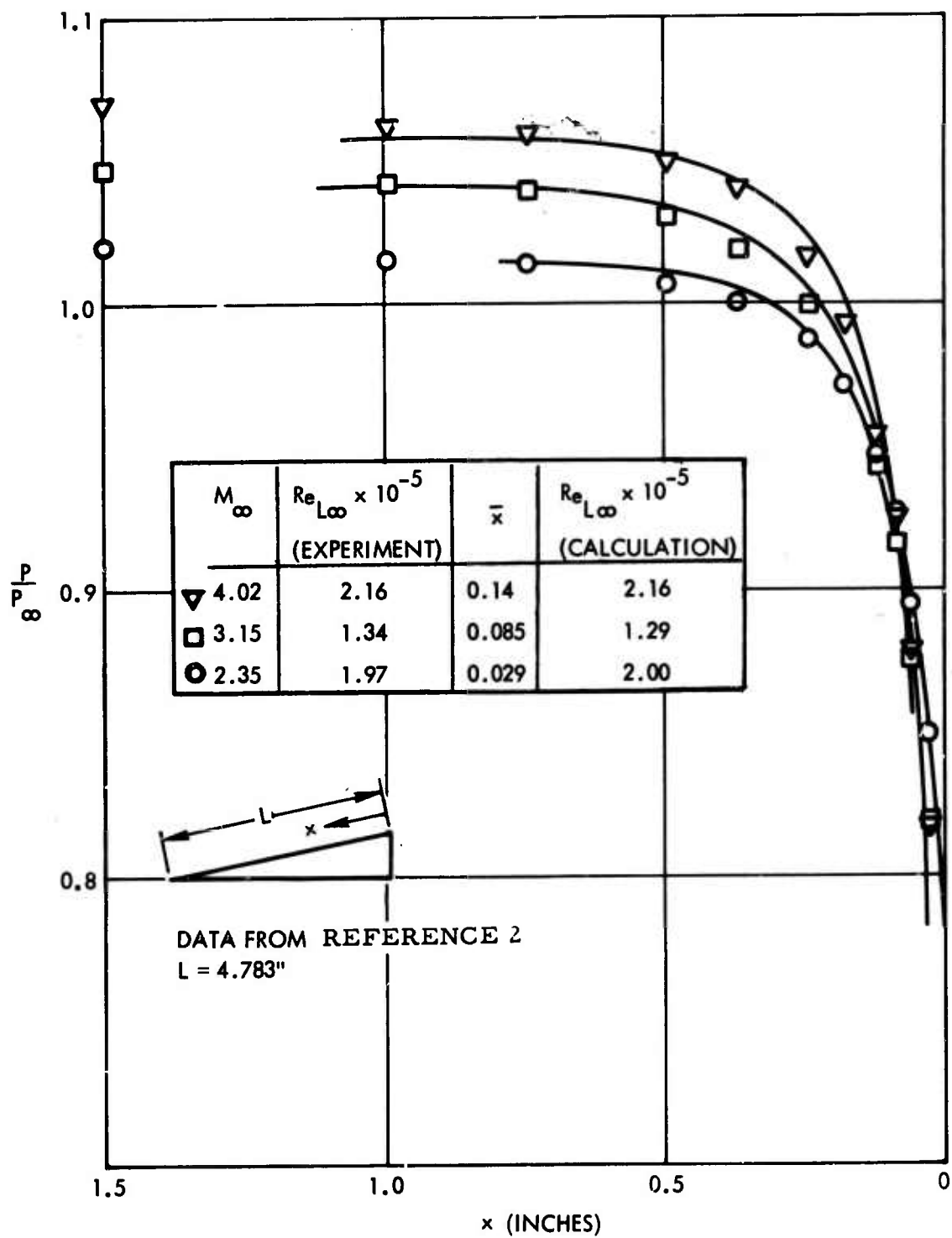


Figure 56. Wall Pressure Near a Sharp Corner-Comparison of Theory with Experiment

Comparisons of the characteristics calculation with the experiment over a distance of several base heights downstream of the corner were made, and the results indicated that the centered expansion grossly overpredicts (by a flow angle of as much as 10 degrees) the streamline orientation in the inviscid region of the flow where the expansion waves from the corner have an influence. In Figure 57, this inviscid region lies above the dotted line at approximately  $1/2$  of the total base height ( $Y/H \approx 0.5$ ) above the  $X/H$  axis. This line represents the locus of points where the change in total pressure along streamlines, hence viscous dissipation, becomes important. In order to obtain good agreement with the experimental data, it was necessary to disregard the model employing the centered expansion, and in its place consider a non-centered expansion beginning upstream of the corner. In the latter calculation, the streamline geometry forming the inner boundary of the inviscid flow to be calculated is specified as a smooth curve, rather than a straight line with a discontinuous slope near the corner (as in the centered-expansion case). The non-centered expansion reflects the upstream influence of the base pressure on the boundary layer structure before the corner, and also demonstrates how this, in turn, has an important effect on the downstream flow entering the viscous near wake.

#### 6.4 INVISCID FLOW ASSUMPTION

Downstream of the separation point on the body, an analytical model of the near wake was formulated at TRW under the assumption that viscous forces are important in the recirculation region, in a narrow shear layer adjacent to the dividing streamline, and below the wake shock wave. The flow above these regions (see Figure 52) was assumed to be expanding inviscidly; the rationale for this is that the vorticity, which was initially very large in the boundary layer, would be significantly and rapidly decreased during the expansion to the point where viscous dissipation would be unimportant. As a result, a method-of-characteristics program was written (Reference 49) for rotational flow which included the capability of calculating imbedded shock waves. An example showing the right running characteristics describing the expansion of the boundary layer into the near wake is presented in Figure 58. A lip shock is shown,





Figure 57. Experimentally Determined Flow Field  
in the Near Wake of a 20-degree Wedge;  
 $M_\infty = 6$ ,  $Re_{\infty H} = 5.5 \times 10^4$  (Reference 5)

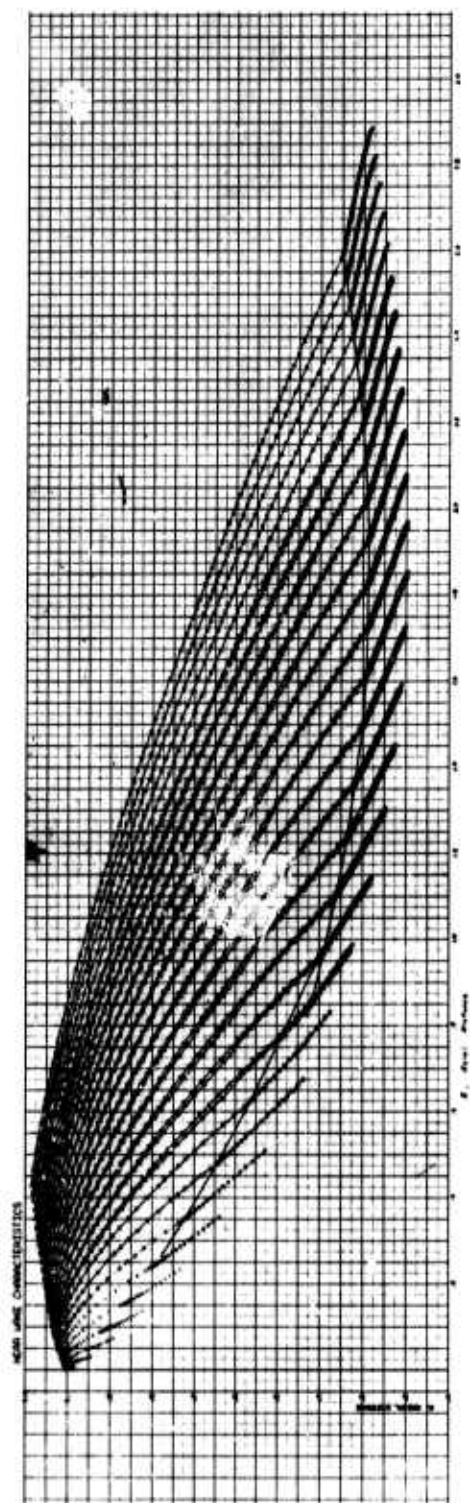


**Figure 58.** Example of a Calculation of the Expansion of the Boundary Layer into the Near Wake by Rotational Characteristics

and a wake shock results as a consequence of an imposed pressure rise along the inner boundary of the calculated region.

With the very recent experimental data of Batt, it has been possible to assess the validity of the assumption that the flow is expanding inviscidly. It was stated earlier that rotational characteristics calculations were performed with initial conditions which were consistent with one of Batt's cases. By adjusting the curvature of the bounding streamline upstream of the body corner all flow properties at a level of a base height agreed with the experiment. The shape of the inner edge streamline after the corner was made to agree with the experiment; and the flow field below a base height, and above where the wake shock would be, was calculated. The result is presented in Figure 59, where the right running characteristics are given and two isobars are shown; the upper one corresponds to the base pressure and the lower one to half the base pressure. The pressure curve shown below the characteristics represents the calculated pressure along the specified streamline boundary and, when this ends, along the non-streamline boundary which is the left running characteristic lying just above the wake shock (not shown). It is seen that the pressure has dropped to a third of the base pressure at the end of the calculation. Thus, the flow in the region of interest is expanding and this, unfortunately, is contrary to the experimental data. The Batt data (Reference 50) shows that the pressure is constant and equal to the base pressure in this region, and that there are significant total pressure losses on streamlines. It appears, short of questioning the data, that the disagreement can only be explained by the viscous effects which are evident from the data.

The experimental data suggests that the viscous near wake below a base radius divides itself into two regions in which pressure forces take on different relative importance. Above the wake shock the balance is between shear and inertia forces whereas the region below the shock is where the primary viscous interaction, and hence, pressure rise occurs. Evidently, the two regions are mutually coupled. Clearly, conditions above the shock affect those below it since the flow progresses in that direction. On the other hand, the presence of strong viscous dissipation in the upper region suggests that shearing stresses are being transmitted

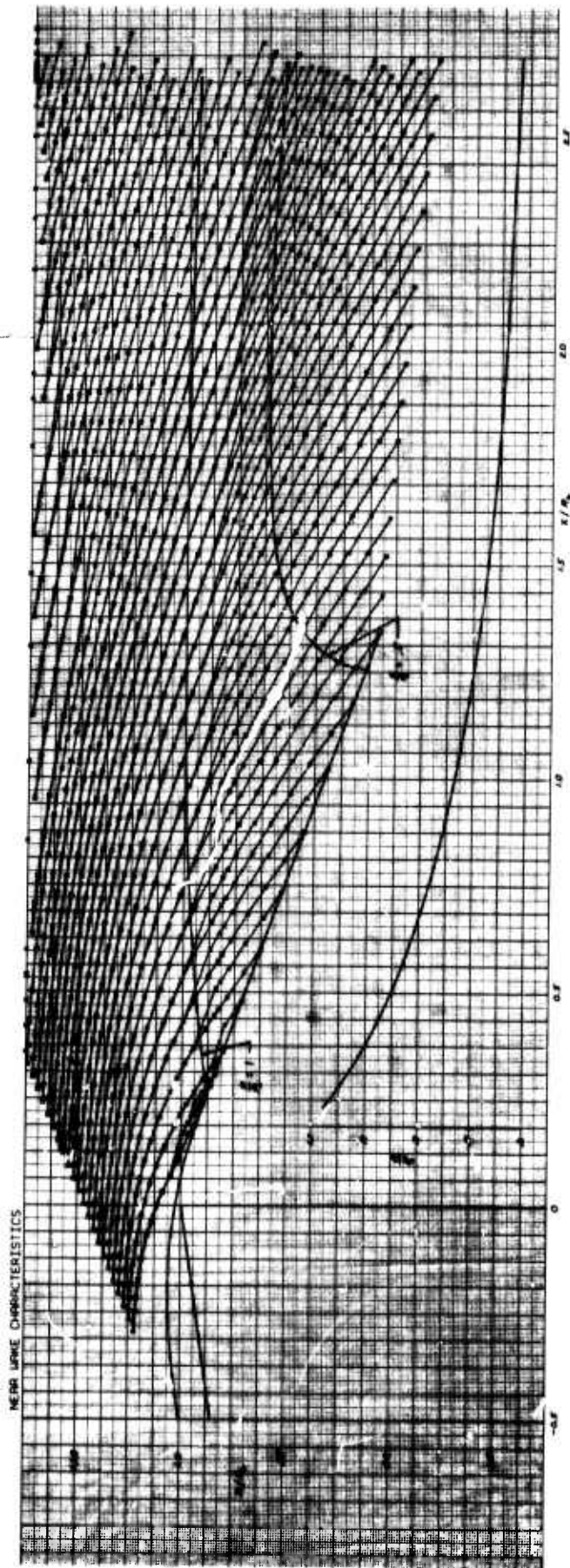


Figure 59. Pressure Field in the Near Wake of a 20-degree Wedge at  $M_\infty = 6$  Calculated by Rotational Characteristics  
Note: Pressures are normalized with the base pressure.

across the shock (probably, in a direction tangential to it). Thus, the basic fluid physics of the near wake differs from that assumed with the inviscid flow model above the wake shock. In that model, the balance is between pressure and inertia forces, and the flow above the shock is influenced by left running characteristics which originate from the edge of the shear layer above the dividing streamline within close proximity to the base, and right running characteristics which emanate from the flow above the corner. However, the experimental results show that this is fundamentally in error. Pressure forces are not important above the shock, and the flow there is strongly influenced by the flow below the shock. It will be shown later that the solution to the interacting near wake is very sensitive to the flow conditions above the shock, and hence, that accurate determination of the flow in this region is very important to the overall wake problem. It must be concluded that attempts at a near wake solution which employ the inviscid model, such as the partial solutions of Weiss (Reference 51), are therefore of questionable validity.

## 6.5 WAKE NECK

The flow downstream of the wake stagnation point has been studied in some detail at TRW and is relatively well understood. A flow model coupling a boundary-layer-like region near the axis to an inviscid outer region using a displacement interaction was first investigated by Webb, Golik, Lees, and Vogenitz (References 52, 53). They found that for any one parameter family of initial profiles, the solution downstream could be divided into two families, with a particular solution forming the boundary of these two families and proceeding downstream through a saddle point type of singularity. Only the particular solution was found to have the downstream behavior appropriate to a far wake and, since the parameter describing the initial profile shapes could be related to the base pressure, this introduces a required uniqueness condition which determines the base pressure.

This behavior is not at all surprising, since there are other well-known examples of problems having qualitatively similar solutions. For instance, the one dimensional nozzle problem is hyperbolic when the time dependent term is retained and the steady state solution is the asymptotic limit for large time. Whether one finds a supersonic or

subsonic solution depends on the imposed boundary condition at the nozzle exit. However, when one searches for a solution to the steady state equations, it is found that this becomes a problem with parabolic character, with all possible downstream conditions obtainable by varying an otherwise undetermined initial condition. There is a whole family of subsonic solutions, but the supersonic solution is unique and determined by a saddle-point type singularity. If we start with the knowledge that the downstream flow is supersonic, then, in either the wake or nozzle problem the only solution of interest is the singular one.

The mathematical nature of the singularity in the wake problem as formulated by Webb et al. has been studied in great detail by Ai (Reference 54) at TRW.

Baum and Denison (Reference 55) extended the interacting wake model to include transverse pressure gradients in the supersonic region with, of course, no qualitative change in the results. This model (in which the equations are solved by finite differences) and the Webb et al. model (which uses integral methods) have both been coupled (by Ohrenberger, Reference 56) at the outer edge to a rotational characteristics calculation (Reference 49) which includes provisions for internally generated shocks. It was originally expected that the rotational characteristics - viscous wake model would suffice as an acceptable model of the near wake. However, as previously discussed, recent experimental data suggest that viscous effects are not negligible in a region lying above the wake shock and within the region for which we have used an inviscid flow model. Nevertheless it is possible to use this model in a restricted way, and in conjunction with known experimental results, to investigate the sensitivity of the wake neck solution to the flow above the shock. In addition, comparisons can be made with experiment.

Rather than employing rotational characteristics to calculate the entire expansion of the boundary layer into the near wake, the approach is to apply the method to a narrow region adjacent to both sides of the wake shock wave. The fact that viscous dissipation is present above the wake shock is then reflected in the boundary conditions imposed on the upstream side of the inviscid region. The assumption is that although the integrated viscous dissipation is important for the entire expansion



process, the amount during a short traverse of the streamlines is small. Batt's experimental results bear this out since the divergence between streamlines (long dashed lines in Figure 57) and lines of constant total pressure (short dashed lines in Figure 57) from the boundary layer to wake shock wave is large, whereas the local divergence is relatively small.

The approach to the present calculations is more easily explained by referring to Figure 60. From the experimental data, the necessary flow parameters are specified along a left running characteristic which lies just above the wake shock wave. The viscous model is restricted to calculating the flow downstream of the wake stagnation point. However, part of the interaction, and hence pressure rise, occurs forward of this point. This is accounted for by specifying from the data, the pressure distribution upstream of the wake stagnation point on that streamline which enters what the model considers to be the edge of the viscous wake at the station of the wake stagnation point. Only one other condition remains and that is specification of the velocity profile at the wake stagnation point. The chosen profile must reflect the correct mass balance consistent with the data. The downstream interaction is then calculated as an eigenvalue problem with the value of Reynolds number as the unknown quantity. Results are shown in Figures 61 and 62 where the two families of non-wake-like solutions discussed previously are shown. The Reynolds number of the case in Figure 61 is smaller than that in Figure 62; the lower Reynolds number case ( $Re_{\omega H} = 50,000$ ) shows a source type solution (the centerline velocity eventually decreases downstream) which would yield a second stagnation point downstream of the wake stagnation point. Figure 61, representing the same flow at a higher Reynolds number ( $Re_{\omega H} = 55,000$ ), shows the sink type solution in which the pressure begins to decrease along the axis. The solution Reynolds number is therefore bracketed by these two cases. The Reynolds number corresponding to the experimental case is 55,000 and so the agreement is quite favorable. It is also of interest to compare the calculated pressure distribution along the axis with the data. This is done in Figure 63 and shows that the calculated distribution is generally on the high side of the experimental data but is nonetheless acceptable.



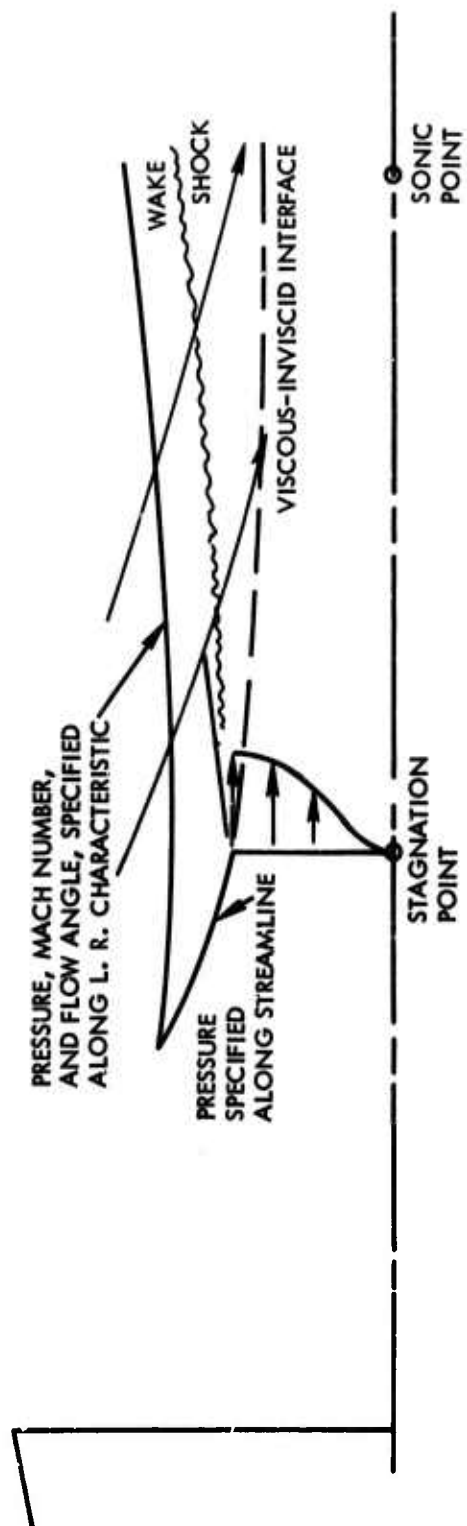
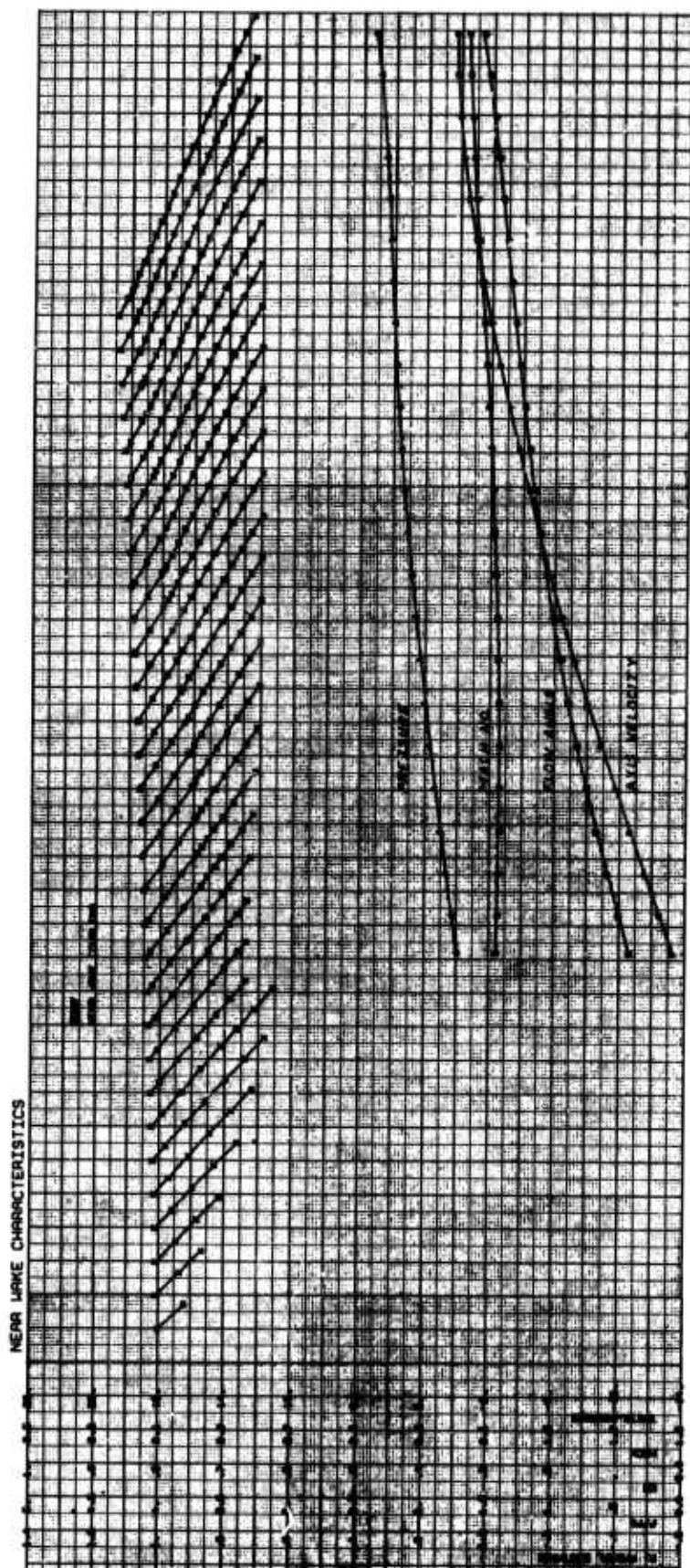


Figure 60. Wake Neck Interaction Analysis



**Figure 6l. Interacting Wake Neck Calculation Showing a Source Type Solution ( $Re_{\infty H} = 50,000$ )**

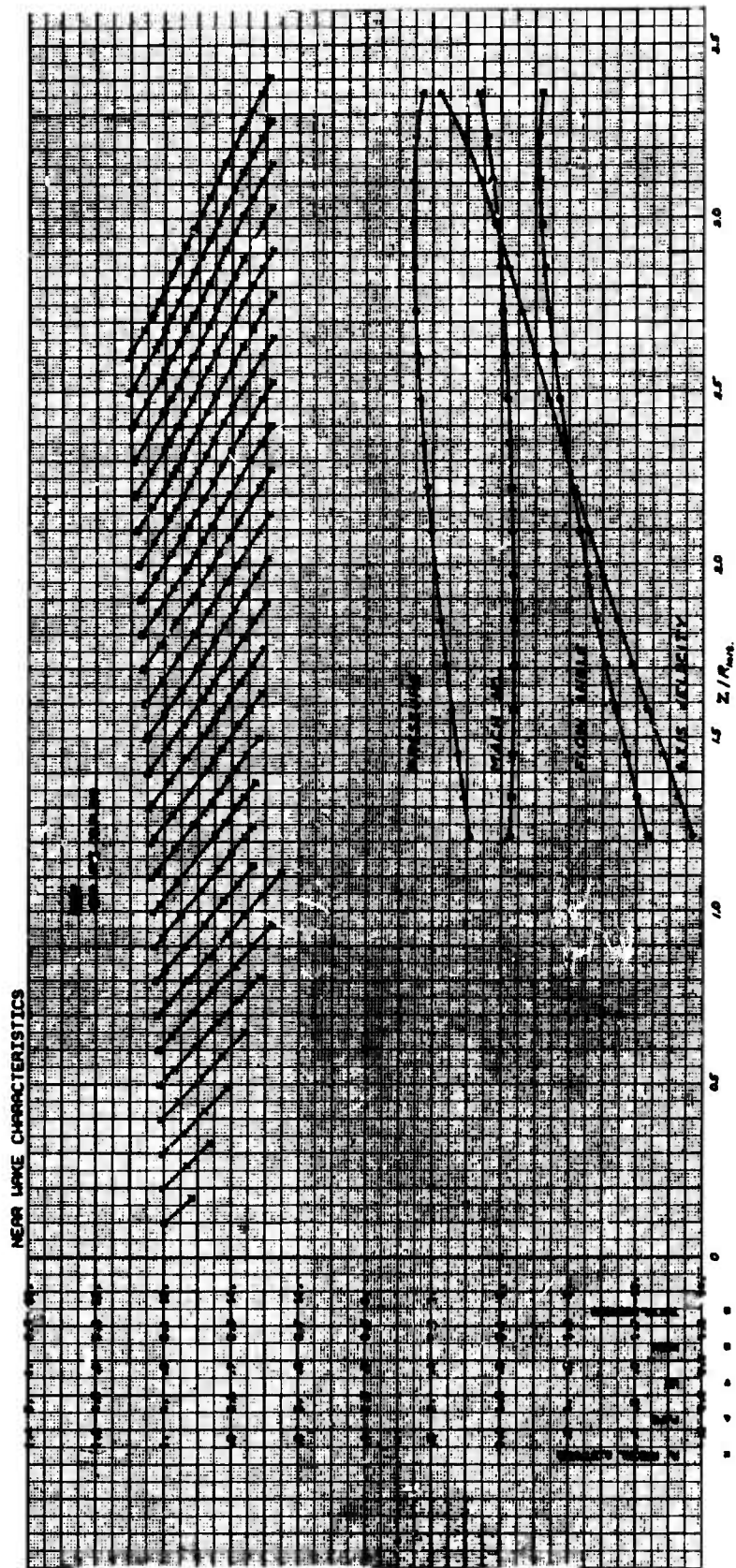


Figure 62. Interacting Wake Neck Calculation Showing a Sink  
Type Solution ( $Re_{\infty H} = 55,000$ )

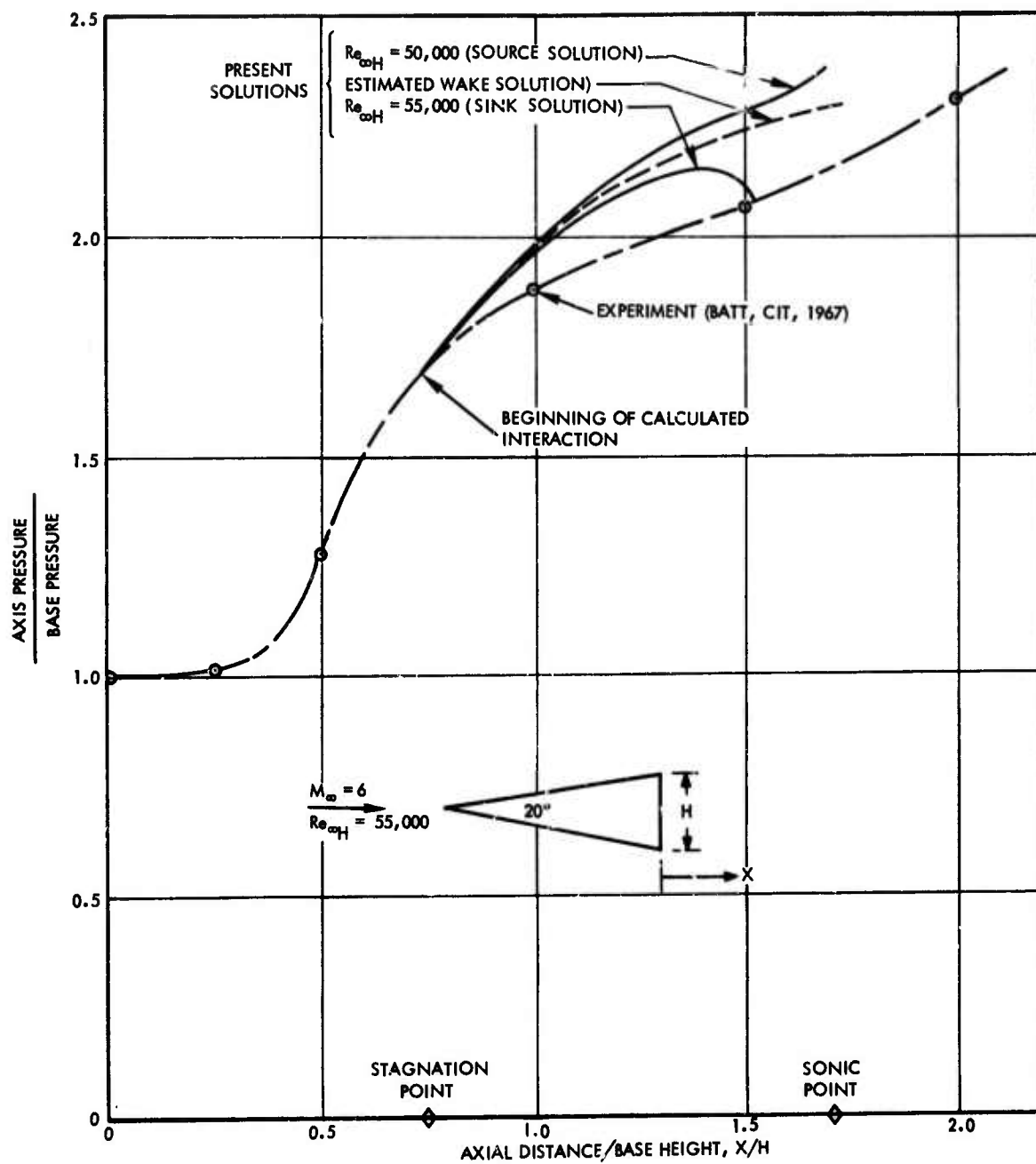


Figure 63. Results of Wake Neck Interaction and Comparison with Experiment

Another point of interest is the sensitivity of the solution to the input flow parameters. There is some flexibility in the specification of the input data due to the uncertainties in the experimental data. This is particularly true along the left running characteristic above the wake shock. Three cases were considered and the input and results are summarized in Figure 64. The best agreement with experiment is for Case I which has already been presented. The flow angle distribution for Case II is the same as for Case I but the Mach number although initially the same was increased to a maximum of about 8 percent. The input left running characteristic is thereby inclined at a somewhat smaller angle to the horizontal. The perturbation in Mach number led to a solution Reynolds which lies between  $43$  and  $50 \times 10^3$  which is slightly lower than that found in Case I. The axis pressure is also higher and has diverged significantly from the experimental values (the solution pressure distribution is bracketed by the curves shown). For Case III the flow angle was decreased 2.5 degrees and the Mach number decreased by a maximum of 4 percent. The left running characteristic is approximately horizontal. The solution Reynolds number lies between  $32$  and  $38 \times 10^3$  which is in considerable disagreement with the experimental value of 55,000. The axis pressure is seen to rise much too steeply compared to experiment. These results demonstrate that the solution is very sensitive to the flow above the shock wave. Changes in Mach number of a few percent and in flow angle of 2.5 degrees have a dramatic effect on the solution. As previously stated, it has become apparent that an accurate description of the flow above the wake shock is required if meaningful near wake solutions are to be obtained.

## 6.6 RECIRCULATION REGION

Recent theoretical investigations of the flow in the recirculation region have been concerned with finding exact numerical or approximate series solutions to the Navier-Stokes equations. The major objection to these analyses lies with their use as a component part of an overall analysis of the near wake, and not as a description of the recirculation region itself. In the overall near wake or "coupled" problem, the flow adjacent to the recirculation region may be described by a set of parabolic differential equations which would normally be solved using a forward

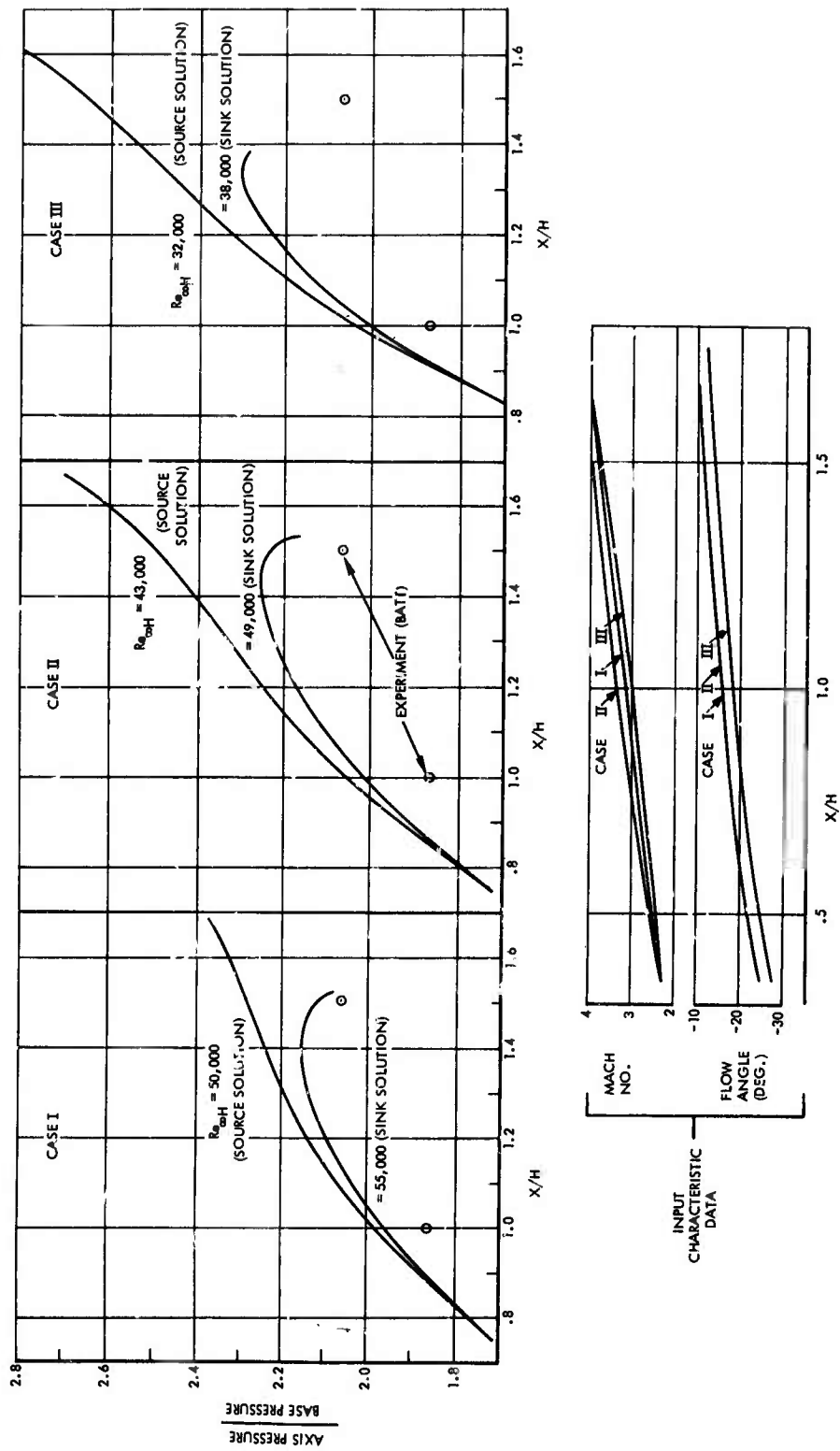


Figure 64. Sensitivity of Wake Neck Solution to the Flow Above the Wake Shock



marching scheme. However, obtaining an exact numerical solution for the recirculation region is an elliptic problem and this fact precludes the use of marching methods. It is therefore not possible to simultaneously calculate the inner recirculating and outer shear flows. In this method the numerical procedure must involve a guess of the boundary conditions for the elliptic region followed by a calculation of the external parabolic flow. Successive guesses or iterations are required until the unmatched flow properties along the entire boundary between the two regions agree to within some desired accuracy. Whether an acceptable convergence of the flow properties along the entire dividing streamline can be achieved is questionable. Certainly, such a scheme is very inefficient from the standpoint of computer time. This is further compounded when a solution to the overall near wake problem is sought since the iteration described above is subordinate to the iteration for the flow which proceeds through the critical point.

Recently, a simplified analysis of the recirculation region was presented by Reeves and Buss (Reference 57) in which the streamfunction was described by a double series expansion in the axial and lateral co-ordinate about the wake stagnation point truncated by terms of the fifth power. Relations between the coefficients of the series were found by satisfying the boundary conditions and the Navier-Stokes equations. However, it remained that several of the coefficients must be specified. A study of the use of this method for the recirculation region in the overall near wake problem revealed that it suffers from the same matching difficulties as in the numerical case. That is, guesses must be made for the unknown coefficients followed by a calculation of the outer parabolic flow. This is repeated until agreement of the unmatched flow properties occurs on the boundary between the inner and outer regions. The questions of convergence and excessive computer time again arise.

What is needed is a simple analysis of the recirculation region which is compatible with the marching scheme for the outer shear flow and which does not require sub-iterations for matching the flow properties on the dividing streamline. Such an analysis was initiated during the present study.



The present approach employs integral methods applied to the Navier-Stokes equations. The nature of the mathematical problem is thereby changed from elliptic to initial valued, thus permitting the use of marching methods in conjunction with the external flow. In addition, a simultaneous matching of the conditions (flow direction, velocity, shear, and pressure) on the dividing streamline with the external shear flow may be accomplished. In this approach the only iterations required in the overall near wake problem will be on the parameter which dictates whether the flow proceeds through the critical point downstream of the wake stagnation point.

To facilitate use of the integral method, several important assumptions are made. The first has to do with the form of the stream-function, which in an integral method, must be specified. It was noted in the analysis by Reeves and Buss that a streamline pattern characteristic of the recirculation region can be described by a polynomial of relatively low order. In particular, a fifth order polynomial of odd powers in the lateral co-ordinate was sufficient. Exploiting this result for the integral analysis leads to the following form for  $\psi$ :

$$\psi(x, \eta) = \psi_1(x) \eta + \psi_2(x) \eta^3 + \psi_3(x) \eta^5$$

where  $\eta$  is a dimensionless lateral co-ordinate  $y/\delta(x)$ , and  $\delta(x)$  is the height of the dividing streamline from the x-axis. The functions  $\delta(x)$ ,  $\psi_1(x)$ ,  $\psi_2(x)$ , and  $\psi_3(x)$  are unknown dependent variables in the integral method.\* Since  $\psi(x, \eta)$  is zero when  $\eta$  is unity for all  $x$ , it follows that

$$\psi_3(x) = -\psi_1(x) - \psi_2(x)$$

and the number of dependent variables are thereby reduced by one. Also,  $\psi_1(x)$  and  $\psi_2(x)$  can be represented in terms of  $\delta(x)$ , the centerline velocity,  $u_0(x)$ , and the horizontal component of velocity on the

---

\*In the approach of Reeves and Buss,  $\psi_1$ ,  $\psi_2$ , and  $\psi_3$  are truncated series expansions in  $x$  with undetermined coefficients, and  $\eta$  is the lateral co-ordinate  $y$ .

dividing streamline,  $u_\delta(x)$ , and can take on more physical meaning as follows:

$$\psi_1(x) = \delta(x) u_0(x)$$

and

$$\psi_2(x) = -2\delta(x) u_0(x) - \frac{1}{2} \delta(x) u_\delta(x)$$

With this representation the dependent variables are  $u_0(x)$ ,  $u_\delta(x)$ , and  $\delta(x)$ .

The governing equations for the three unknown variables are obtained by integrating the x-momentum equation (Navier-Stokes), and a moment of this equation across the recirculation region. The additional equation is given by matching the shear on the dividing streamline with that from the outer flow. However, in the absence of the actual coupling, the external shear must be a specified function of the axial co-ordinate. The other flow quantities on the dividing streamline (pressure, velocity, and direction) are matched as a consequence of specifying the boundary conditions on the external shear flow in the coupled case.

The final assumption to be imposed is that the pressure is independent of the lateral co-ordinate across the recirculation region, i. e.,  $p = p(x)$ . From the Reeves and Buss solutions at the higher Reynolds numbers, this appears to be a good assumption away from the base. A significant lateral pressure variation does appear on and near the base; however, it may be shown that the average value of  $\partial p / \partial x$  (which appears in the integral equations) across the recirculation region is very small and is, in fact, exactly zero on the base. Consequently, the average axial pressure gradient term will be ignored, initially; and the lateral pressure field near the base will be calculated using the y-momentum equation once the solution for  $\psi$  is known.

The governing equations have been developed and the nature of the near base solution investigated by a series expansion. At this point, the method remains promising and, hopefully, will be continued at a later date.

## 6.7 CONCLUSIONS AND RECOMMENDATIONS

A number of phenomena have been identified in the current contract period as being of critical importance in determining the near wake flow field. These include two major effects:

- 1) the upstream influence of the low base pressure on the boundary layer approaching the separation point strongly affects the flow field far downstream;
- 2) viscous effects cannot be neglected external to the lip and wake shocks.

A method of calculating the boundary layer flow approaching separation has been developed, including the upstream influence and the lip or separation shock imbedded deeply within the boundary layer. The agreement with experiment of the computed wall pressure distribution near separation and the separation shock location was excellent. It is felt that the phenomena important in determining the near wake flow field are now recognized, and the tools for incorporating them into a theoretical model have been developed. The most important problem to be attacked in the near future is, then, to tie together the near wake regions into a complete theoretical near wake model incorporating all of the effects which we now recognize to be important. With this in mind, the investigation of a simplified method of computing the recirculation region, suitable for incorporation into a complete near wake computation scheme, has been initiated and is continuing.

## REFERENCES

1. Bird, G. A. , "Approach to Translational Equilibrium in a Rigid Sphere Gas", Physics of Fluids 6, 1518-1519, 1963.
2. Bird, G. A. , "Shock Wave Structure in a Rigid Sphere Gas" Rarefied Gas Dynamics, Supplement 3, (J. H. DeLeeuw, ed.) Vol. I, 1965.
3. Bird, G. A. , "Aerodynamics Properties of Some Simple Bodies in the Hypersonic Transition Regime" AIAA J. Vol. 4, No. 1, Jan. 1966.
4. Broadwell, J. E. , and Rungaldier, H. , "Structure of the Shock Layer on Cylinders in Rarefied Gas Flow", Rarefied Gas Dynamics, Supplement 4, Vol. II, 1967. (C. L. Brundin, Ed.)
5. Broadwell, J. E. & Rungaldier, H. , "Shock Layer Structure on Cylinders, Spheres and Wedges in Low Density Supersonic Flow", TRW Systems Report No. 66-3320. 4-10, Dec. 1966.
6. Vogenitz, F. W. , Bird, G. A. , Broadwell, J. E. , and Rungaldier, H. , "Theoretical and Experimental Study of Rarefied Supersonic Flow About Several Simple Shapes", TRW Report No. 07354-6082-R000 (to be published).
7. Willis, D. R. , "A Study of Some Nearly Free Molecular Flow Problems", Ph. D. Thesis, Princeton University (1959).
8. Maslach, G. J. , "Supplementary Cylinder Drag Data for Transition Flow Conditions", Univ. of Calif. IER Report No. AS-63-3 Berkeley, Calif. July 1963.
9. Aroesty, J. , "Sphere Drag in a Low Density Supersonic Flow" IER Report HE-150-192, University of California, Jan. 1962.
10. Wegener, P. P. , and Ashkenas, H. , "Measurement of Sphere Drag at Supersonic Speeds", JFM, Vol. 10, Part 4, pg. 550, June 1961.
11. Liepmann, H. W. ; Narasimha, R. , and Chahine, M. , "Theoretical and Experimental Aspects of the Shock Structure Problem" Proc. of 11th Int'l Congress of Applied Mechanics, Munich, 1964.
12. Kahn, H. "Multiple Quadrature by Monte Carlo Methods", in Mathematical Methods for Digital Computers, Ralston, A. , and Wilf, H. S. , Wiley and Sons, N. Y. , 1960.
13. Sherman, F. S. , "A Low Density Wind Tunnel Study of Shock Wave Structure and Relaxation Phenomena in Gases", Univ. of Calif. IER Report No. H. E. -150-122, Berkeley, California, May 1954.

14. Russell, D., "Electron Beam Density Measurements on Stagnation Line of a Sphere", JPL (to be published). (approximate title)
15. Wang, C. J., Peterson, J. B., and Anderson, R., "Gas Flow Tables", Space Technology Laboratories Inc. Report GM-TR-154, March 1957.
16. Hilsenrath, J., et. al. "Tables of Thermal Properties of Gases", NBS Circular 564, November 1955.
17. Potter, J. L., "The Transitional Rarefied-Flow Regime", in Rarefied Gas Dynamics (C. L. Brundin, ed.), Vol. 2, pp. 881 - 938, Academic Press Inc., New York (1967).
18. Liepmann, H. W., Narasimha, R., and Chahine, M. T., "Structure of a Plane Shock Layer", Physics of Fluids, Vol. 5, No. 11, pp. 1313 - 1324, 1962.
19. Fox, J., Webb, W. H., Jones, B. G., and Hammitt, A. G., "Hot-Wire Measurements of Wake Turbulence in a Ballistic Range," AIAA Journal, Vol. 5, pp. 99-102, 1967.
20. Lees, L., and Hromas, L., "Turbulent Diffusion in the Wake of a Blunt Nosed Body at Hypersonic Speeds," Journal of Aerospace Sciences, Vol. 29, pp. 976-993, 1962.
21. Webb, W. H., and Hromas, L., "Turbulent Diffusion of a Reacting Wake," AIAA Journal, Vol. 3, pp. 826-837, 1965.
22. Webb, W. H., "A Model for the Calculation of Radar Backscatter from Underdense Hypersonic Turbulent Wakes," TRW Report 6433-6005-KU000, June 8, 1964. Also see Webb, W. H., "Self-Preserving Fluctuations and Scales for the Hypersonic Turbulent Wake," AIAA Journal, Vol. 2, pp. 2031-2033, 1964.
23. Clay, W. G., Herrmann, J., and Slattery, R. E., "Statistical Properties of the Turbulent Wake behind Hypervelocity Spheres," Phys. Fluids, Vol. 8, pp. 1792-1801, 1965.
24. Lien, H., and Eckerman, J., "Interferometric Analysis of Density Fluctuations in Hypersonic Turbulent Wakes," AIAA Journal, Vol. 4, pp. 1988-1994, 1966.
25. Townsend, A. A., The Structure of Turbulent Shear Flow, Cambridge University Press, London, 1956.
26. Demetriades, A., "Turbulence Measurements in an Axisymmetric Compressible Wake," Philco-Ford Corp., Report No. UG-4118, August 1, 1967.
27. Gibson, C. H., Chen, C. C., and Lin, S. C., "Measurements of Turbulent Velocity and Temperature Fluctuations in the Wake of a Sphere," AIAA Paper No. 67-20, 5th Aerospace Sciences Meeting, New York, 1967.

28. Lin, S. C. and Teare, J. Derek, "Rate of Ionization behind Shock Waves in Air, II -- Theoretical Interpretations," *The Physics of Fluids*, Vol. 6, No. 3, pp. 355-375, March 1963.
29. Davies, W. O., "Carbon Dioxide Dissociation at 3500° to 6000°K," *The Journal of Chemical Physics*, Vol. 41, No. 6, pp. 1846-1852, September 1964.
30. Sulzmann, K. G. P., Myers, B. F., and Bartle, E. R., "CO Oxidation, I -- Induction Period Preceding CO<sub>2</sub> Formation in Shock Heated CO-O<sub>2</sub>-AR Mixtures," *Journal of Chemical Physics*, Vol. 42, No. 4, pp. 3969-3979, June 1965.
31. Avramenko, L. I. and Kilesnikova, R. V., *Bulletin of the Academy of Sciences of the U.S.S.R., Division of Chemical Science*, p. 1562, 1959, (*Izvestiya Akademii NAUK S.S.S.R., Otdelenia Khimicheskikh Nauk*).
32. Walker, P. L., Jr., Rusinko, F., Jr., Austin, L. G., "Gas Reactions of Carbon," *Advances in Catalysis and Related Subjects*, edited by D. D. Eley, et al, Vol. XI, pp. 133-221 Academic Press, Inc., New York, 1956.
33. Blyholder, G., Eyring, H., "Kinetics of Graphite Oxidation, II," *Journal of Physical Chemistry*, Vol. 63, pp. 1004-1008, June 1959.
34. Moore, J. A. and Zlotnick, M., "Combustion of Carbon in an Air Stream," *A.R.S. Journal*, Vol. 31, No. 10, pp. 1388-1397, October 1961.
35. Rubel, A. and Zeiberg, S. L., "Some Effects of Turbulent Fluctuation on Air Ionization Reaction Rates in Hypersonic Wakes," *A.I.A.A. Paper No. 65-819*, December 1965.
36. Kiser, K. M. and Hoelscher, H. E., "Chemical Reactions in a Water Tunnel," *Industrial and Engineering Chemistry*, Vol. 49, No. 6, pp. 970-977, June 1957.
37. Sparks, R. E. and Hoelscher, H. E., "An Experimental Study of Liquid-Phase Turbulent Diffusion," *A.I.Ch.E. Journal*, Vol. 8, No. 1, pp. 103-112, March 1962.
38. Saidel, G. M. and Hoelscher, H. E., "Chemical Reaction in the Turbulent Wake of a Cylinder," *A.I.Ch.E. Journal*, Vol. 11, No. 6, pp. 1058-1063, November 1965.
39. Toor, H. L., "Mass Transfer in Dilute Turbulent and Non-turbulent Systems with Rapid Irreversible Reactions and Equal Diffusivities," *A.I.Ch.E. Journal*, Vol. 8, No. 1, pp. 70-78, March 1962.
40. Hawthorne, W. R., Weddell, D. S. and Hottel, H. C., "Mixing and Combustion in Turbulent Gas Jets," *Third Symposium on Combustion, Flame and Explosion Phenomena*, pp. 266-288, 1949.

41. Keeler, R. N. , "Mixing and Chemical Reactions in Turbulent Flow Reactors," University of California, Lawrence Radiation Laboratory Report No. UCRL-7852, June 1964.
42. Moore, J. A. , "Chemical Non-Equilibrium in Viscous Flows", Ph. D. Thesis, State University of New York at Buffalo, May 1967.
43. Hirschfelder, J. O. , Curtiss, C. F. , and Bird, R. B. , Molecular Theory of Gases and Liquids, Wiley, New York, 1964.
44. Lees, L. and Hromas, L. , "Turbulent Diffusion in the Wake of a Blunt Nosed Body at Hypersonic Speeds", Journal of the Aerospace Sciences, Vol. 29, No. 3, August 1962.
45. Baum, Eric, "An Interaction Model of a Supersonic Laminar Boundary Layer Near a Sharp Backward Facing Step," TRW Report 07854-6019-ROOO, December 1966.
46. Baum, Eric, "An Interaction Model of a Supersonic Laminar Boundary Layer On Sharp and Rounded Backward Facing Steps," TRW Report 07854-6019-R001, July 1967.
47. Hama, Francis R. , "Experimental Investigations of Wedge Base Pressure and Lip Shock," JPL TR 32-1033, December 1966.
48. Weinbaum, S. , "Rapid Expansion of a Supersonic Boundary Layer," AIAA J. 4, 217-226, 1966.
49. Ohrenberger, J. T. , "Near Wake Characteristics Program - Finite Difference and Related Equations," TRW Technical Operating Report 4456-6004-T0-000, 5 October, 1965.
50. Batt, R. C. , "Experimental Investigation of Wakes Behind Two-Dimensional Slender Bodies at  $M = 6$ ," Ph. D. Thesis, California Institute of Technology, June 1967.
51. Weiss, R. F. , "A New Theoretical Solution of the Laminar, Hypersonic Near Wake," AIAA Preprint No. 67-63, 5th Aerospace Sciences Meeting, New York, January 1967.
52. Webb, W. H. , et al, "A Multimoment Integral Theory for the Laminar Supersonic Near Wake," Proceedings of the 1965 Heat Transfer and Fluid Mechanics Institute.
53. Golik, R. J. , Webb, W. H. , and Lees, L. , "Further Results of Viscous Interaction Theory for the Laminar Supersonic Near Wake," AIAA Preprint No. 67-61, 5th Aerospace Sciences Meeting, New York, Jan. 1967.
54. Ai, D. K. , "On the Hypersonic Laminar Near Wake Critical Point of the Crocco-Lees Mixing Theory," AIAA Paper 67-60, presented at 5th Aerospace Sciences Meeting AIAA, January 1967.



55. Baum, E., and Denison, M. R., "Interacting Supersonic Laminar Wake Calculations by a Finite Difference Method," AIAA Journal, July, 1967.
56. Ohrenberger, J. T., "The Flow of the Boundary Layer into the Near Wake by Rotational Characteristics and Comparisons with Experiment," TRW 07854-6089-R000, in preparation.
57. Reeves, B. L. and Buss, H., "On the Flow in Regions of Laminar Separation," AIAA Paper No. 67-64, 5th Aerospace Sciences Meeting, New York, January 1967.
58. Wilson, L. N., "Far Wake Behavior of Hypersonic Spheres," AIAA Journal, Vol. 5, No. 7, July 1967.

## APPENDIX I

The following list of reports have been or shortly will be published in fulfillment of Penetration Systems Studies, Contract AF 04 (694)-992.

1. Baum, Eric, "An Interaction Model of a Supersonic Laminar Boundary Layer Near a Sharp Backward Facing Step," BSD-TR 67-81, 07854-6019-R000, December 1966.
2. Fox, J., "Space Correlation Measurements in the Fluctuating Turbulent Wakes Behind Projectiles," BSD-TR 67-82, TRW 07854-6021-R000, February 1967. This was also presented at the Fifth AIAA Aerospace Sciences Meeting, New York, January 1967, Paper No. 67-19 and will be published in the AIAA Journal.
3. Webb, W. H., "A New Mixing Length Theory for Turbulent Flows in Dynamic Equilibrium," BSD-TR-67-120, TRW 07854-6024-R000, AD 814884, March 1967.
4. Baum, Eric, "An Interaction Model of a Supersonic Laminar Boundary Layer on Sharp and Rounded Backward Facing Steps," BSD-TR 67-181, TRW 07854-6019-R001, July 1967. Also accepted for publication in AIAA Journal.
5. Lewis, J. E., "The Compressible Boundary Layer with Pressure Gradient, Heat Transfer and Mass Transfer and Its Low Speed Equivalent," BSD-TR-67-196, TRW 07854-6065-R000, August 1967.
6. Ai, D. K., "On the Hypersonic Laminar Near Wake Critical Point of the Crocco-Lees Mixing Theory," TRW 07854-6010, R000, June 1967, to be issued. This was also presented at the Fifth AIAA Aerospace Sciences Meeting, New York, January 1967, Paper No. 67-60.
7. Baum, E. and Denison, M. R., "Interacting Supersonic Laminar Wake Calculations by a Finite Difference Method," AIAA Journal, Vol. 5, No. 7, July 1967.
8. Ohrenberger, J. T., "Near Wake Viscous Interaction with a Rotational External Flow," TRW 07854-6088-R000, to be issued.

9. Ohrenberger, J. T., "The Flow of the Boundary Layer into the Near Wake by Rotational Characteristics and Comparisons with Experiment," TRW 07854-6089-R000, to be issued.
10. Fox, J., Webb, W. H., Jones, B. G. and Hammitt, A. G., "Hot-Wire Measurements of Wake Turbulence in a Ballistic Range," AIAA Journal, Vol. 5, January 1967.
11. Golik, R. J., Webb, W. H. and Lees, L., "Further Results of Viscous Interaction Theory for the Laminar Supersonic Near Wake," presented at the Fifth AIAA Aerospace Sciences Meeting, January 1967, Paper No. 67-61.
12. Vogenitz, F. W., Bird, G. A., Broadwell, J. E. and Rungaldier, H., "Theoretical and Experimental Study of Rarefied Supersonic Flow about Several Simple Shapes," TRW 07854-6082-R000, to be issued. Also, to be presented at the Sixth AIAA Aerospace Sciences Meeting, New York, January 1968.

## APPENDIX II

### MONTE CARLO COMPUTER SIMULATION OF TWO-DIMENSIONAL AND AXI-SYMMETRIC SUPERSONIC STEADY FLOWS

The approach is to conduct numerical experiments with a model gas on the computer. The real gas is simulated by the order of a thousand rigid-sphere molecules which may be thought of as a representative sample of the many billions of molecules in the corresponding real gas. The positions and velocity components of the simulated molecules are stored in the computer and typical collisions are computed among them as a time parameter is advanced. The computation of collisions starts at zero time, the molecules having been set up as a uniform stream at the required freestream Mach number. The body is inserted into this flow at zero time and the desired steady flow is obtained as the large time solution of the resulting unsteady flow.

The freestream flow is in the positive  $x$  direction and the simulated region is bounded by the  $x$  axis as a line of symmetry, and by the upstream, outer and downstream boundaries. These boundaries must be set sufficiently far from the body to eliminate interference. The simulated region is divided into a number of cells which are sufficiently small for the change in flow properties across the cell to be small. Since the flow is either two-dimensional or axi-symmetric, only two position coordinates need be stored for each simulated molecule. The three velocity components are also stored and a record is kept of the molecules within each cell.

The first step is to generate the initial, or zero time, configuration of molecules. The molecules are distributed uniformly over the simulated region and the velocity components are appropriate to a gas in Maxwellian equilibrium and moving at the required Mach number.

The body is then inserted into the flow and the molecules are allowed to move and collide among themselves. The two processes are uncoupled by computing collisions appropriate to a time interval  $\Delta t_m$  and by then moving the molecules through distances appropriate to  $\Delta t_m$  and their instantaneous velocities. The distortion produced in the molecular

paths by this approximation is small as long as  $\Delta t_m$  is small compared with the mean time between collisions.

Since the change in flow properties over the width of each cell is small, the molecules in a cell at any instant may be regarded as a sample of the molecules at the location of the cell. The relative location of the various molecules within the cell can then be disregarded and the collision probability of a particular pair of molecules within the cell depends only on their relative velocity. A pair of molecules is chosen at random from those within the cell under consideration and is retained or rejected in such a way that the probability of retention is proportional to the relative velocity  $v_r$ . When a pair is retained, a typical collision is computed between the two molecules and the new velocity components are stored in place of the old ones. The random selection of impact parameters is particularly simple for rigid sphere molecules since all directions for the new relative velocity vector are equally probable.

The time between collisions for the pair is  $(A N v_r)^{-1}$ , where  $N$  is the number density in the cell. For each collision, the time counter for this cell is advanced by

$$\Delta t = (2/N_c) \times (A N v_r)^{-1}$$

where  $N_c$  is the actual number of molecules in the cell. Collisions are computed in the cell until the time counter has advanced through  $\Delta t_m$ . When this procedure has been carried out for every cell, the overall time is advanced through  $\Delta t_m$  and the molecules are moved through appropriate distances.  $N_c/2$  is of course the number of pairs in the cell. Over a large number of collisions, say  $k$ , the average time between collisions is:

$$\Delta \bar{t} = \frac{1}{k} \cdot \sum_{i=1}^k (\Delta t)_i = \frac{1}{k} \frac{2}{A} \sum_{i=1}^k \frac{1}{N_{c_i} N_i v_{r_i}}$$

Now:

$$\frac{1}{k} \sum_{i=1}^k \frac{1}{N_{c_i} N_i v_{r_i}} = \frac{1}{\bar{N}_c \bar{N} \bar{v}_r} \cdot \left\{ \frac{1}{k} \sum_{i=1}^k \frac{\bar{N}_c \bar{N} \bar{v}_r}{N_{c_i} N_i v_{r_i}} \right\}$$

The quantity in brackets should  $\rightarrow 1$  for  $k$  large enough.

Then

$$\overline{\Delta t} = \frac{2}{N_c} \frac{1}{A \bar{N} \bar{v}_r} = \frac{\bar{t}}{(\bar{N}_c/2)}$$

where  $\bar{t}$  = mean time between collisions per molecule.

Then in a time interval  $\bar{t}$ , on the average, each molecule will undergo one collision and will travel an average distance between collisions

$$\bar{t} \cdot \bar{c} = \frac{\bar{c}}{A \bar{N} \bar{v}_r} = \frac{1}{\sqrt{2} A \bar{N}} = \lambda$$

which is the local mean free path. Note that by normalizing all quantities to a reference cell in the free stream, the molecular cross section  $A$  need never be specified e.g.,

$$\frac{\lambda}{\lambda_\infty} = \frac{N_\infty}{N}; \quad \frac{\Delta t}{\bar{t}_\infty} = \frac{2}{N_c} \frac{\sqrt{2} N_\infty \bar{c}_\infty}{N \bar{v}_r}$$

The freestream mean free path is determined by specifying the Knudsen number

$$K_n = \frac{\lambda_\infty}{\text{body dimension}}$$

The set of molecules in each cell will change as the molecules are moved and appropriate conditions must be applied at the boundaries of the region being simulated. The upstream boundary normal to the free-stream direction is treated as a source of molecules with velocity components representative of the downstream moving molecules in the equilibrium freestream. Any molecule which moves back upstream across this boundary is regarded as being "lost" and is removed from the store. The plane of symmetry along the  $x$  axis is regarded as a specularly reflecting surface in two-dimensional flows. The outer and rear surfaces present greater difficulties. A procedure has been developed which usually introduces only a small reflected disturbance and which becomes exact in free molecule flow. This is to regard a molecule as "lost" if it moves outward across the boundary but, if it moves inward from the boundary during the time interval  $\Delta t_m$  through a distance greater than its original

distance from the boundary, it moves to the new position and a similar molecule is added in the original position.

The rationale for this procedure is as follows: since there are supposed to be no gradients in mean properties normal to the boundary (uniform flow) it is equally likely that a similar molecule crosses any horizontal line near the boundary. A molecule moving into the field away from the boundary through a distance greater than its initial distance from it is a statistical measure of the event that a molecule crosses the boundary and enters the field. Placing it so that it enters during the next movement interval is a convenient way of handling the book keeping of getting it inside the field.

The latter part of this procedure should only be applied to those molecules with properties similar to the freestream molecules. An alternative procedure would be to regard the outer boundary as a specularly reflecting surface. While this would result in a larger reflected disturbance, it does permit a simple physical interpretation.

Interactions with the body must also be computed. The body is assumed to have a diffusely reflecting surface with an accommodation coefficient of unity. After the flow has settled down to a steady state, the momentum and energy transfer to the surface is recorded and is used to compute the aerodynamic data. The time required to establish steady flow may usually be assumed to be close to the time required for the freestream to travel several body dimensions. The flow field properties are also sampled in the steady flow. Instantaneous samples are recorded at appropriate time intervals and these are averaged for greater accuracy. The time interval for sampling  $\Delta t_g$  should be of the order of the time required for the flow to traverse one cell.

The results become progressively more accurate as the sample size is increased and the statistical scatter is reduced. An indication of the order of this scatter is given by the normal distribution result that the standard deviation is equal to the reciprocal of the square root of the number in the sample. 68.3% of the results should lie within one standard deviation, 95.5% within two and 99.7% within three. Successful runs have been made with as few as six simulated molecules in each cell and the statistical fluctuations do not appear to induce instabilities in the flow.



The key to the simulation is the procedure which selects the molecules for a collision pair according to the correct probability and then advances the time parameter by the appropriate amount for each collision. In this way, an appropriate set of collisions is computed for any distribution function of molecular velocities. Apart from the boundary conditions, only two approximations are made. The first is the uncoupling of the molecular collisions and motion, and this becomes exact as  $\Delta t_m$  tends to zero. The second is the assumption of uniform properties over the cell and this disappears as the cell size tends to zero.

Programs have been developed for supersonic flow past,

- i) flat plate at zero incidence,
- ii) circular cylinder with axis normal to flow,
- iii) sphere,
- iv) sharp nosed wedge at zero incidence

and

- v) sharp nosed cone at zero incidence.

The overall number flux, drag, and heat transfer coefficient are determined for each body, together with their distribution along or around the surface of the body. Flow field properties are sampled and number density, flow velocity and temperature are output at a number of points in the flow. As an indication of the degree of non-equilibrium, the temperatures based on the individual velocity components are also output. In addition, the velocity distribution may be sampled at a number of points in the flow. Simulated equilibrium temperature probes may be set in the flat plate and cylinder flows.

### APPENDIX III

#### PARAMETERS OF THE MONTE CARLO CALCULATION

The steady state flow field properties of a body will depend upon a set of fluid mechanical parameters; viz,

$$C_D = f(K_n, M, T_b/T_\infty, \text{Surface reflection properties, Fluid properties, Body shape, etc.})$$

The Monte Carlo estimate of the same property, denoted by  $\tilde{C}_D$ , for given fixed values of the above fluid mechanical properties will depend upon a set of calculation parameters; viz,

$$\tilde{C}_D = \tilde{f}(\text{Sample size, Chance, Movement time, Cell size, Initial Field accuracy, Field Size})$$

The first two quantities reflect the fact that the calculation is a statistical one. The sample size is the number of molecules to contribute information regarding the particular property to be determined, such as density or drag. Computing the arithmetic mean of the sample (the information from each molecule is weighted equally) we can appeal to two laws of statistics<sup>12</sup> to tell us something about how the sample mean should behave. The Strong Law of Large Numbers says that the sample mean will tend toward the true mean as the sample size tends to infinity:

$$\tilde{C}_{D_{SS}} \longrightarrow \bar{C}_D \quad \text{as} \quad SS \longrightarrow \infty$$

The Central Limit Theorem further says that as the sample size tends to infinity the distribution of the sample mean will tend toward a Gaussian distribution with variance

$$\sigma_{\tilde{C}_D}^2 \longrightarrow \frac{\sigma_{PP}^2}{SS}$$

where  $\sigma_{PP}^2$  is the variance of the parent population from which the samples are taken. Note that the sample mean is a distributed variable which means that if the calculation is repeated with different random numbers but fixed values of all parameters including sample size, in general the

sample mean will be different. The mention of infinity in the two laws need not cause concern; it is surprising how small a sample is needed for the laws to take hold.

In general it is difficult to make a priori estimates of the dispersion of the sample mean since the dispersion of the parent population is unknown.

For the following simple situation an approximate numerical estimate can be made: consider near-free molecule flow past a flat plate. Assume diffuse reflection from plate.



Molecules in the flow field can be considered nearly in Maxwellian equilibrium with distribution of U velocity

$$f(U) = \frac{1}{\sqrt{2\pi} \sigma_U} e^{-\frac{1}{2\sigma_U^2} (U - \bar{U}_\infty)^2}$$

where

$$\sigma_U = \frac{v m_\infty}{\sqrt{2}}$$

Because the reflection is diffuse the tangential momentum transferred to the plate by each molecule which strikes it is  $mU$ .

Average number flux to unit area of plate

$$\sim \frac{\rho_\infty \bar{c}_\infty}{4m} = \frac{\rho v m_\infty}{2\sqrt{\pi} m}$$

In a small time interval,  $\Delta t$ , then the average number of molecules to hit unit area of the plate is:

$$\text{sample size } SS = \frac{\rho v m_\infty}{2\sqrt{\pi} m} \Delta t$$

The estimated momentum flux to the plate is then

$$\text{Momentum flux } \tilde{D} = \frac{1}{\Delta t} \sum_{i=1}^{SS} m U_i = \frac{\rho_{\infty} v_{m_{\infty}}}{2 \sqrt{\pi}} \frac{1}{SS} \sum_{i=1}^{SS} U_i$$

Normalizing to get an estimate of drag coefficient:

$$\tilde{C}_D = \frac{\tilde{D}}{\frac{1}{2} \rho \bar{U}_{\infty}^2} = \frac{v_{m_{\infty}}}{\sqrt{\pi} \bar{U}_{\infty}^2} \frac{1}{(SS)} \sum_{i=1}^{SS} U_i$$

Then:

$$\begin{aligned} \text{Variance } (\tilde{C}_D) &= \left( \frac{v_{m_{\infty}}}{\sqrt{\pi} \bar{U}_{\infty}^2} \right)^2 \frac{1}{(SS)^2} \sum_{i=1}^{SS} \text{Variance } (U_i) \\ &= \left( \frac{v_{m_{\infty}}}{\sqrt{\pi} \bar{U}_{\infty}^2} \right)^2 \cdot \frac{1}{(SS)} \sigma_U^2 = \left( \frac{1}{\sqrt{2\pi} S^2} \right)^2 \frac{1}{SS} \\ \therefore \sigma_{\tilde{C}_D} &= \frac{1}{\sqrt{2\pi} S^2} \cdot \frac{1}{\sqrt{SS}} \end{aligned}$$

An approximation for the mean value of  $\frac{1}{SS} \sum U_i$  is  $\bar{U}_{\infty}$ . Substituting in the expression for  $\tilde{C}_D$  we get

$$\bar{C}_{D \text{ free molecule}} \sim \frac{1}{\sqrt{\pi} S}$$

Then

$$\sigma_{\tilde{C}_D} = \frac{1}{\sqrt{2} S} \cdot \frac{1}{\sqrt{SS}} \bar{C}_D$$

For more complicated flows where the molecules in the field have widely differing distributions, no such numerical estimate can be made, but  $\sigma$  would be expected to be larger. On purely empirical grounds it has been assumed in the analysis in this report that:

$$\sigma_{C_D} = \frac{1}{\sqrt{SS}} \cdot \tilde{C}_D$$

where SS is the sample size. Judging by the scatter in repeated calculations, this somewhat overestimates  $\sigma$ .

We now return to the other parameters which influence the flow properties; viz, Movement time, Cell size, Initial Field Accuracy, and Field Size. In order for the calculation method to be easily utilized, it would be hoped that the results not be extremely sensitive to these parameters. This indeed turns out to be the case. Movement time,  $\Delta t_m$ , and cell size are somewhat akin to the stepsize in a finite difference calculation — they need only be reduced in size until the change in the result falls below a certain level (unlike the effect of step size the calculation does not diverge suddenly as they are increased, the degradation of accuracy occurs rather slowly).

The movement time has been varied from  $.05 \bar{t}_\infty$  to  $.15 \bar{t}_\infty$  with negligible effect on the drag calculation as shown in Figure 6. The effect of this change on density and temperature on the stagnation line is shown in Figures III-1 and III-2. There is no apparent effect on density but

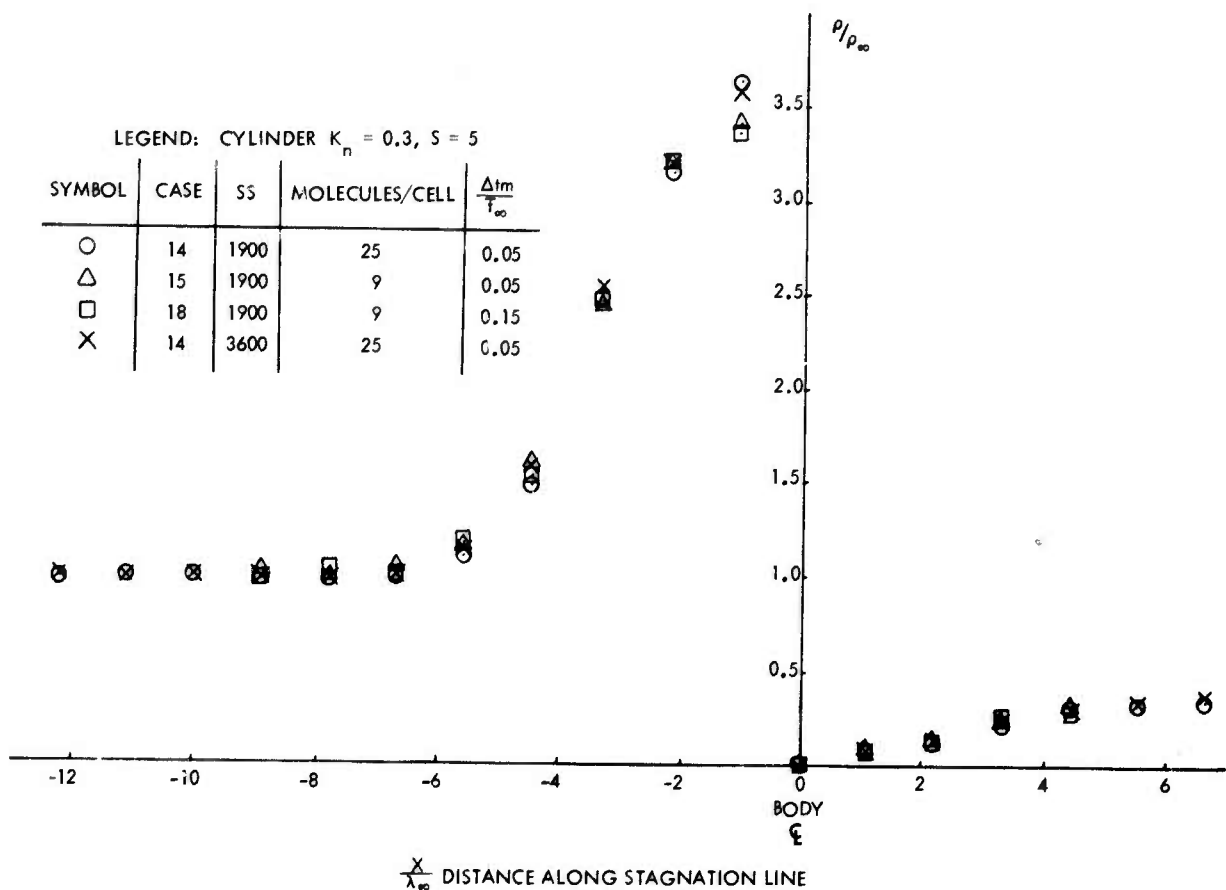


Figure III-1 Effect of Calculation Parameters on Stagnation Line Density

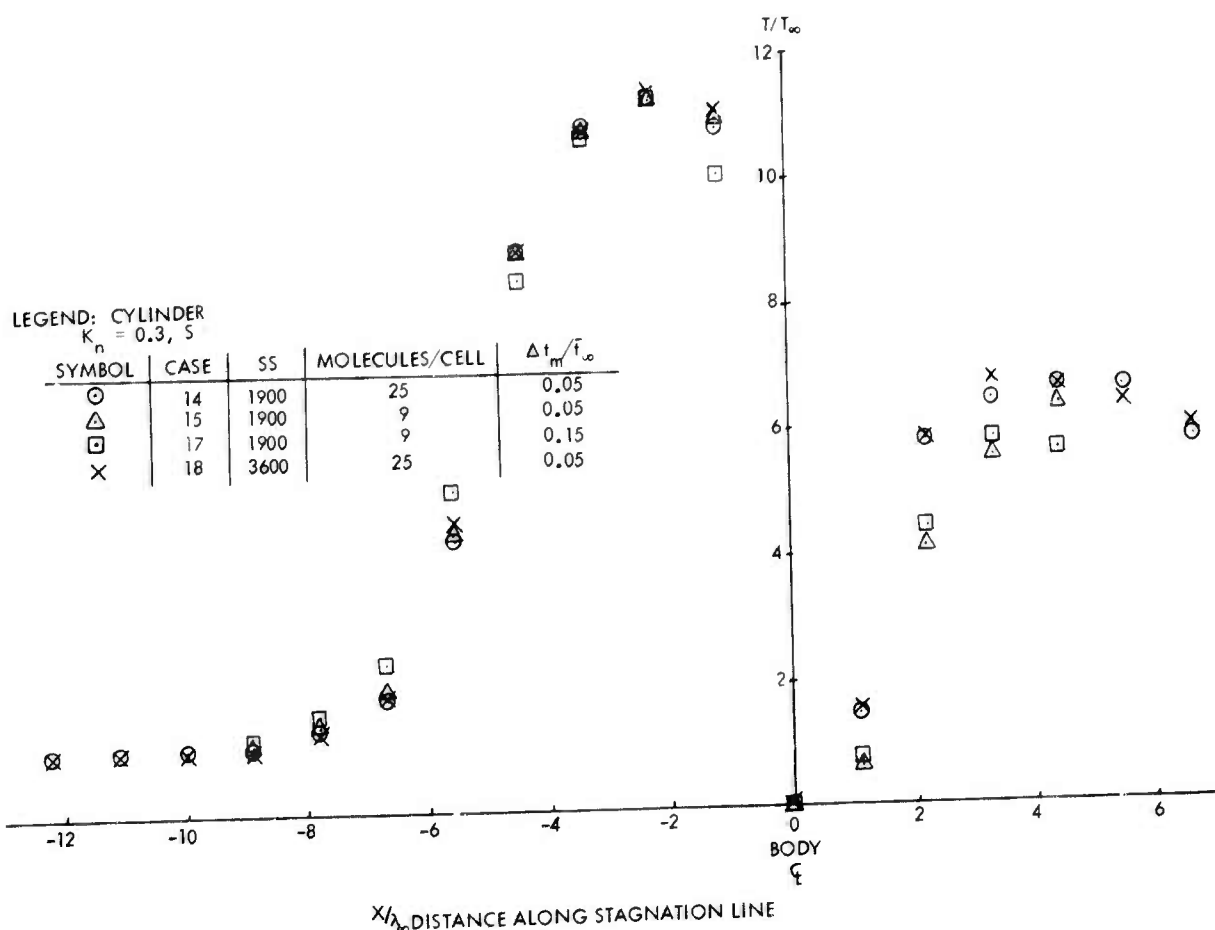


Figure III-2 Effect of Calculation Parameters on Stagnation Line Temperature

temperature, which is more sensitive, shows a trifle more scatter at  $\Delta t_m = .15 \bar{t}_\infty$ .

Cell size has not been varied systematically so that its effect could be completely isolated but the results of many different calculations with different cell sizes suggest that as long as the cell width is not greater than two mean free paths in regions of strong gradients the results are not strongly influenced.

The calculation is performed by instantaneously inserting the body and allowing the field to evolve to an approximate steady state at Time =  $T_{ST}$ . The calculation of the cumulative average to determine flow properties is begun at this point. The initial number of molecules in each cell thus affects the sample size involved in determining this approximate steady state, and hence the accuracy of the calculation at some later time, since dispersion in the initial field takes some time to be averaged out. The density and temperature profiles on the stagnation line of a

cylinder at time =  $T_{ST}$  for 25 and 9 molecules/cell are shown in Figures III-3 and III-4. The larger sample has reduced the initial scatter in density but temperature, which is more sensitive, shows large scatter for both values.

The effect of field size is shown in Figures III-5 and III-6 where density and temperature profiles on the stagnation line and along a line which coincides with the upper boundary of the small field are compared. The field sizes are shown in Figure 8. There is negligible effect on the stagnation line in front of the body and only a very slight effect appearing on the downstream portion of the upper boundary line. Temperature does appear to be more sensitive than density and there is some unexplained scatter in the temperature values on the stagnation line in the rear of the body. The upper boundary condition is approximate and molecules crossing the boundary into the field would be expected to introduce something extraneous to the disturbance from the body; however, since the flow is hypersonic or strongly supersonic, the effects of errors introduced by the feeble thermal motion across the boundary are swept downstream rapidly and show up, if at all, only near the boundary downstream of the body.

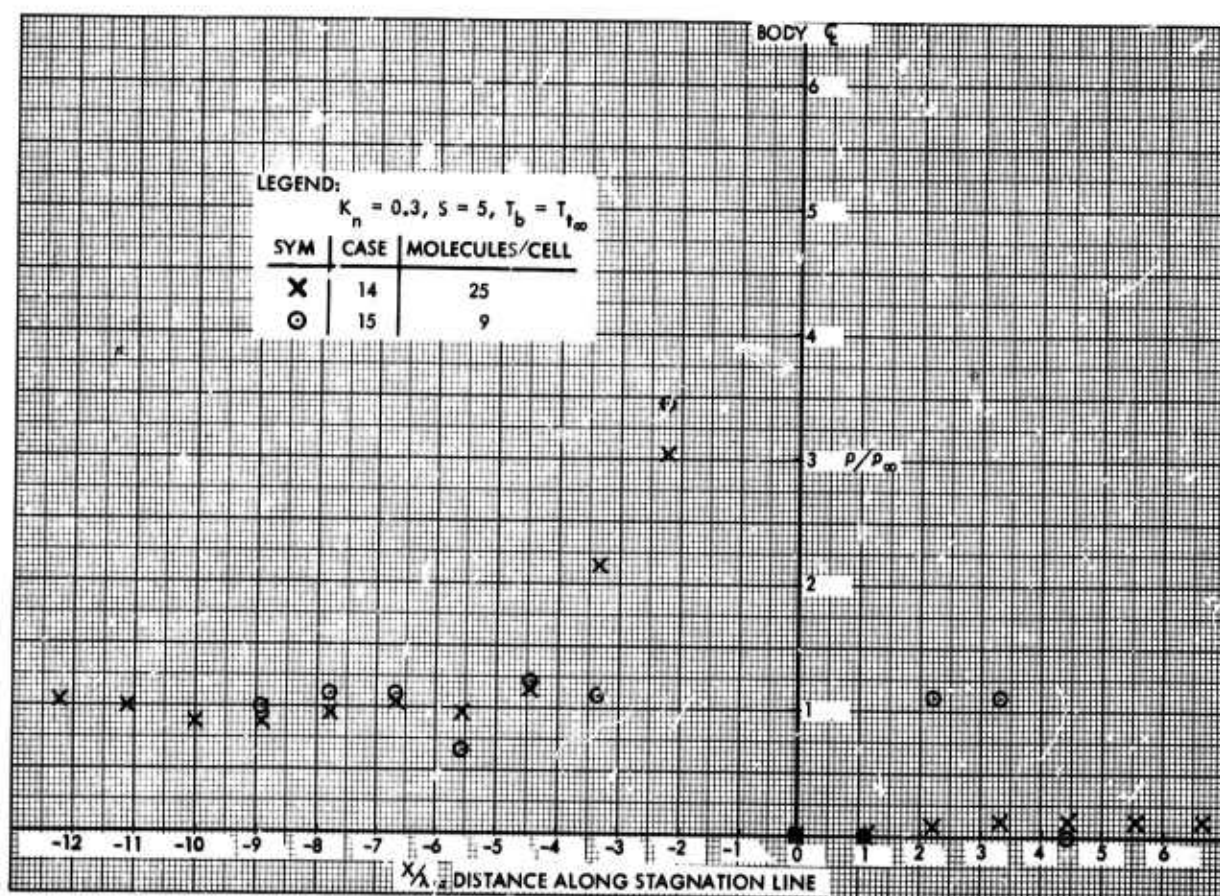


Figure III-3 Initial Field Scatter Density on Stagnation Line of a Cylinder



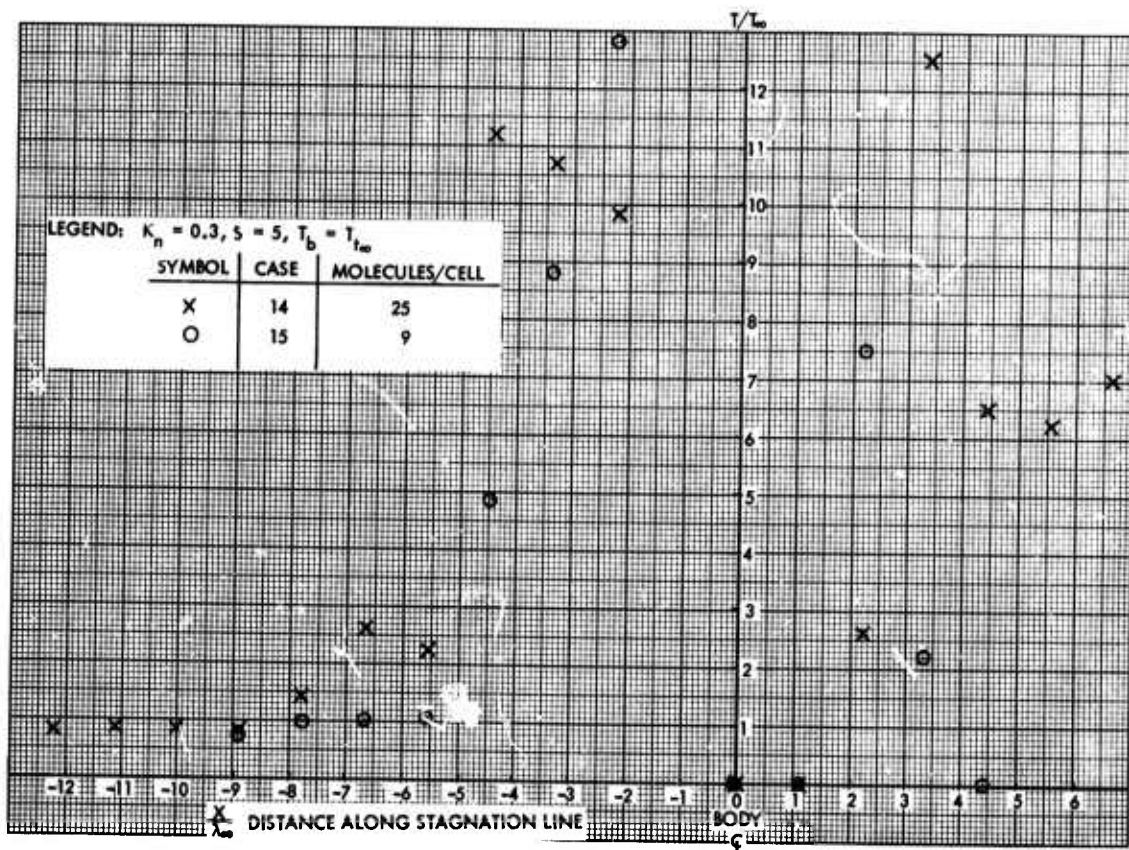


Figure III-4 Initial Field Scatter Temperature on Stagnation Line of a Cylinder

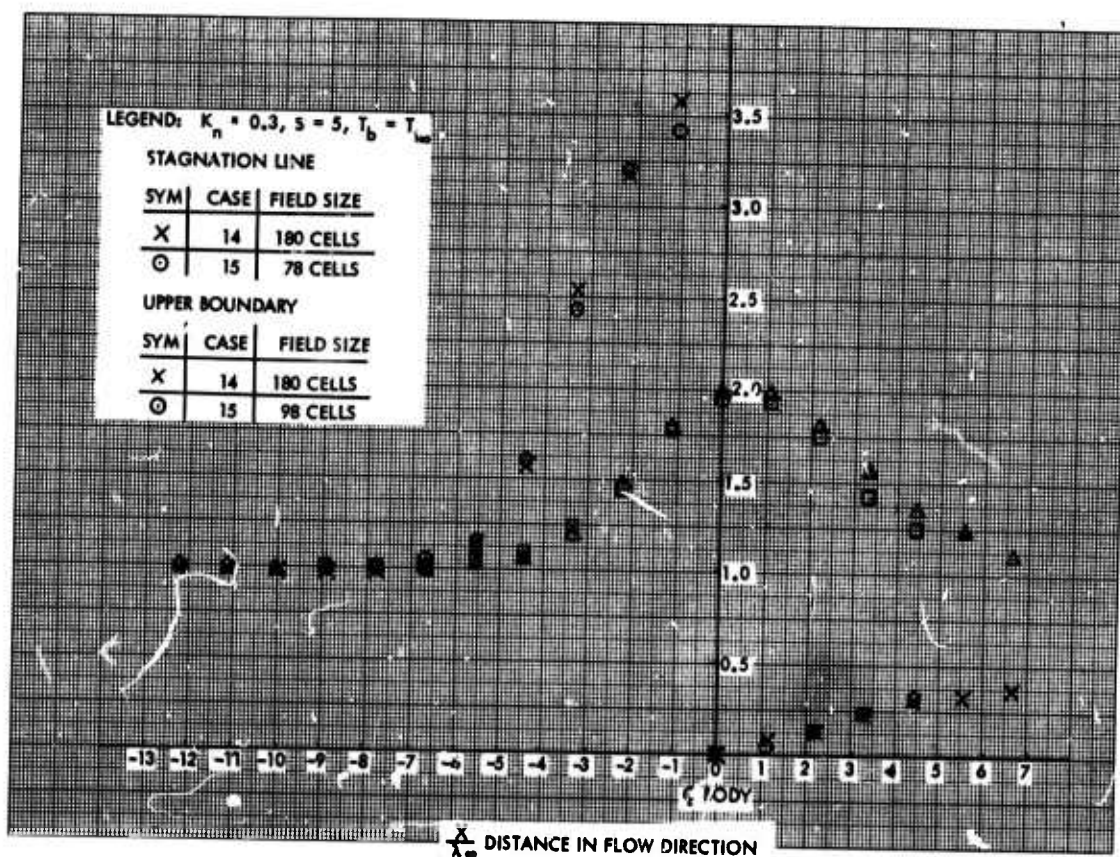


Figure III-5 Effect of Field Size on Density in the Flow Field of a Cylinder

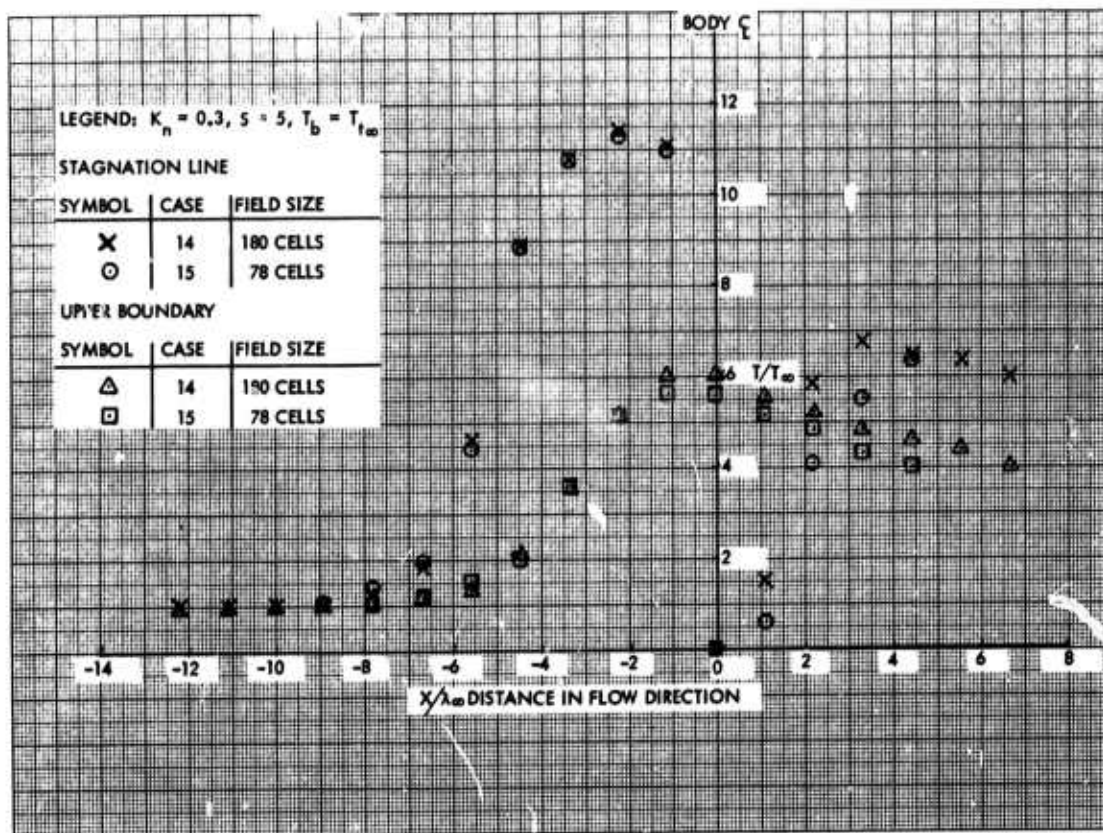


Figure III-6 Effect of Field Size on Temperature in the Flow Field of a Cylinder

## APPENDIX IV

### DESCRIPTION OF LOW DENSITY WIND TUNNEL EXPERIMENTAL SET-UP

#### IV. 1 EXPERIMENTAL METHODS AND PROCEDURES

##### IV. 1. 1 Experimental Equipment

All experiments were carried out in the TRW Systems Low Density Wind Tunnel. This facility is a steady flow tunnel exhausted by two diffusion pumps backed by a mechanical vacuum pump. Two nozzles were used in these experiments; one has an area ratio of twenty-five with an exit diameter of two inches, and is conical with a ten degree half angle. The other has an area ratio of 188 with an exit diameter of 1.7 inches and is also conical with a ten degree half angle. Both argon and nitrogen were used as the working gas, and were supplied at room temperature from high pressure bottles. The experiments were carried out 0.4 inches downstream of the nozzle exit plane in the large low pressure test section. The flow conditions used at this section in the flow may be found in Tables IV-1 and IV-2.

##### IV. 1. 2 Drag Measurements

The drag balance used in this experiment was an adaptation of the Cahn Electrobalance, Model RG, which is a remote control unit, capable of operation in vacuum and has a very high sensitivity. The balance is a null-type single component type beam balance. The beam is mounted on a meter movement which can be driven to a null position. The null position is determined by a photo cell which senses light striking it through a slit. In front of the slit the balance beam moves up and down, thus allowing more or less light to reach the cell. If an amount of light other than that of the null position reaches the cell, a feed back circuit drives the meter movement to return the beam to its null position. The current necessary to accomplish this return has been calibrated and can be read out directly as a force.

In order to use the balance in this experiment, certain modifications had to be made. A picture of the balance, see Figure IV-1, will help to explain these. In order to support the sting necessary to mount the model,

a clamp had to be made which holds the sting arrangement to the balance beam. The sting then goes through a shield and finally attaches to the model. In order to minimize the weight effects of the clamp and sting a counter weight was built which balances the moments about the pivot. It is also necessary to lower the center of gravity of the system below the pivot in order to be operating in a stable condition. To support the balance in the tunnel, a case was built which could be moved in two directions on the support pad and on which the sting shield could be mounted. This sting shield is necessary to keep down the drag forces on the sting as much as possible.

In Figure IV-2 can be seen the actual support of the models on the balance. The model is supported on the upright part of the sting by a very thin horizontal piece. In order to investigate the size effect of this horizontal piece two different diameter stings were used. One was a 1.5 inch long, 0.028 inch diameter stainless steel tube; the other a 1.5 inch long, 0.010 inch diameter tungsten rod. On the 0.125 inch diameter models, this gave a sting to base area ratio of 5% and 0.6% respectively.

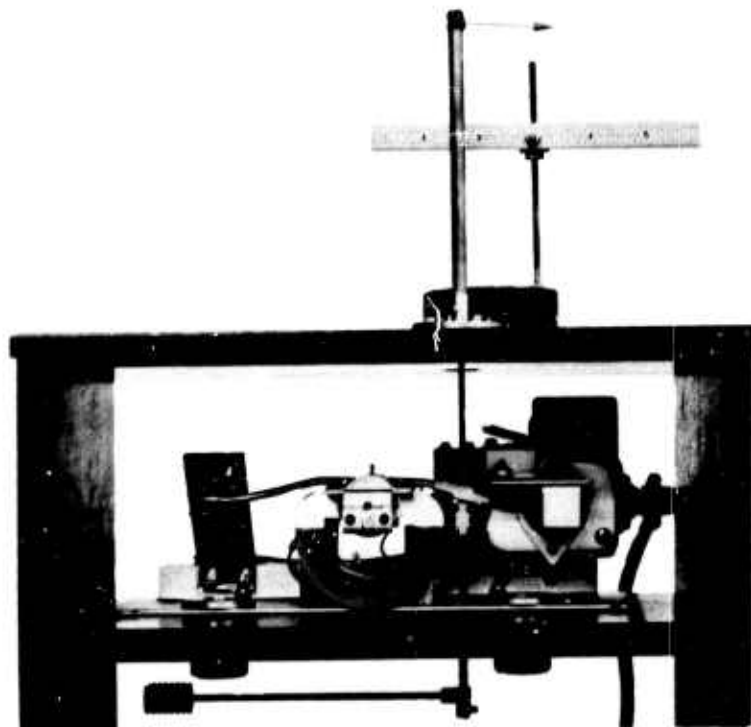


Figure IV-1. Balance and Model in Test Configuration

In order to eliminate the drag of the support mechanism from the model drag a dummy model and sting arrangement was made. Again in Figure IV-2 we see a schematic of this set-up. A dummy sting of the proper size is inserted in the beam clamp and positioned in the flow. A model was then attached to an external support free from the balance and positioned in front of the dummy sting. In order to give correct readings, the model was put within 0.001 inches from the sting. Since the balance is of the null type, the sting always remains in the same position even though varying forces are applied to it during a run. The effect of the sting holding the dummy model was determined to be negligible.

Two models were used in these drag investigations. One was a 0.125 inch diameter nylon sphere, the other a 90° half angle aluminum cone with a base diameter of 0.125 inches and a nose bluntness ratio of 0.10.

#### IV. 1.3 Flow Field Surveys

The flow field in the stagnation region of the various models tested was investigated with a free molecule equilibrium temperature probe.

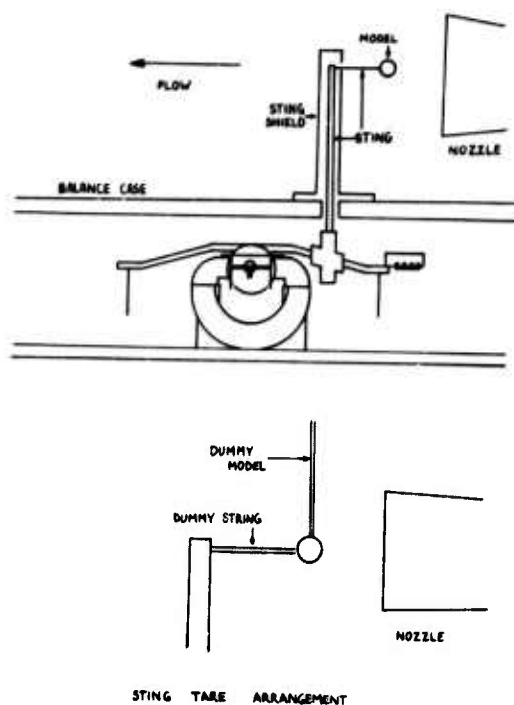


Figure IV-2. Schematic of Model and Dummy Model Setup in the Balance

(References 4 and 5.) The models used in this survey were two wedges and four cylinders. One wedge was sharp with a  $10^\circ$  half angle; the other a 10 percent nose bluntness wedge with  $9^\circ$  half angle. Both of these wedges were run at zero degrees angle of attack.

The cylinders had diameters of 0.002, 0.005, 0.0153, and 0.125 inches.

The free molecule probe was made in the form shown in Figure IV-3. A small current, about 0.08 ma was passed through the vertical tungsten wire (0.0002 inch in diameter). The voltage drop in the central 0.5 inches of the wire was measured through potential leads made of 0.00025 inch diameter platinum-tungsten wire. The voltage drop, or resistance, which changes with temperature could then be recorded. In addition to providing the potential leads, the platinum-tungsten wires form thermocouples with the tungsten wire. The two junctions could, with the current shut off in the central wire, be used to record the point temperature at the ends of the resistance section. The probe was calibrated in an oven before using. The center part of the wire, including the two thermocouples, was inserted

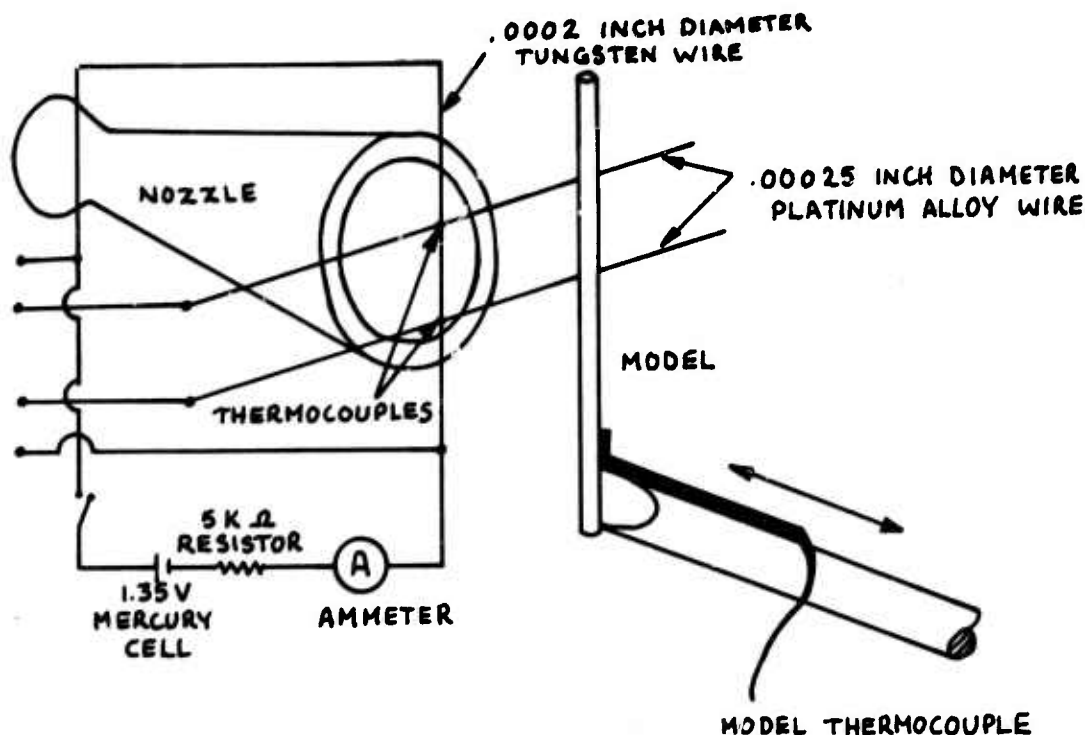


Figure IV-3. Schematic of the Equilibrium Temperature Probe and Circuitry



into a small copper block which was heated by an electric resistance heater. This was done to simulate the conditions existing while testing in the wind tunnel. The wire output, both the Emf and thermocouple readings, were then plotted on an x-y recorder against a Cr-A<sub>1</sub> thermocouple. A calibration curve for the wire Emf and thermocouple output against temperature was then constructed.

The probe was made by stretching all three wires over the posts and springs (Figure IV-4) and securing them under tensions of approximately two-thirds of their yield stress. Such tensions are necessary to minimize deflections under drag loads. The junctions are then copper-plated and soft soldered to form the joints. Care was taken to make the points as small as possible since the recovery temperature of the system is dependent on the Knudsen number. Figure IV-4 shows the probe in position between the model and nozzle exit plane.

In the experiment the wire probe was generally held stationary and the models moved on a lathe cross feed. The whole stagnation region could thus be investigated. The model location was monitored by dial

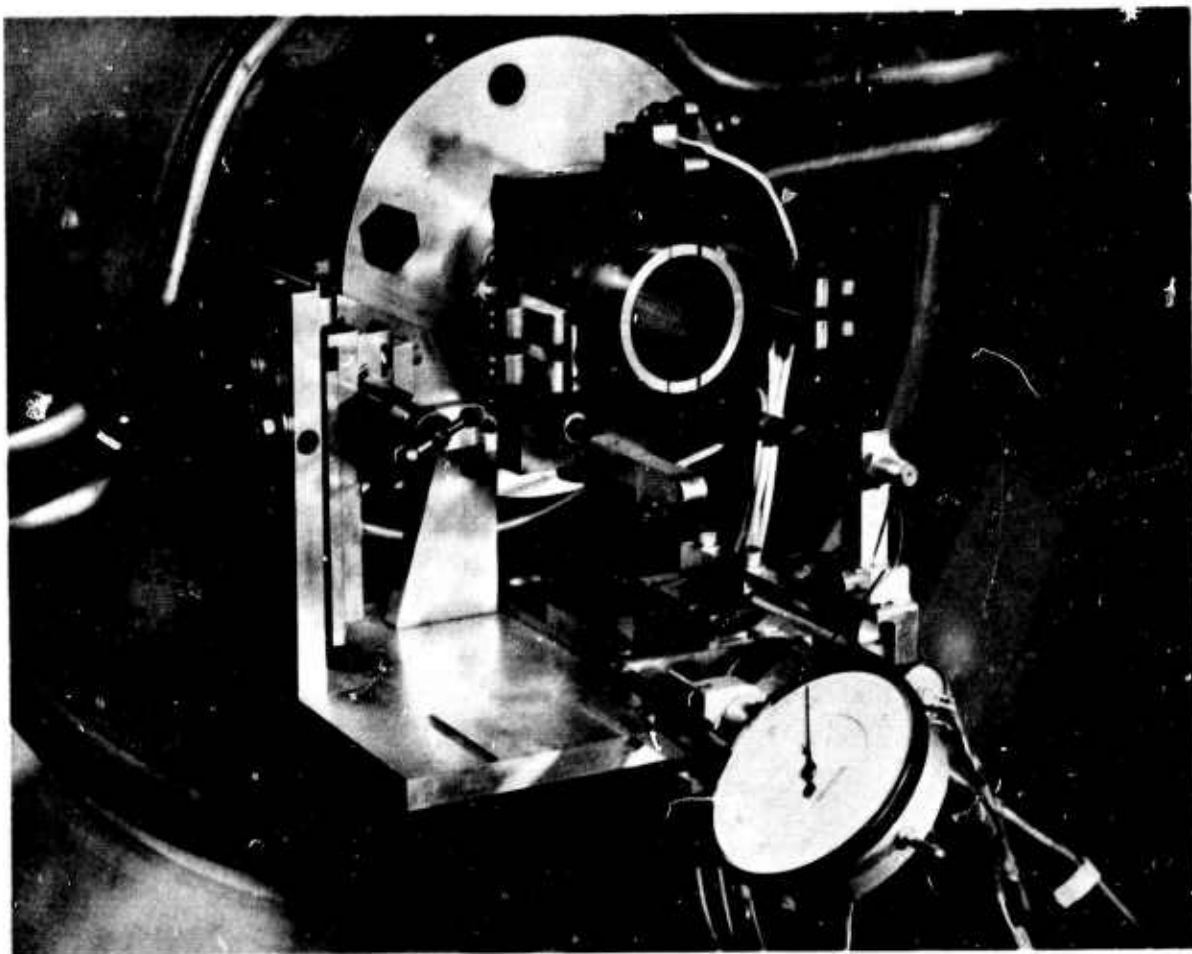


Figure IV-4. Equilibrium Temperature Probe in Operating Condition in Wind Tunnel



indicators of 0.001 inch least count. The x-axis, or stagnation line, location of the model was also indicated by a Sanborn displacement transducer whose output was directly connected to the x-axis of an x - y recorder. The resistance wire and thermocouple outputs were connected to the y-axis of the recorder.

In the case of the blunt  $90^\circ$  wedge a modification had to be made. Since this model was run both at liquid nitrogen temperature in addition to the recovery temperature run, it was necessary to hold the model as firmly as possible to avoid deflection under liquid nitrogen conditions. To accomplish this it was necessary to mount the wire probe on the crossfeed and hold the model firmly to the tank. The wire position was monitored in the same way the model had been in the other runs.

The temperature in the reservoir was measured by a chromel-alumel thermocouple, and the model and wire holder post (which forms the cold junction of the wire thermocouples) were measured by copper-constantan thermocouples.

The 0.125 inch cylinder was made from a steel rod and supported much like the model in Figure IV-4. The smaller cylinders were actually wires supported by a U-shaped frame attached to the cross feed.

The  $10^\circ$  sharp wedge was made from oil hardened steel and ground to a sharp edge of approximately 0.0001 to 0.0003 inches. The blunt wedge was also machined from steel with a hole drilled through the back. The liquid nitrogen, supplied from a standard pressurized bottle and vented to atmosphere, was passed through that hole.

The alignment of model and wire was accomplished by observing the adjustments through a jig transit with an optical micrometer. Wire and model were aligned parallel within 0.001 inch over the length of the model. The jig transit was also used to measure the deflection of the wire under drag loads. Some typical deflection values are presented in Table IV-5.

Probe deflection becomes a problem when one moves off the stagnation line since the drag on the probe wires changes as one moves to different parts of the flow field. Since it would be a very time-consuming process to measure the wire deflection at all the conditions used in the experiment, it was decided to use the information gathered on the

stagnation line surveys to reduce off line data. The correction was assumed to be constant for equal densities or temperature ratios, and was carried out accordingly. Spot checks of this method showed it to be satisfactory and the method was used throughout the experiments.

## IV. 2 DATA REDUCTION

### IV. 2. 1 Flow Field Calculations

The usual method of flow field calculation, using the impact and stagnation pressure measurements with an assumption of isentropic flow, was used in reducing the data. Surveys were run in the test region of the nozzle, both axially and radially. Since the nozzles were conical and not contoured, both radial and axial Mach gradients exist. A range of stagnation pressures was found for both nozzles where the flow field consisted of a large enough isentropic core to envelop the free molecule probe and where the gradients were small over distances comparable to the model dimensions. The calculations were then carried out using the tables of Reference 15.

The viscosity of air was determined by the Sutherland formula

$$\mu_{\infty} = 2.27 \frac{T_{\infty}^{3/2}}{T_{\infty} + 198.6} \times 10^{-8} \text{ lb sec/ft}^2$$

For Argon the viscosity was interpolated from the tables in Reference 16. The mean free path was then found from the equation

$$\lambda_{\infty} = \mu_{\infty} \left[ \rho_{\infty} \sqrt{\frac{2}{\pi}} RT_{\infty} \right]^{-1}$$

The flow field parameters which are of importance, and against which the data were plotted are as follows.

For the drag measurements the drag coefficients were plotted against Reynolds number. In the case of the sphere drag the Reynolds number was based on free stream values and is defined as

$$Re_{\infty D} = \frac{V_{\infty} \rho_{\infty} D}{\mu_{\infty}}$$

For the cone drag the Reynolds number suggested by Potter (Reference 17) was used:

$$Re_{we} = Re_{\infty l} \left( \frac{T_{\infty}}{T_w} \right)^{1/2} \quad \text{where} \quad \frac{\mu_{\infty}}{\mu_w} = \left( \frac{T_{\infty}}{T_w} \right)^{1/2}$$

or

$$Re_{we} = Re_{\infty l} \frac{\mu_{\infty}}{\mu_w} = \frac{V_{\infty} \rho_{\infty} l}{\mu_w}$$

where  $l$  is the wetted length of the cone and  $\mu_w$  is evaluated at the wall temperature. This Reynolds number was chosen because it seems to correlate all cone data in the transition regime, independent of bluntness or wall to stagnation temperature ratio.

#### IV. 2. 2 Drag Coefficient Determination

Since the setup for both the spheres and cones was the same, the data were reduced identically. Force at the pivot point is read off the control box of the micro balance. To obtain the force acting on the model the proper moment arms have to be used. The sting correction numbers are obtained in a similar fashion. Drag coefficient is calculated in the following way:

$$C_D = \frac{F_{\text{model} + \text{sting}} - F_{\text{sting}}}{q A}$$

where  $q$  is the dynamic pressure and  $A$  the area based on the model diameter.

Table IV-1. Flow Conditions at the Test Station of the Drag Balance Studies

Model	Gas	Stagnation Pressure, $P_t$ mm Hg	Stagnation $T_t$ Temperature, $^{\circ}R$	Mach Number $M$	$Re_{\infty D}$	Cone $Re_{w,l}$
0.125 inch Diam. Sphere and 0.125 inch Base Diam. $90^{\circ}$ Cone	$N_2$	5	533	3.92	100	82
		10	533	4.20	176	125
		15	533	4.33	249	167
		20	533	4.40	322	210
		25	533	4.46	392	255
	$N_2$	50	533	5.95	448	160
		100	533	6.35	783	241
		150	533	6.57	1095	311
		200	533	6.73	1390	373

Table IV-2. Flow Conditions and Models Used in the Flow Field Surveys

Model	Gas	Stagnation Pressure, $P_t$ mm Hg	Mach Number $M$	Knudsen Number $K_{No}$	Mean Free Path, $\lambda^\infty$ inches x $10^{-3}$	Body Temperature $T_b$
0.125 inch CYL	$N_2$	100	6.35	0.012	1.495	$T_{t^\infty}$
		250	6.75	0.0062	0.776	$T_{t^\infty}$
0.0156 inch CYL	$N_2$	100	6.35	0.098	1.495	$T_{t^\infty}$
		250	6.75	0.051	0.776	$T_{t^\infty}$
	Ar	15	5.20	0.136	2.09	$T_{t^\infty}$
		25	5.43	0.106	1.40	$T_{t^\infty}$
		40	5.72	0.069	1.05	$T_{t^\infty}$
0.005 inch CYL	Ar	15	5.20	0.418	2.09	$T_{t^\infty}$
		25	5.43	0.280	1.40	$T_{t^\infty}$
		40	5.72	0.210	1.05	$T_{t^\infty}$
0.002 inch CYL	Ar	15	5.20	1.043	2.09	$T_{t^\infty}$
		25	5.43	0.700	1.40	$T_{t^\infty}$
		40	5.72	0.525	1.05	$T_{t^\infty}$
20° Wedge Sharp	$N_2$	100	6.35		1.495	$T_{t^\infty}$
		250	6.75		0.776	$T_{t^\infty}$
18° Wedge	$N_2$	100	6.35		1.495	$T_{t^\infty}$
10% Nose		250	6.75		0.776	$T_{t^\infty}$
Bluntness		100	6.35		1.495	$T_{t^\infty}$
		250	6.75		0.776	$T_{t^\infty}$

Table IV-3. Sample Deflection Measurements for the  
Equilibrium Temperature Probe

Model	Gas	Stagnation Pressure Pt, mmHg	Mach Number M	Distance From Stagnation Point x, inches	Deflection at x inches
0.0156 inch Cylinder	N <sub>2</sub>	100	6.35	0.040	0.002
				0.030	0.002
				0.020	0.002
				0.010	0.002
				0.005	0.001
		250	6.75	0.040	0.005
				0.030	0.005
				0.020	0.005
				0.010	0.004
				0.005	0.003
	Ar	15	5.20	0.040	0.004
				0.030	0.004
				0.020	0.003
				0.010	0.002
				0.005	0.002
		25	5.43	0.040	0.006
				0.030	0.005
				0.020	0.005
				0.010	0.002
				0.005	0.003
		40	5.72	0.040	0.007
				0.030	0.007
				0.020	0.008
				0.010	0.004
				0.005	0.003

Unclassified

Security Classification

## DOCUMENT CONTROL DATA - R&amp;D

(Security classification of title, body of abstract and indexing annotation must be entered when the overall report is classified)

1 ORIGINATOR, ACTIVITY (Corporate author)

TRW SYSTEMS

2a REPORT SECURITY CLASSIFICATION

Unclassified

2b GROUP

3 REPORT TITLE

PENETRATION SYSTEMS STUDIES  
REENTRY PHYSICS PROJECT -- FINAL REPORT

4 DESCRIPTIVE NOTES (Type of report and inclusive dates)

Technical Report -- Final

5 AUTHOR(S) (Last name, first name, initial)

Hromas, L. A., et al.

6 REPORT DATE

October, 1967

7a TOTAL NO OF PAGES

145

7b NO OF REFS

58

8a CONTRACT OR GRANT NO

AF 04(694)-992

b PROJECT NO

ARPA Order No. 388

9a ORIGINATOR'S REPORT NUMBER(S)

07854-6099-R000

9b OTHER REPORT NO(S) (Any other numbers that may be assigned this report)

SAMSO-TR-67-133

10 AVAILABILITY/LIMITATION NOTES This document is subject to special export controls and each transmittal to foreign governments or foreign nationals may be made only with prior approval of Space and Missile Systems Organization (SMSO), Los Angeles AFS, Los Angeles, California.

11 SUPPLEMENTARY NOTES

12 SPONSORING MILITARY ACTIVITY

Space and Missile Systems Org.  
Air Force Systems Command  
Norton Air Force Base, Calif.

13 ABSTRACT The present report describes the results obtained under the Reentry Physics portion of the Penetration Systems Studies contract. The purpose of the contract is to carry out analyses and experiments of hypersonic flow in support of missile detection and discrimination technology. The work comprises the following five tasks: (a) high altitude drag investigation, (b) nonequilibrium turbulent boundary layer, (c) wake turbulence measurements, (d) improved laminar wake, and (e) near wake analysis. The last four tasks fall under the general heading of hypersonic wake and boundary layer technology. The objective and approach for each task is presented together with a summary of the results obtained to date.



14	KEY WORDS	LINK A		LINK B		LINK C	
		ROLE	WT	ROLE	WT	ROLE	WT
	Reentry Physics High Altitude Drag Boundary Layer Laminar Wake Near Wake Hypersonic Flow						

## INSTRUCTIONS

1. **ORIGINATING ACTIVITY:** Enter the name and address of the contractor, subcontractor, grantee, Department of Defense activity or other organization (corporate author) issuing the report.

2a. **REPORT SECURITY CLASSIFICATION:** Enter the overall security classification of the report. Indicate whether "Restricted Data" is included. Marking is to be in accordance with appropriate security regulations.

2b. **GROUP:** Automatic downgrading is specified in DoD Directive 5200.10 and Armed Forces Industrial Manual. Enter the group number. Also, when applicable, show that optional markings have been used for Group 3 and Group 4 as authorized.

3. **REPORT TITLE:** Enter the complete report title in all capital letters. Titles in all cases should be unclassified. If a meaningful title cannot be selected without classification, show title classification in all capitals in parenthesis immediately following the title.

4. **DESCRIPTIVE NOTES:** If appropriate, enter the type of report, e.g., interim, progress, summary, annual, or final. Give the inclusive dates when a specific reporting period is covered.

5. **AUTHOR(S):** Enter the name(s) of author(s) as shown on or in the report. Enter last name, first name, middle initial. If military, show rank and branch of service. The name of the principal author is an absolute minimum requirement.

6. **REPORT DATE:** Enter the date of the report as day, month, year, or month, year. If more than one date appears on the report, use date of publication.

7a. **TOTAL NUMBER OF PAGES:** The total page count should follow normal pagination procedures, i.e., enter the number of pages containing information.

7b. **NUMBER OF REFERENCES:** Enter the total number of references cited in the report.

8a. **CONTRACT OR GRANT NUMBER:** If appropriate, enter the applicable number of the contract or grant under which the report was written.

8b, 8c, & 8d. **PROJECT NUMBER:** Enter the appropriate military department identification, such as project number, subproject number, system numbers, task number, etc.

9a. **ORIGINATOR'S REPORT NUMBER(S):** Enter the official report number by which the document will be identified and controlled by the originating activity. This number must be unique to this report.

9b. **OTHER REPORT NUMBER(S):** If the report has been assigned any other report numbers (either by the originator or by the sponsor), also enter this number(s).

10. **AVAILABILITY/LIMITATION NOTICES:** Enter any limitations on further dissemination of the report, other than those

imposed by security classification, using standard statements such as:

- (1) "Qualified requesters may obtain copies of this report from DDC."
- (2) "Foreign announcement and dissemination of this report by DDC is not authorized."
- (3) "U. S. Government agencies may obtain copies of this report directly from DDC. Other qualified DDC users shall request through \_\_\_\_\_."
- (4) "U. S. military agencies may obtain copies of this report directly from DDC. Other qualified users shall request through \_\_\_\_\_."
- (5) "All distribution of this report is controlled. Qualified DDC users shall request through \_\_\_\_\_."

If the report has been furnished to the Office of Technical Services, Department of Commerce, for sale to the public, indicate this fact and enter the price, if known.

11. **SUPPLEMENTARY NOTES:** Use for additional explanatory notes.

12. **SPONSORING MILITARY ACTIVITY:** Enter the name of the departmental project office or laboratory sponsoring (paying for) the research and development. Include address.

13. **ABSTRACT:** Enter an abstract giving a brief and factual summary of the document indicative of the report, even though it may also appear elsewhere in the body of the technical report. If additional space is required, a continuation sheet shall be attached.

It is highly desirable that the abstract of classified reports be unclassified. Each paragraph of the abstract shall end with an indication of the military security classification of the information in the paragraph, represented as (TS), (S), (C), or (U).

There is no limitation on the length of the abstract. However, the suggested length is from 150 to 225 words.

14. **KEY WORDS:** Key words are technically meaningful terms or short phrases that characterize a report and may be used as index entries for cataloging the report. Key words must be selected so that no security classification is required. Identifiers, such as equipment model designation, trade name, military project code name, geographic location, may be used as key words but will be followed by an indication of technical context. The assignment of links, rules, and weights is optional.